Measurement of the forward-backward asymmetry of charm and bottom quarks using prompt leptons at TRISTAN

Daisuke TATSUMI

In Partial Fulfillment of the Requirements
for the Degree of Doctor of Science

Osaka University
Toyonaka Osaka, Japan

May 1, 1997

Abstract

We report here a new measurement of cross-section and forward-backward asymmetry in the heavy flavour (c and b) quark production using prompt leptons at TRISTAN ($\sqrt{s} = 58$ GeV).

We have improved our capability of identifying electrons and muons and obtained a large sample of heavy flavour quarks events. A sample containing electrons with momentum p >1 GeV/c and muons with $p > 2$ GeV/c were used.

From a fit to momentum (p) and transverse momentum (p_t) spectra of the leptons, the effective Born cross-sections of b and c quark pair production are measured to be

$$\begin{aligned} \sigma_c &= 45.3 \pm 3.2 \text{ (stat.)} \pm 3.8 \text{ (syst.)} \text{ pb} \\ \sigma_b &= 19.3 \pm 1.1 \text{ (stat.)} \pm 0.8 \text{ (syst.)} \text{ pb.} \end{aligned}$$

From a fit to the angular distribution of the thrust axis of the same sample, the forward-backward asymmetries of b and c quark pair production are measured to be

$$\begin{aligned} A_{FB}^c &= -0.47 \pm 0.07 \text{ (stat.)} \pm 0.03 \text{ (syst.)} \\ A_{FB}^b &= -0.38 \pm 0.10 \text{ (stat.)} \pm 0.01 \text{ (syst.).} \end{aligned}$$

Both the measured cross-section and the forward-backward asymmetry of b and c quarks are consistent with and provide a more stringent constraint on the Standard Model prediction.

A possible deviation from the Standard Model prediction is examined in terms of the compositeness scale Λ. We have obtained some most stringent lower limits on Λ_{eecc} and Λ_{eebb} at 95% CL.

Acknowledgements

My work has been accomplished in collaboration with many people: all of the members of VENUS collaboration, TRISTAN accelerator group and Nagashima group in Osaka University. First of all, I would like to thank them from my heart.

I would like to thank Professor Nagashima for giving a great chance to join the VENUS group in the TRISTAN experiment. His guidance and encouragement leads me to the interest in the High Energy Physics. I would like to thank Professor Matsui for welcoming me to study at KEK. Without his support I could not have completed my work.

Professor Haba often taught me how to study physics and how to overcome difficulties. I thank him from my heart. And I thank Dr. Takita for his kindness in my scientific and daily life. Also I thank Dr. Hara, Dr. Hazumi, Ms. Tsuzuki and fellows of Nagashima group.

At KEK, Professor Sakuda has given me helpful suggestions and guided me to the right way. I thank him from my heart. Dr. Yamada has given me useful suggestions about heavy flavour physics. I also thank Dr. Tsuboyama, Yamada, Uehara, Odaka, Kanzaki, Shirai, Ohama, Ishihara and other staff.

Finally, I thank my family for their support and kindness.

Contents

List of Figures

List of Tables

Chapter 1

Introduction

1.1 The Standard Model

Elementary particle physics is a branch of science to search for basic components of matter and to study interactions among them. Now we believe that matter is made up of quarks and leptons and that they interact with each other by exchanging intermediate bosons.

Quarks and leptons are fermions because of their half integral spin. Leptons carry integral charges, 0 or ± 1, in unit of positron charge (see Table 1.1). Members of leptons are electron (e), muon (μ) and tau (τ). Neutral members are called "neutrinos" and are assigned a subscript corresponding to charged partners; *i.e.* these are ν_e, ν_μ and ν_τ. A lepton which together associated neutrino make a doublet as shown in Table. 1.1

Quarks carry fractional charges of $+2/3$ or $-1/3$ and have an internal quantum number called "flavour". They are labeled as u, c, t for charge $2/3$ quarks and d, s, b for charge $-1/3$ quarks, respectively, which together forms a doublet. Each doublet of leptons and quarks forms a generation. Since c and b quarks have masses of about 3 and 5 GeV/c^2, respectively, by contrast to those of u, d and s quarks which are well below 1 GeV/c^2, they are called "heavy flavour"[1] quarks.

charge	Leptons			charge	Quarks		
0	ν_e	ν_μ	ν_τ	$+\frac{2}{3}$	u	c	t
-1	e	μ	τ	$-\frac{1}{3}$	d	s	b

Table 1.1: Fermions

There are four fundamental forces: electromagnetic, weak, strong and gravitational force. They are mediated by bosons with integral spin. Table 1.2 lists three of these. Gravity is the only interaction not listed here, because its effects are negligible in the present work. Any charged

[1]The recently discovered top quark with its mass of 180 GeV is also a heavy quark. But in this paper we use heavy flavour to denote c and b quarks

particles interact via the electromagnetic force, mediated by photon (γ). The intermediate vector bosons $W^{\pm}$ and Z^0 mediate the weak interaction. The weak force act on all particles, but the range of the weak force is limited by the boson masses; its typical range is 1/400 fm [†]. The strong interaction is the force between quarks. It is mediated by gluons (g) with typical range of about 1fm[‡]. Its strength is much larger than that for the weak force.

Interaction	Particle	Name
Electromagnetic	γ	photon
Weak	$W^{\pm}$, Z^0	weak boson
Strong	g	gluon

Table 1.2: Bosons

An important goal of elementary particle physics is to understand and unify all of the forces. For example, Maxwell unified the force of electricity and magnetism. The theory predicted and explained the existence of electromagnetic and light waves. An important principle underlying the electromagnetic theory is Lorenz invariance of space-time. The extension of Maxwell's theory to incorporate Quantum Mechanics leads to the theory of Quantum Electromagnetic Dynamics (QED). This theory has been tested by experiments with extreme precision.

In the last thirty years, the electromagnetic and weak interactions have been integrated into the electroweak theory [1]. The mathematical structure rests upon an underlying symmetry called a local gauge invariance; the electroweak theory is based on the gauge group SU(2)×U(1). For this reason, particles in Table 1.2 are called gauge bosons. The weak bosons, which are originally massless in the gauge group, get their mass through the vacuum expectation value of a Higgs field, as the result of spontaneous break down of the gauge symmetry [2]. However, there is no experimental evidence of the existence of the Higgs boson with spin 0. The existence of $W^{\pm}$ and Z^0 gauge bosons was predicted by the electroweak theory and they were eventually discovered at CERN in 1983 [3].

Quantum Chromo-dynamics (QCD) is also a gauge field theory of SU(3). It describes interactions of quarks and gluons and is based on the symmetry properties of their color charge. There are eight generators in SU(3) gauge group and they correspond to massless gauge bosons "gluons" carrying a color charge. The observation of three jets events in e^+e^- annihilation confirmed the existence of the gluon.

Due to its non-Abelian nature, gluons also interact with each other and the strength of the strong interaction increases as the distance between them increases. This feature is responsible for the "quark confinement"[4]. At short distances, namely at high momentum transfer, the

[†]The range of weak force is $\hbar c/m_W c^2$ = 200 MeV·fm / 80 GeV = 1/400 fm; 1 fm = 10^{-15}m

[‡]The long range force of the strong interaction is shielded by color confinement and the typical range is characterized by pion mass rather than gluon mass, hence $\hbar c/m_\pi c^2$ = 200 MeV·fm /130 MeV ~ 1.5 fm

[4]Quark confinement actually means that of color charge. In the perturbative QCD, the strength of color charge

coupling strength α_s becomes small. This effect, "asymptotic freedom", allows a perturbative treatment of the strong interactions at short distances.

The Standard Model in a gauge theory based on the symmetry groups SU(3)×SU(2)×U(1) and contains particles listed in Table 1.1 and 1.2 and the Higgs boson. All experimental data are consistent with the Standard Model so far, but this model contains many parameters which cannot be fixed naturally. Our intention is to test the Standard Model and also to compare results with a model beyond the Standard Model in this thesis.

To test the Standard Model, we chose the e^+e^- collision experiment for two reasons. First, a very high energy is necessary to investigate the elementary interactions at short distances. It is given by a large colliding beam accelerator. Second, the e^+e^- collision make clean signals compared to hadron-hadron collision. These features allow us to test the Standard Model precisely.

An e^+e^- collider called TRISTAN was constructed to search the top quarks and started operation in 1986. Although, the top quark was not discovered at TRISTAN energy ($\sqrt{s} \leq 64$ GeV). It is the energy region where the interference between the electromagnetic and weak force is significant. For example, the effect of the interference is clearly seen in the differential cross section of the lepton and quark pair production. In the next section, we describe the quark pair production at TRISTAN energy.

coupling (coupling among the quarks and gluons) is expressed by $1/ln(R^{-1})$ as a function of their distance (R). Namely the strength of the strong interaction increases as the distance between them increases. Therefore quarks are confined and don't exist by itself.

1.2 Quark pair production in e^+e^- annihilation process

In the lowest order of the electroweak theory, Feynmman diagram of the quark pair production in e^+e^- annihilation process is shown in Fig. 1.1. These quark pairs are produced via single photon or Z^0 boson propagation.

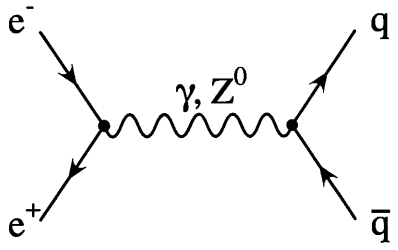

Figure 1.1: Feynman diagram of quark pair production in e^+e^- annihilation process.

The differential cross-section is expressed as the following formula [58],

$$\frac{d\sigma}{d\cos\theta} = \frac{3\alpha^2}{4s}[\, A(1+\cos^2\theta) + B\cos\theta \,], \tag{1.1}$$

with

$$A = e_e^2 e_q^2 + 2e_e e_q v_e v_q \Re(\chi) + (v_e^2 + a_e^2)(v_q^2 + a_q^2)\,|\chi|^2 \tag{1.2}$$

and

$$B = 4e_e e_q a_e a_q \Re(\chi) + 8 v_e v_q a_e a_q \,|\chi|^2, \tag{1.3}$$

where θ is the polar angle of the quark with respect to the electron beam direction, α is fine structure constant, s is square of the center of mass energy in e^+e^- collision, e_i is an electric charge in the unit of a positron charge, v and a are vector and axial vector coupling constant, respectively, and χ is a propagation term of Z^0 boson. The last three variables are given as

$$a_q = \frac{e_q}{|e_q|} = \begin{cases} 1 & (q = u, c, t) \\ -1 & (q = d, s, b) \end{cases}, \tag{1.4}$$

$$v_q = \frac{e_q}{|e_q|} - 4e_q \sin^2\theta_W = \begin{cases} 1 - \frac{8}{3}\sin^2\theta_W & (q = u, c, t) \\ -1 + \frac{4}{3}\sin^2\theta_W & (q = d, s, b) \end{cases} \tag{1.5}$$

and

$$\chi = \frac{1}{16\sin^2\theta_W \cos^2\theta_W} \frac{s}{s - M_Z^2 + iM_Z\Gamma_Z}, \tag{1.6}$$

where M_Z, Γ_Z and $\sin\theta_W$ are the mass, decay width of Z^0 boson and the Weinberg angle, respectively.

Forward-backward asymmetry $A_{\rm FB}$ is defined as

$$A_{\rm FB} = \frac{\int_0^1 \frac{d\sigma}{d\Omega} d\cos\theta - \int_{-1}^0 \frac{d\sigma}{d\Omega} d\cos\theta}{\int_{-1}^1 \frac{d\sigma}{d\Omega} d\cos\theta} = \frac{3B}{8A} \tag{1.7}$$

$$= \frac{3}{2} \frac{e_e e_q a_e a_q \Re(\chi) + 2 v_e v_q a_e a_q \, |\chi|^2}{e_e^2 e_q^2 + 2 e_e e_q v_e v_q \Re(\chi) + (v_e^2 + a_e^2)(v_q^2 + a_q^2) \, |\chi|^2} \ , \tag{1.8}$$

where A and B are the variables defined in Eq. 1.2 and 1.3, respectively, and the term including $\Re(\chi)$ denotes the interference between γ and Z^0 boson. Forward-backward asymmetry comes from V–A structure of weak current in the Standard Model. It indicates parity violation in the electroweak theory. Figure 1.2 shows a prediction of the Standard Model on $A_{\rm FB}$ as a function of the center of mass energy. There were many previous experiments at the PEP ($\sqrt{s}$ = 29 GeV), PETRA ($\sqrt{s}$ = 35 $\sim$ 44 GeV), LEP and SLC ($\sqrt{s} \sim$ 91 GeV) collider. At TRISTAN energy ($\sqrt{s}$ = 58 GeV) it has the largest negative value as found in the Fig.1.2, because the interference between γ and Z^0 exchange amplitude becomes large. The measurement of $A_{\rm FB}$ at TRISTAN energy is, therefore, very important to test the Standard Model.

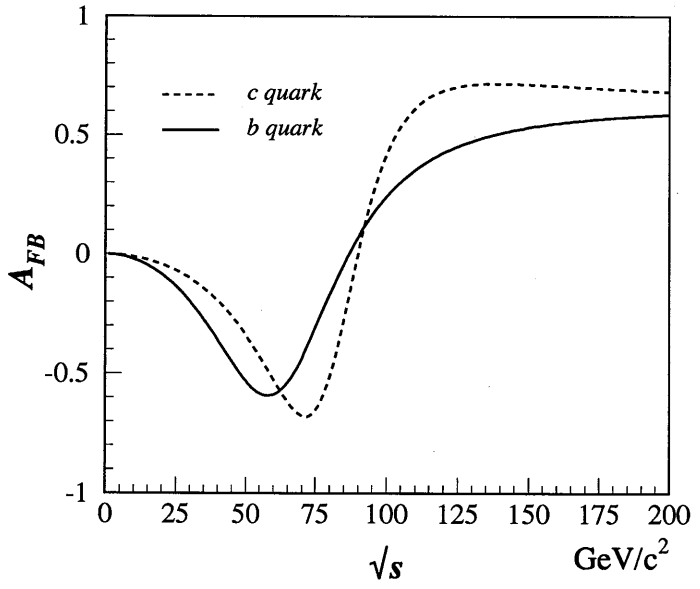

Figure 1.2: Forward-backward asymmetry of c and b quarks.

1.3 Heavy flavour tag using their semi-leptonic decays

In order to measure A_{FB} of the heavy quarks, we have to identify the quark flavour and determine the direction of the quark or anti-quark. In reality, what we observe are not quarks but hadrons which contain quarks as their constituents. For instance, $c\bar{c}$ quarks produced in the reaction in Fig. 1.1, which we call a primary c quarks, subsequently pick up quarks from vacuum and form hadrons. When the c ($\bar{c}$) quark pick up $\bar{u}$ (u) or $\bar{d}$ (d) and form a spin 1 meson, it is called D^*. Finally we observe its decay products.

There are three distinct techniques to identify quark flavours in the hadrons; D^* tag for c quark, lifetime tag for b quark and prompt lepton tag for c and b quarks,

1. Since primary c quarks produced in e^+e^- annihilation tend to form D^* meson, they can be tagged by D^*. D^* is characterized by its small Q-value in its decay $D^{*\pm} \rightarrow D^0\pi^\pm$. We can identify D^* by reconstructing D^0 associated with soft π and examining the reconstructed mass difference $(M_{D^*} - M_{D^0})$.

2. Since B hadrons, which include b quark as their constituents, have relatively long lifetimes (in a sense their decay length is measurable), we can identify the secondary decay vertices by the precise tracking device. By requiring the decay vertex well separated from the production point, we can distinguish b quark production from those of other quarks.

3. Prompt leptons coming from the semi-leptonic decays are the most remarkable signature of the production of c or b quarks. The tagging of these leptons is, therefore, an effective mean to identify the heavy flavour quarks and to derive an information of the quark charge (quark or anti-quark) at the same time. In the case of b quarks, *e.g.* $B^0(= b\bar{d}) \rightarrow D^{*+}l^-\bar{\nu}$, the negative sign of the lepton charge ($Q = -1$) tells the sign of b quark charge.

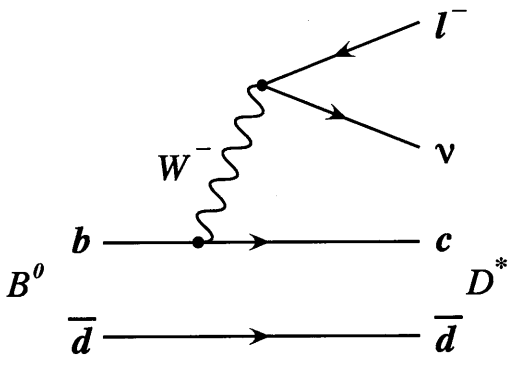

Figure 1.3: Semileptonic decay of a B meson: $B^0 \rightarrow D^{*+}l^-\bar{\nu}$

Since VENUS contains in itself excellent devices such as the lead-glass calorimeter (LG), transition radiation detector (TRD) and muon chamber system to distinguish leptons (e or

μ) from the other hadrons, we apply the prompt lepton tag to measure the forward-backward asymmetry of the heavy quarks in this thesis. Previous measuremnets have been performed with prompt electron or muon tagging [4,5]. But this is the first analysis to succeed in prompt muon tagging at closer region to the quarks direction. The details of the prompt lepton tag are described in Chap. 4 and 5.

As will be described in Chap. 1.4, the prompt leptons tend to have larger momentum than the leptons from the background process like $\pi^{\pm} \to \mu^{\pm}\nu_{\mu}$, $K^{\pm} \to l^{\pm}\nu_{l}\pi^{0}$ or $\gamma \to e^{+}e^{-}$. We can distinguish the prompt leptons by their momenta. But, to make presice measurement, we must well understand on backgrounds for prompt leptons and reduce the systematic errors. Hadron misidentifications are evaluated by control samles of pion and Monte Carlo simulation, which is also described in Chap. 4 and 5.

1.4 Quark fragmentation

Quarks once produced in $e^{+}e^{-}$ annihilation are governed by Quantum Chromo-dynamics (QCD). These quarks cannot be observed directly, but appear in groups of hadrons which are collimated toward the direction of the original quark. Such a group of collimated hadrons is called "jet".

The evolution of jets according to QCD can be understood as illustrated in Fig 1.4.

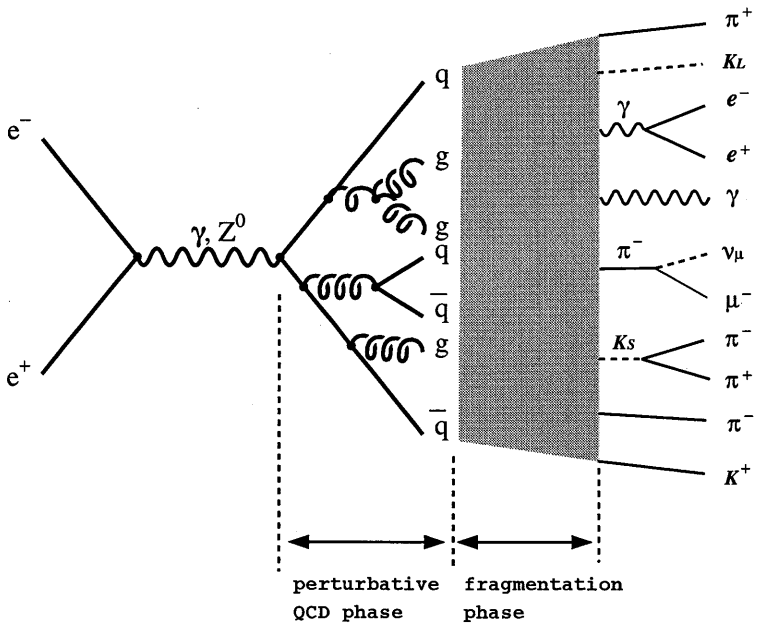

Figure 1.4: QCD processes

The first step of the evolution is the perturbative phase. Since the energy scale is large and the coupling strength of the strong interaction α_s is small in this phase, the perturbative QCD

theory can be applied for each process, where quarks radiate gluons and gluons split into quark anti-quark pairs or gluon pairs.

The second is the fragmentation phase. In this phase the perturbative theory cannot be applied because of a larger α_s, so phenomenological models must be used to describe the fragmentation processes. Assuming that the transition amplitude for a fast moving heavy quark Q to fragment into a hadron $H = (Q\bar{q})$ and a light quark q is proportional to the inverse of the energy transfer $\Delta E^{-1} = (E_H + E_q - E_Q)^{-1}$, the following parametrization has been proposed by Peterson *el al.* [6] for heavy quark fragmentation:

$$D(z) \propto \frac{1}{z}\left(1 - \frac{1}{z} - \frac{\epsilon}{1-z}\right)^{-2}. \tag{1.9}$$

The above parameterization is known to reproduce several experimental data well and used widely in modelling of heavy quark fragmentation. The only parameter of the model ϵ is related to the squared ratio of the effective mass of the light quark to that of the heavy quark;

$$\epsilon \approx \frac{m_q^2}{m_Q^2}, \tag{1.10}$$

and z is defined as

$$z = \frac{(E + p_{//})_{\text{hadron}}}{(E + p)_{\text{quark}}}. \tag{1.11}$$

Here $p_{//}$ is the longitudinal momentum with respect to the quark direction, $(E + p)_{\text{quark}}$ is the sum of the energy and momentum of the quark. Figure 1.5 shows shapes of the Peterson function (Eq. 1.9) for various values of parameter ϵ. The energy spectrum of the heavy quarks are harder than that of the light quarks due to these heavy masses.

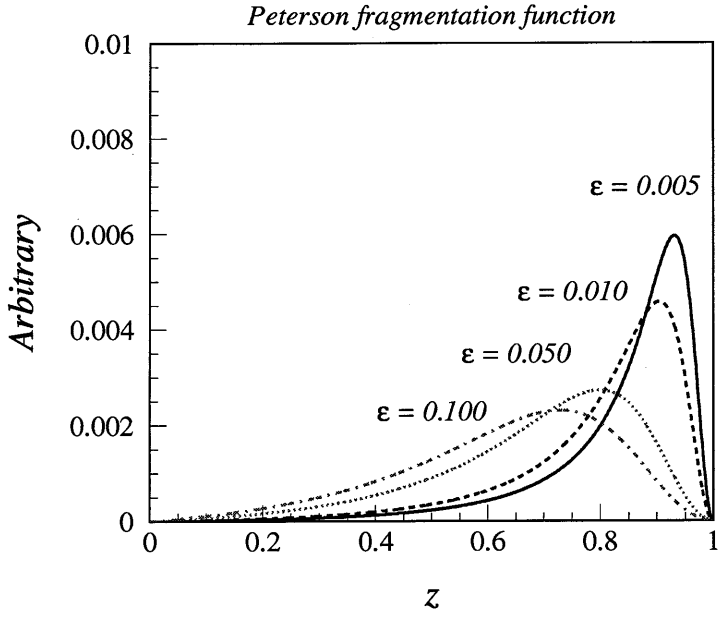

Figure 1.5: Shapes of the Peterson function for various values of parameter ϵ

Experimentally, it is hard to determine z on an event-by-event basis. Instead, the scaled energy of the hadron, x as defined bellow, is usually used for the expression of the results.

$$x = \frac{E_{\rm hadron}}{E_{\rm beam}}. \tag{1.12}$$

This variable, which includes the effect of gluon emission in perturbative phase, is used in this work.

As a result of hard energy spectrum of the c and b hadrons, its decay products tend to have larger momentum. A tagging of the prompt leptons with large momentum, therefore, provides a clean identification of the heavy flavour quarks events.

1.4.1 Determination of the thrust and jet axes

Similar to the fragmentation parameter of z, it is hard to determine the quark direction. We define the quark direction as an unit vector of the thrust axis ($\vec{n}$), which is defined so as to maximize the value of thrust (T).

$$T = \max \Sigma \frac{|\vec{p}_i \cdot \vec{n}|}{|\vec{p}_i|} \tag{1.13}$$

The thrust axis is uniquely determined in a event. In the VENUS detector, the quark direction can be determined by the thrust axis with an accuracy of 6°. The sign of the quark direction is assigned according to the charge of tagged leptons.

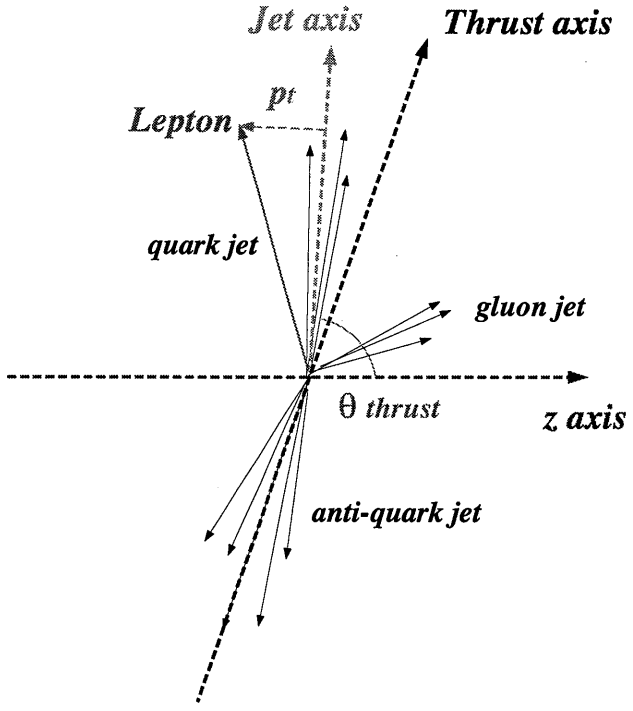

Figure 1.6: Schematic view of thrust axis and jet axis.

To separate leptons from semi-leptonic decays of c and b quarks effectively, we also define the direction of a mother hadron in their decays. Because the thrust axis includes the effect of gluon emission as illustrated in Fig. 1.6, we use the jet axis as the direction of a mother hadron. To form jets, we use the clustering of JADE algorithm [7], which is done as follows. At first, the scaled invariant mass square y_{ij} is calculated for all pairs of particle i and j as follows,

$$y_{ij} = \left(\frac{M_{ij}}{E_{\rm vis}}\right)^2 \tag{1.14}$$

where M_{ij} is the invariant mass of the particles i and j and $E_{\rm vis}$ is the total visible energy defined in Chap. 3.2.1. Among all pairs the particle pair with smallest invariant mass is regarded as a pseudo-particle. Then this procedure is repeated until the scaled invariant mass square (y_{ij}) of the pseudo-particle exceed a threshold value[5]. The remaining pseudo-particles are defined as jets. A jet axis is given as a momentum sum vector of the jet. Hereafter we define the transverse momentum p_t as those against the jet axis.

1.5 Quark compositeness

Using the present results of the measurements on the total cross-section and the forward-backward asymmetry, we will check the consistency with the Standard Model predictions. The possible deviations from the Standard Model predictions would signal new physics.

As a mean to test the Standard Model, we take the contact interaction approach [8, 9]. If quarks are made of constituents, new interactions among quarks should appear at the short distance which may be expressed as the inverse of the compositeness mass scale of Λ. Therefore if the Standard Model predictions are consistent with the measured values, we can set the constraints as the lower limits on the compositeness scale.

Eichten et al. presented the general formalism of the lowest dimensional contact interactions which respect chiral invariance. Based on this approach, lower limits of a few TeV at 95% CL have been set on the compositeness scale in purely leptonic contact interactions ($eeee, ee\mu\mu, ee\tau\tau$) by PEP, PETRA, TRISTAN and LEP experiments in e^+e^- annihilation [10–17]. The compositeness scale of purely quark contact interactions has been also studied at the CERN $p\bar{p}$ collider and the Tevatron [20–25]. However, there have been few published limits on the contact interactions including both quarks and leptons. This type of contact interactions can be studied in the heavy quark production in e^+e^- annihilation.

The effective Lagrangian in the process $e^+e^- \to q\bar{q}$ is defined as,

$$\mathcal{L}^{\rm contact} = \frac{g^2}{\Lambda^2} \sum_{i,j=L,R} \eta_{ij}\ \bar{e}_i\gamma^\mu e_i\ \bar{q}_j\gamma_\mu q_j. \tag{1.15}$$

[5]In this thesis, we choose the threshold value as 0.05.

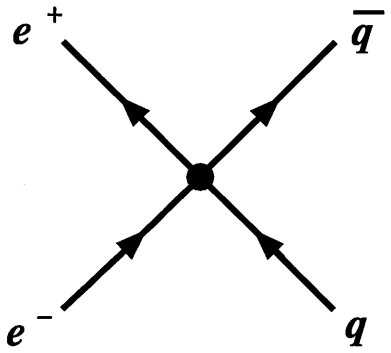

Figure 1.7: Contact interaction of $e^+e^- \to q\bar{q}$ process

Here, subscript of L, R denote chirality of an electron or quark current. By convention, the unknown coupling constant g is set to $g^2/4\pi = 1$ and the magnitude of the coefficients η is set to be unity. Various types of interactions, which are reflected to the choice of η_{ij} parameters, are considered as summarized in Table 1.3.

Model	η_{LL}	η_{RR}	η_{LR}
$LL^{\pm}$	± 1	0	0
$RR^{\pm}$	0	± 1	0
$AA^{\pm}$	± 1	± 1	± 1
$VV^{\pm}$	± 1	± 1	∓ 1

Table 1.3: Different models of the four fermions contact interaction

This effects are investigated as the deviation from the Standard Model by using the measured values of the forward-backward asymmetry and the total cross-section of c and b quarks. This analysis is performed in Chapter 7.

1.6 Outline of this thesis

The outline of this thesis is as follows. In Chapter 2, we describe the e^+e^- collider TRISTAN and VENUS detector. The descriptions of the event trigger and the data acquisition system are also contained. In Chapter 3, we describe how events are reconstructed from obtained data and then how backgrounds are reduced. Chapter 4 and 5 contain description of prompt electron and muon tags, respectively. In Chapter 6, we derive results on the measurement of the total cross-section σ and the forward-backward asymmetry $A_{\rm FB}$. Finally, we discuss the obtained results and set lower limits on compositeness scale Λ in Chap. 7.

Chapter 2

Experimental Apparatus

The data used in this analysis were collected by a general purpose magnetic spectrometer VENUS[1] at electron-positron collider TRISTAN[2], which is located at National Laboratory for High Energy Physics (KEK) in Tsukuba, Japan. Figure 2.1 shows a layout of TRISTAN. It consists of three parts; injectors of linear accelerator (LINAC), Accumulation Ring (AR) and Main Ring (MR). VENUS detector is located at one of the four interaction points FUJI on MR. A brief introduction to TRISTAN and VENUS detector is given below.

2.1 TRISTAN

TRISTAN started operation in November 1986. Then great efforts have been put in raising the beam energy of TRISTAN as much as possible. To achieve this goal, more than thirty cavities were added in the TRISTAN ring until summer of 1989. Finally, maximum center-of-mass energy of 64 GeV was achieved in December 1989. The above period was called as TRISTAN Phase–I.

In February 1990, when SLC[3] and LEP[4] collider started operation at higher center-of-mass energy ($\sqrt{s} = 91$ GeV) than TRISTAN, TRISTAN Phase–II operation was started. In the second period, the emphasis of the operation was set on obtaining as high luminosity as possible. A pair of superconducting quadrupole magnets (QCSs) were installed at each collision points until May 1991. The center-of-mass energy was fixed at 58 GeV to obtain the maximum luminosity. As a result, a peak luminosity of 1.02 pb^{-1}/day was achieved on 23 Nov 1991. Total integrated luminosity from November 1986 to May 1995 is about 400 $pb^{-1\dagger}$.

[1] VErsatile National laboratory and Universities Spectrometer
[2] Transposable Ring Intersecting STorage Accelerator in Nippon
[3] Stanford Linear Collider; located at Stanford Linear Accelerator Center, USA
[4] Large Electron Positron collider; located at CERN, Switzerland
$\dagger$ 1 pb^{-1}=10^{36} cm^{-2}

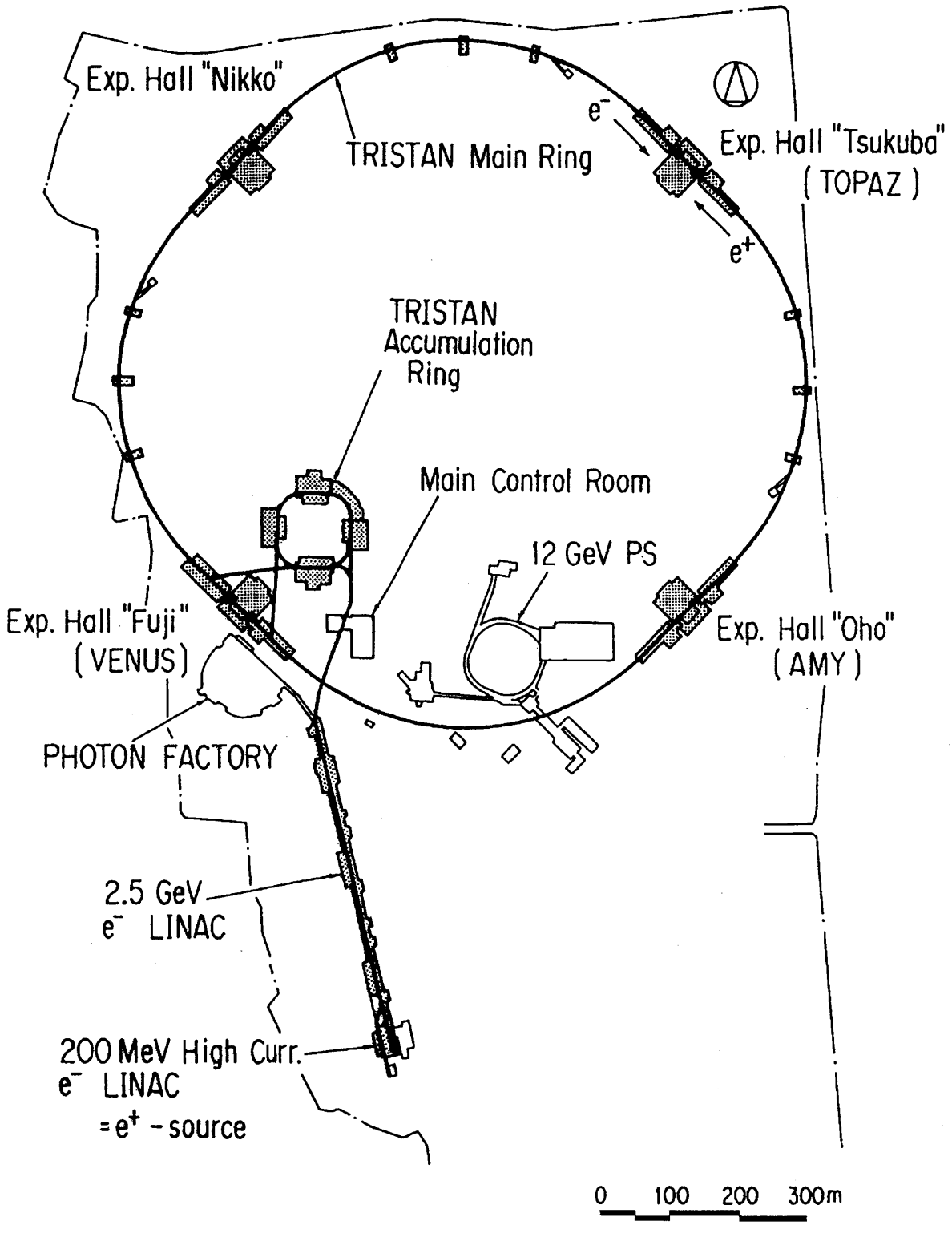

Figure 2.1: Layout of TRISTAN

2.1.1 Injectors (LINAC)

Injectors consists of two parts; a positron generator and a main linear accelerator (LINAC). Furthermore a positron generator consists of three parts; a high current pre-accelerator, a conversion section and a post-accelerator.

A pre-accelerator is a high current e^- linear accelerator of 10 A and accelerates electrons up to 200 MeV. Then the electron beam strike a tantalum target. In the target, electrons induce electro-magnetic showers, *i.e* positrons are generated through electron-positron pair production. Positrons with certain momentum range are selected with a solenoid magnet and then accelerated by a post-accelerator up to 250 MeV.

Main LINAC, which is 400 m long, accelerates electrons and positrons up to 2.5 GeV. Electrons and positrons accelerated in LINAC are transferred to AR.

2.1.2 Accumulation ring (AR)

Accumulation ring (AR) is a booster whose circumference is 377 m and stores electrons or positrons from LINAC to the beam current more than 10 mA. After accumulation, an electron or positron beam is accelerated up to 8.0 GeV and then transferred to MR.

2.1.3 Main ring (MR)

Main ring (MR) has a circumference of 3018 m and consists of 4 straight sections of 193 m length, and 4 arc sections. Two electron bunches and two positron bunches circulate in opposite directions (electrons circulate clockwise and positrons, counter-clockwise) and collide with each other at the mid-points of the straight section. So there are 4 interaction points[5] at which the colliding beam detectors are located. The beams collide every 5 μs. A large portion of the straight section is allocated for RF[6] cavities which accelerate the beams from the injection energy to the required collision energy and then compensate for a large energy loss due to synchrotron radiation.

The energy loss (ΔE) due to synchrotron radiation is expressed as

$$\Delta E \cong 0.0885 \times \frac{E^4}{\rho} \quad \text{(MeV/turn)}, \tag{2.1}$$

where E is the beam energy in GeV and ρ is the radius of curvature in meter. The amount of it is 254 MeV/turn at $E = 29$ GeV.

The beam energy spread σ_E is expressed as

$$\frac{\sigma_E}{E} = 0.857 \times 10^{-3} \times \frac{E}{\rho}, \tag{2.2}$$

which amounts to 49 MeV at E=29 GeV. The energy spread varies according to the frequency shift (Δf_{RF}) applied to the accelerator by RF cavities. Δf_{RF} is stable around 3 kHz during the runs of the present experiment.

[5]Four interaction points are called OHO, TSUKUBA, NIKKO and FUJI, respectively.

[6]RF means "Radio Frequency", practically it is 508.6 MHz

TRISTAN-MR parameters	
Circumference	3018 m
Bending radius (ρ)	246.5 m
Injection beam energy	8.0 GeV
Max. beam energy	32.0 GeV
Revolution frequency (f_{rev})	99.33 MHz
Beam current (I_e) per bunch	$\sim$ 8 mA
Number of bunches (N_b)	4 = 2 (e^+) + 2 (e^-)
Beam size at collision point (σ_x^* / σ_x^* / σ_z^*)	300 μm / 10 μm / 1 cm
Max. luminosity	1.6×10^{31} cm^{-2} sec^{-1}
Max. integrated luminosity per day	1.02 pb^{-1}/day
Beam life	3 $\sim$ 4 h

Table 2.1: Parameters of TRISTAN-MR.

The beam has approximately Gaussian shape with effective r.m.s.[7] widths of about 300 μm in the horizontal direction, 10 μm in the vertical direction, and 2 cm in the beam direction at the intersection points in the TRISTAN Phase–II operation. Typical lifetime of the beam is 3$\sim$4 hours during a physics run. The parameters of MR are listed in Table 2.1. The luminosity is one of the most important parameters in the colliding beam experiments. The event rate, dN/dt, for a reaction having total cross-section σ, is related to the luminosity $\mathcal{L}$ of the machine by

$$\frac{dN}{dt} = \sigma \cdot \mathcal{L} . \tag{2.3}$$

For an e^+e^- collider, $\mathcal{L}$ is often expressed as follows

$$\mathcal{L} = \frac{n_{e^+} n_{e^-}}{4\pi\sigma_x^*\sigma_y^*} \cdot f_{rev} \tag{2.4}$$

$$= \frac{I_{e^+} I_{e^-}}{4\pi e^2 \sigma_x^*\sigma_y^* f_{rev}} \tag{2.5}$$

The beam current (I_e) is expressed as follows,

$$I_e = e n_e f_{rev} \tag{2.6}$$

where n_e is the number of electron (positron).

The luminosity is determined by measuring the number of Bhabha scattering (e^+e^- elastic scattering) events [26].

[7] "r.m.s." means root mean square.

2.2 VENUS

VENUS is a general purpose magnetic spectrometer designed to study various reactions in the e^+e^- annihilation. Figure 2.2 shows a schematic view of VENUS.

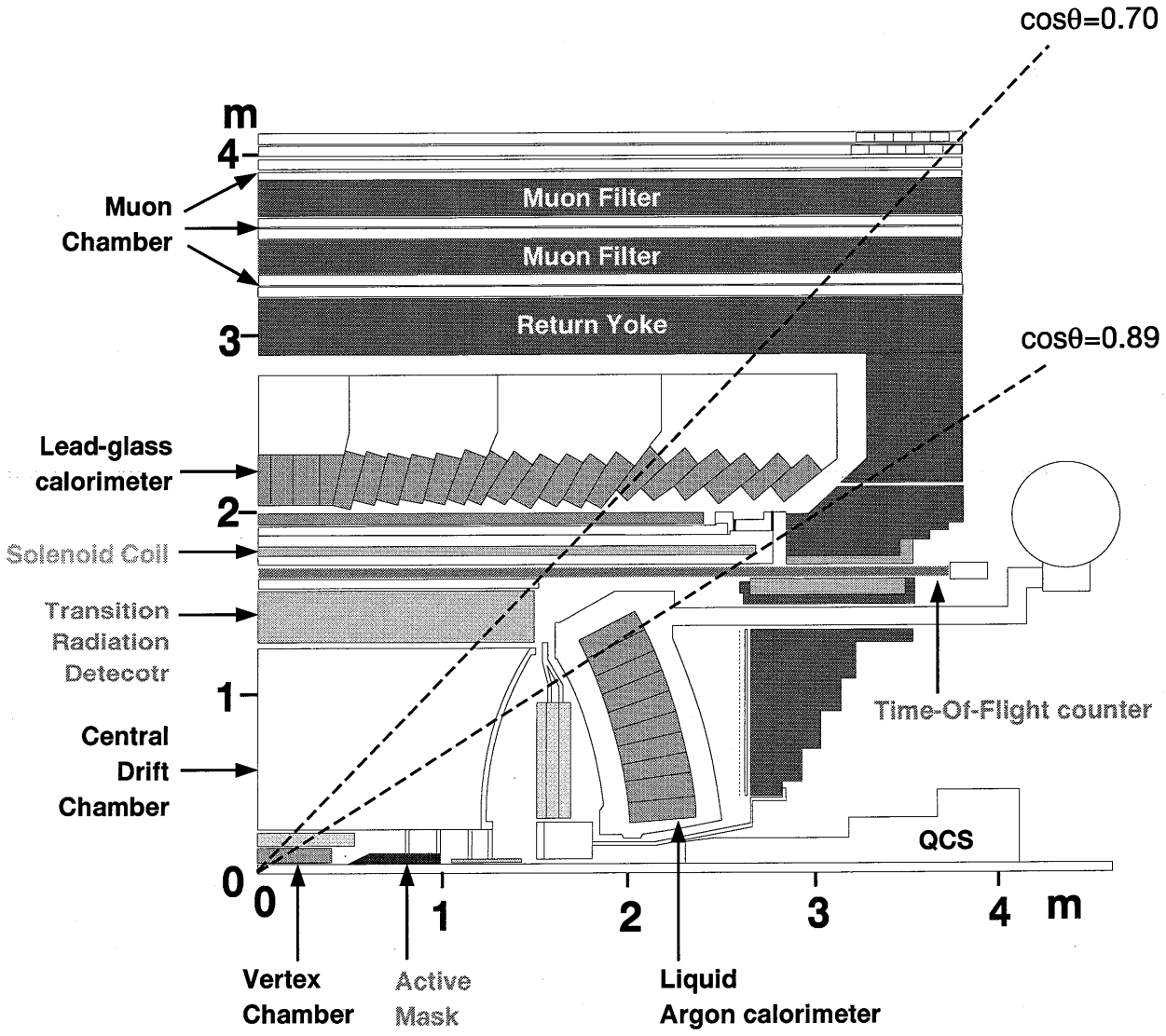

Figure 2.2: A schematic view of VENUS

The coordinate system of VENUS is shown in Fig. 2.3. The z-axis is defined as along the e^- beam direction. The y-axis is defined as vertical direction. θ and ϕ are defined as polar and azimuth angle, respectively.

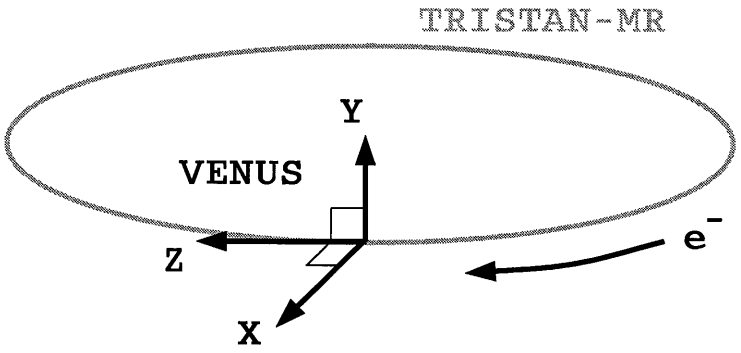

Figure 2.3: The coordinate system of VENUS

Detector component	inner / outer radius [cm]	length or z position [cm]	polar angle $\|\cos\theta\|$	radiation length [X_0]
Beam pipe	4.8 + 0.11(thickness)	24	–	0.003
VTX chamber	5.4 / 14.4	60	0.90	0.034
CDC inner	25.0	~250		0.007
gas	–	–	–	0.0015
outer	126.0	300	0.75	0.035
TRD	127.0 / 157.7	296	0.68	0.219
TOF	163.9 / 168.1	233	0.81	0.099
LG	197.0 / 230.0	615	0.80	18.0
LA	–	–	0.79–0.99	20.3
AM	4.4/10.0	–	0.989–0.999	
Muon chamber	–	±380	0.70	

Table 2.2: Geometries of VENUS components

2.2.1 Vertex chamber (VTX)

The vertex chamber (VTX) is located at innermost place in the VENUS detector. The purpose of it is to precisely determine the decay vertex of hadrons such as B meson in the x-y plane. It is a jet-type drift chamber which has the length, inner and outer radii of 60.0, 5.4 and 14.4 cm, respectively. The chamber consists of 12 drift sectors, each of which has 16 sense anode wires, as shown in Fig. 2.4 [27]. The anode wire planes of all sectors tilt by the angle of about 15° from the radial direction. This is mainly due to optimization of high quality sensitive region for the particles with any azimuthal angle. Tilting is also useful for resolving what is called the left-right ambiguity of a track. To achieve good spatial resolution of $\sim 50\mu m$, we use what is called slow gas, a mixture of 92% carbon-dioxide (CO_2) and 8% ethane (C_2H_6) at 3 atmospheric pressure. This provides us large gas volume of uniform electron drift velocity ($\sim$ 7 mm/μs). Since the drift velocity is proportional to the electric field and inversely proportional to the gas density, the electric field, pressure and temperature of the gas should be controlled with stability of more than 0.1 % in order to keep the drift velocity constant.

Beam pipe, which is made of beryllium, is a part of VTX chamber. The material was chosen for its low density and strength against pressure. Its thickness, outer radius and length are 0.11, 9.8 and 24 cm, respectively. It is covered by 50 μm thick titanium sheets to absorb X rays from beam breamsstraulung.

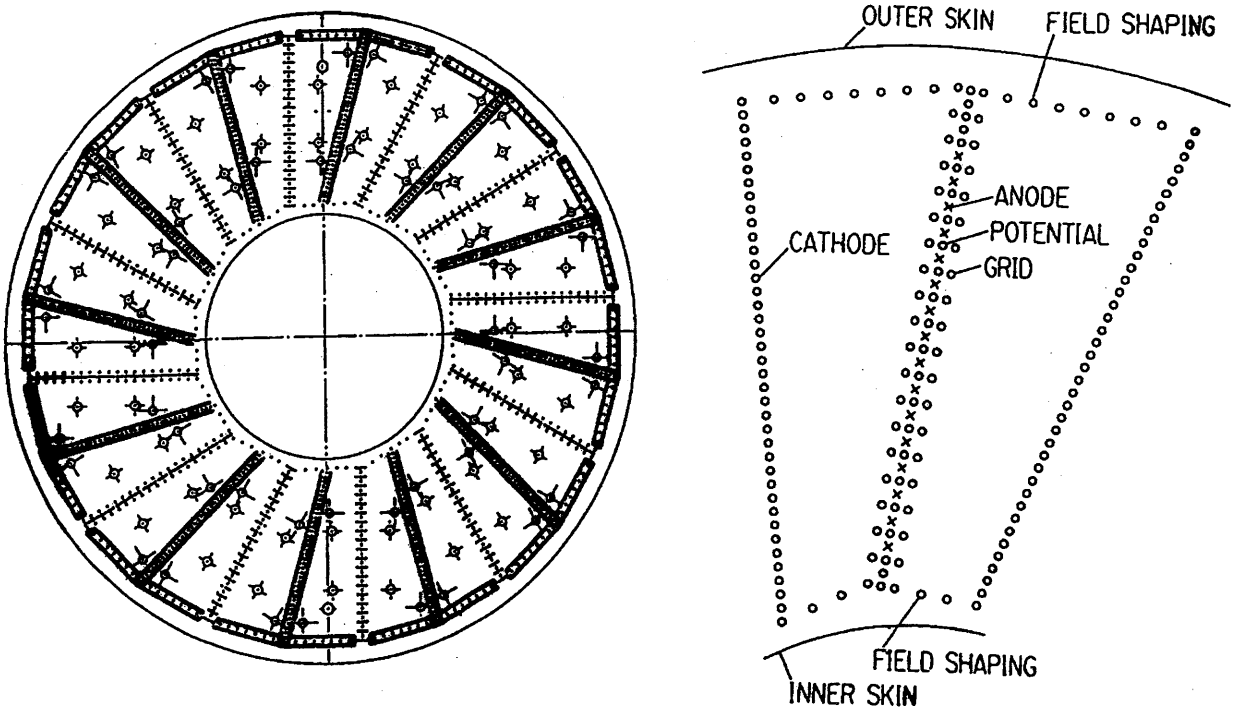

Figure 2.4: Schematic view of VTX

2.2.2 Active mask (AM)

Active mask is a pair of cylindrical sandwich calorimeters [28]. Its role is to measure the number of Bhabha events and stop the particles from the events such as beam-gas or beam-beampipe interaction, so it is called "active mask". It consists of 0.1 cm thick lead sheets and plastic scintillation fiber sheets as shown in Fig. 2.5 and covers small polar angle regions of $2.6° \sim 8.6°$, $171.4° \sim 177.4°$.

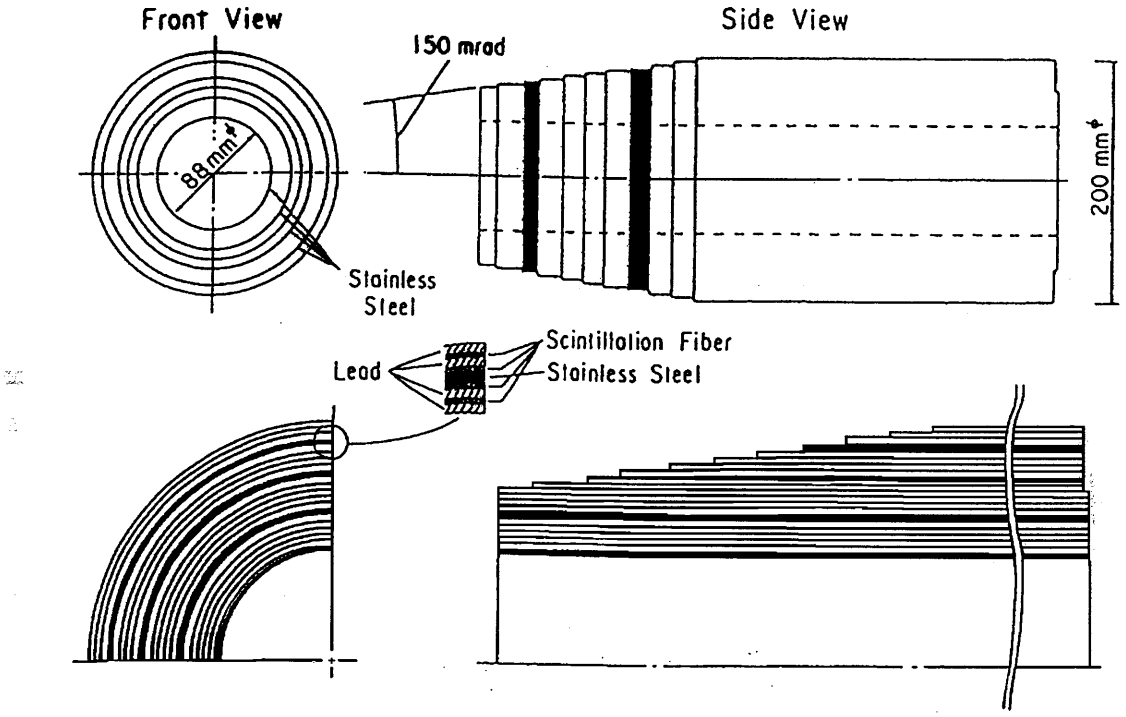

Figure 2.5: Schematic view of active mask

2.2.3 Central drift chamber (CDC)

Central Drift Chamber (CDC) is a cylindrical multi-wire drift chamber [29] and is the main tracking device of the VENUS detector. The inner and outer radii of the gas volume are 25 cm and 126 cm, respectively. Its length is 300 cm. It is filled with HRS gas ($Ar:CO_2:CH_2$=89:10:1). This mixture was chosen because of its good properties for a long-term operation for large drift chamber. It is nonflammable, stable against aging and less expensive.

For the track reconstruction in the x-y projection (normal plane to the beam axis), 20 axial layers of drift cells are provided. Every two layers are rotated by half a cell width and combined into one double layer. The z coordinate is determined by using 9 stereo layers tilted by 3 ° with respect to the z axis. All layers are grouped to form 10 "superlayer"s consisting of a pair of axial layers and one stereo layer, except for innermost superlayer. Furthermore, a half of the

superlayers have an offset of one quarter of a cell width with respect to the other superlayers, in order to avoid a radial alignment of worse quality regions. If we ignore this small offset, the arrangement of the cells has a 32-fold symmetry in azimuth. The symmetry allows us to design a simple and efficient track trigger logic. One rectangular drift cell of 1.7 cm high and typically 2 cm wide contains one sense wire at the center and surrounding 6 potential wires. The sense wires are gold-plated 30 μm-thick tungsten-rhenium (3%) alloy and stretched with the tension of 60 gW. The potential wires are gold-plated 140 μm-thick molybdenum with the tension of 300 gW. Molybdenum was chosen because of its large yield. It makes easier to replace defective wires after completing the chamber. The maximum gravitational sag is 250 μm for the sense wires and 600 μm for the potential wires. The drift field is provided by applying a positive high voltage, typically 2.1 kV, to the sense wires. The potential wires are grounded. The electric field is almost radial near the sense wire up to a distance of about 5 mm, while the effect of the potential wires is significant outside the region.

Figure 2.6 is a view of CDC in the x-y plane. Charged particles produced at a central region $|\cos\theta| \leq 0.75$ cross a sensitive region of all layers.

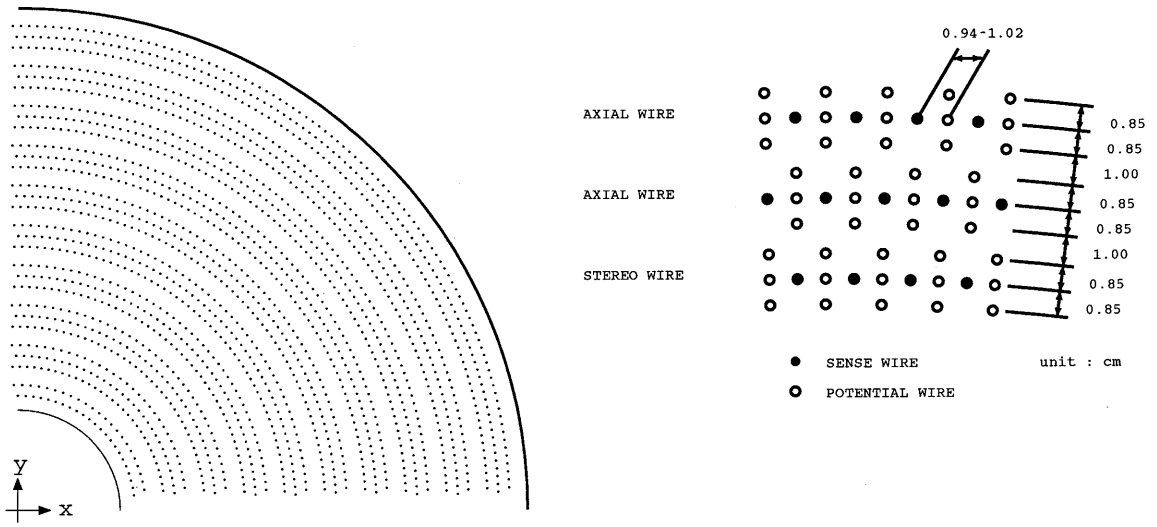

Figure 2.6: A (a) x-y view and (b) cell configuration of CDC

The endplates are 2 cm-thick aluminum plates having a curved shape. The shape was chosen to minimize the deformation due to the wire tension. The maximum deformation was measured to be about 0.05 cm, consistent with the calculation. The wire tension applied to the endplates, amounting to 9 ton in total, is supported by the outer cylinder made of 0.5 cm-thick CFRP (carbon-fiber reinforced plastic). The use of CFRP allows us to reduce the material thickness to approximately 1/2 in the case of aluminum. The VENUS CDC is the first large-size drift chamber that has employed CFRP as a major component of the mechanical structure. The inner cylinder, made of 0.1 cm-thick CFRP, serves as only a gas seal. The inside surfaces of

the cylinders are lined with aluminum foil, in order to eliminate outgasses and provide a good electrical property.

2.2.4 Transition radiation detector (TRD)

The transition radiation detector (TRD) is a large cylindrical detector, extending from 127 cm to 157.7 cm radially and 296 cm in z direction. It covers the angular region of $|\cos\theta| \leq 0.7$ [30].

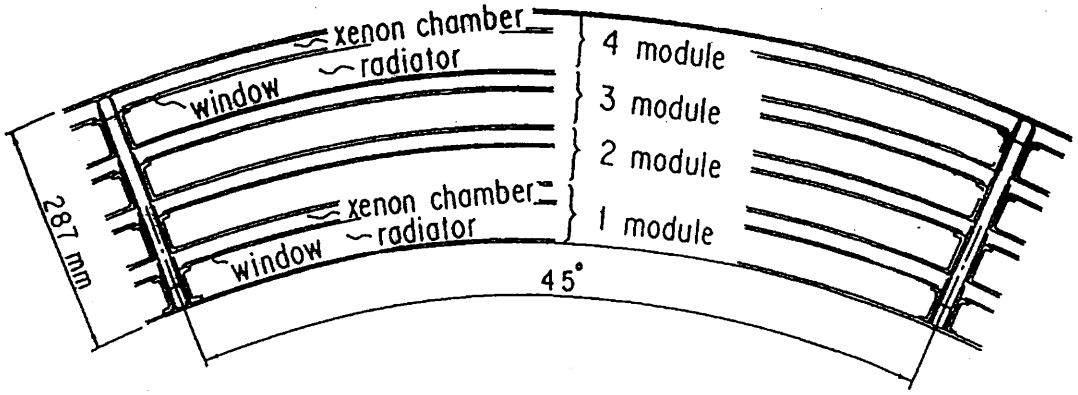

Figure 2.7: Schematic view of TRD

When a charged particle of a Lorentz factor $\gamma \geq O(1000)$ traverses the boundary of two media, having different dielectric constants, an X-ray called as "transition radiation" is produced along the particle trajectory. The differential flux is expressed by the following formula,

$$\frac{d^2S}{d\omega d\theta} = \frac{2\alpha\theta^3}{\pi}\left(\frac{1}{1/\gamma^2+\omega_1^2/\omega^2+\theta^2} - \frac{1}{1/\gamma^2+\omega_2^2/\omega^2+\theta^2}\right)^2. \tag{2.7}$$

where ω, $\omega_{1,2}$ are the frequency of X-ray and plasma frequencies[8] of the media, respectively, α is the fine structure constant ($\alpha = 1/137$) and θ is the emission angle with respect to the particle trajectory. The total energy of the radiation is given as

$$S = \frac{\alpha}{3}\frac{(\omega_1-\omega_2)^2}{\omega_1+\omega_2}\gamma \simeq \frac{\alpha}{3}\omega_1\gamma \qquad (\text{for } \omega_1 \gg \omega_2) \tag{2.8}$$

and is found to be proportional to Lorentz factor γ.

TRD consists of two components. One is a "radiator box" which contains polypropylene fibers (ω_1=20eV) and a helium gas (ω_2=0.28eV). The other is an X-ray chamber which has a thickness of 2 cm and is filled with gas mixture (Xe:CH_4=90:10) to detect the transition

[8]Plasma frequency of a medium are related as follows, $\omega = \sqrt{ne^2/\varepsilon_0 m}$, where n is refractive index of the medium, e is electric charge, ε_0 is a dielectric constant of vacuum and m is mass of the electron.

radiation. TRD is divided into eight sectors in azimuth as shown in Fig. 2.7 and each sector has four layers of the radiator box and X-ray chamber. Thus 32 pairs of radiator box and X-ray chamber comprise the detector. The total radiation thickness of TRD is 0.18 X_0.

2.2.5 Time-of-flight counter (TOF)

TOF consists of 96 plastic scintillator with dimensions of 4.2×10.8×466 cm^3 [31]. These counters are placed inside of a solenoid coil at the radius of 166 cm and cover the range of $|\cos\theta| \geq 0.81$. There are 0.3 cm gaps between two adjacent counters. These gaps cause the inefficiency of about 3%. Each end of the scintillator is viewed by a photo-multiplier tube (PMT) through a 145 cm long acrylic light guide. The time resolution is estimated to be about 200 nsec by using Bhabha and $\mu^+\mu^-$ events.

By combining the time and the momentum measured by TOF and CDC, respectively, the π/K/P separation for $p < 1$ GeV/c is possible. TOF is also used for event trigger.

2.2.6 Magnet system

The magnet system consists of a superconducting solenoid, a flux return yoke, a helium refrigerator and a high current power supply. The superconducting solenoidal coil has its dimensions of 177 cm in radius and 527 cm in length. It provides a uniform magnetic field of 7.5 k-Gauss in the beam direction. Its superconducting material is Nb-Ti/Cu. The excitation current is 3980 A at 7.5 k-Gauss. The material thickness in the radial direction is made exceedingly thin, 0.52 X_0.

The iron return yoke supports the magnetic force of about 230 ton with a maximum elastic deformation of 0.04 cm. The cryogenic system keeps the temperature of the solenoid below 4.5 K. The stored energy is estimated to be 11.7 MJ.

The magnetic field in a volume of 3.2 m diameter by 4 m length was measured by using a nuclear-magnetic resonance (NMR) probe and the hall probes for the three dimensional components with the accuracy of the order of 10^{-4}. The uniform field of 7.5 k-Gauss was obtained in the entire CDC region within a standard deviation of 0.3 % [32].

2.2.7 Barrel lead-glass calorimeter (LG)

The roll of the lead-glass calorimeter (LG) is to detect and measure the energy of electromagnetic particles such as electrons and photons. It is located between the solenoid coil and iron return yoke with the radial range of 197−230 cm and length of 615 cm [33]. It covers a range of angle $|\cos\theta| \leq 0.80$. LG calorimeter consists of 5160 lead-glass Čherenkov counter modules and is segmented into 120 blocks in the ϕ-direction and 43 blocks in the z-direction. A LG module is made of DF6 whose main components are PbO (70.9 %) and SiO_2 (27.3 %), and has properties such as the radiation length of 1.69 cm, the critical energy of 12.6 MeV and the refractive index of 1.805. The typical size is 12.0×11.6 cm^2 in cross-section and 30 cm in length,

corresponding to 18.0 X_0. The schematic cut view of a LG module is shown in Fig. 2.8. A 3-inch PMT surrounded by a μ-metal magnetic shield is attached to each LG module together with a plastic light guide of 5 cm in length. At the central part of LG calorimeter, the box- and grid-type of PMTs are used, while at the both end parts where the leakage field is 20 to 30 Gauss, mesh-type are used. High voltage ranging from -1.5 to -2.0 kV is applied for PMTs during data taking. In order to trace the gain fluctuation of the PMTs, a monitoring system of a Xe flash tube with an optical fiber bundle is used.

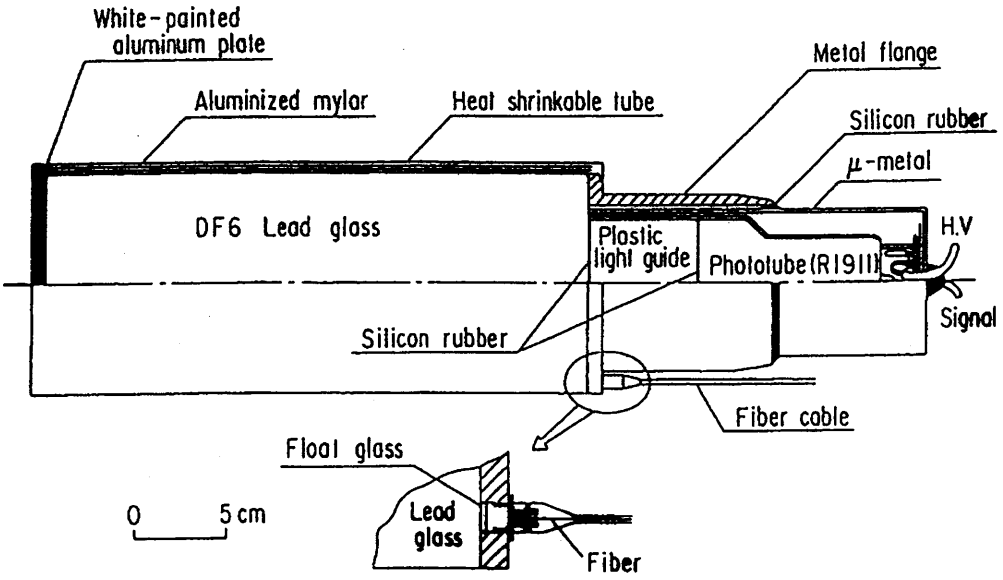

Figure 2.8: Assembly of a lead-glass module.

LG blocks are pointed to the interaction region to minimize multi-hit probability of a particle. LG is divided into seven sections in the z-direction, and the lead-glass blocks are set parallel within each section as shown in Fig. 2.9. In this configuration, LG blocks are tilted by 0° to 14° with respect to the line which point to the interaction point. In the x-y plane, all LG blocks are tilted by 3° with respect to the radial line. This semi-tower geometry prevents a particle from escaping through 0.15 cm gaps between blocks.

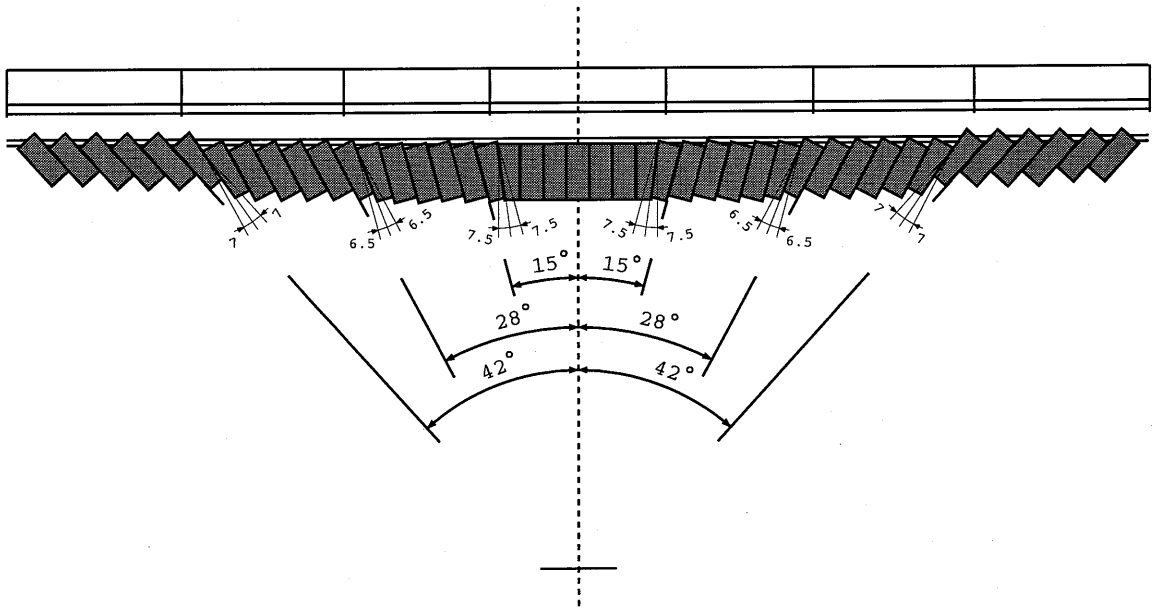

Figure 2.9: Schematic view of LG

Energies are measured with Čherenkov lights ($\sim 10^3$ photoelectrons for a 1 GeV electron) which are radiated by charged particles in electromagnetic showers. Such a high energy shower develops by successive bremsstrahlung and electron-positron pair creation by photon until their energies reach the critical energy. Below the critical energy, ionization by collision processes dominates. So the total amount of the light yield is proportional to the energy deposit in LG blocks. The relation between the energy and the light yield was calibrated by using the electron beam from the internal target beam line (IT4) at TRISTAN-AR [34].

2.2.8 Endcap liquid argon calorimeter (LA)

LA is a sampling calorimeter for measuring the energies of electromagnetic shower induced by electron and photon in the forward and backward region. A pair of liquid argon calorimeter are installed between CDC and endcaps of the return yoke. Each one covers an angular range of $0.79 \geq |\cos\theta| \geq 0.99$ as shown in fig 2.10. Each calorimeter consists of 480 tower structure modules which look at the point 80 cm away from the interaction point on the beam axis to prevent a particle from escaping through gaps of 3.0 mm. Fig. 2.10 shows a view of LA. Each tower module consists of 71 calcium-lead plates of 0.15 cm thick which corresponds to 20.3 X_0. The whole calorimeters are filled with liquid argon of 86 K. Lead plates of each tower are electrically segmented into four groups, so each side of the calorimeter has 1920 channels of signal read-out [37].

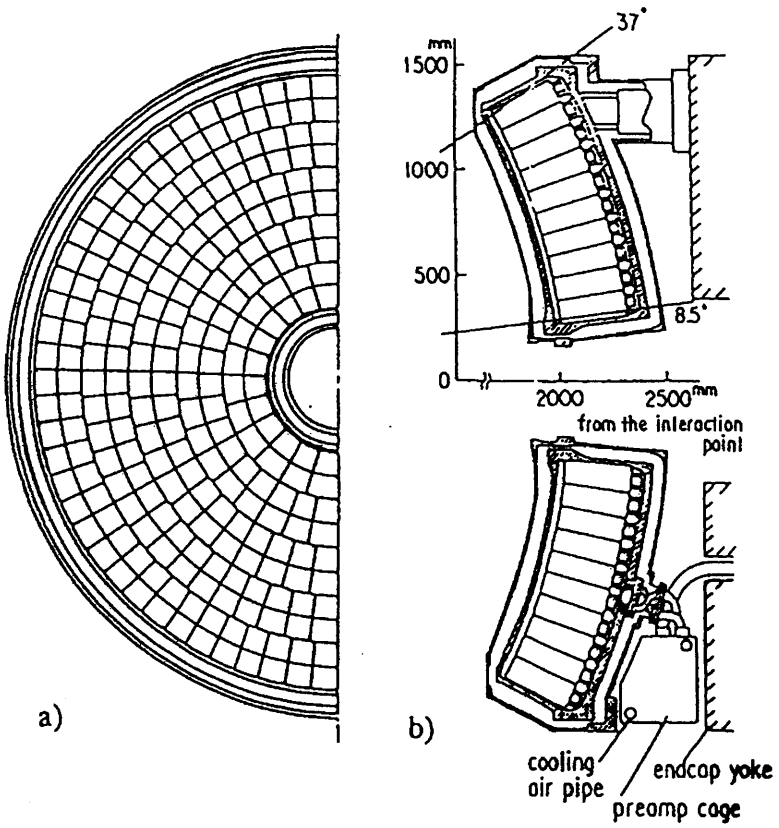

Figure 2.10: Schematic view of LA

2.2.9 Muon chamber system

The muon chamber system covers the large outermost area of VENUS to detect muons [38, 39]. It consists of two main parts: the barrel part and the forward-backward part. Both parts consist of four layered array of extruded aluminum modules, each with 8 cells of drift tubes. A module consists of two layers of four cells staggered by a half cell as shown in Fig. 2.11.

Each cell has cross-section of 5×7 cm^2 with the wall thickness of 0.25 cm on average. Lengths of the modules are 760 cm for the barrel part, and vary from 245 cm to 505 cm depending on the location for the forward-backward part. The sense wire of 70 μm in diameter made of gold-plated tungsten with 3 % rhenium is stretched at the center of each cell with a tension of 400 gW. The tubes are filled with P-10 gas (Ar:CH_4 = 90:10). High voltage of 2.7 kV is applied to each sense wire and the tubes are operated in a proportional mode.

In the barrel part, inner three layers of the modules, interleaved with 20 cm thick iron filters, measure the x and y positions of the penetrating particle. The outermost layer of module, which is located just outside of the third layer without any iron filters, measures the z-position

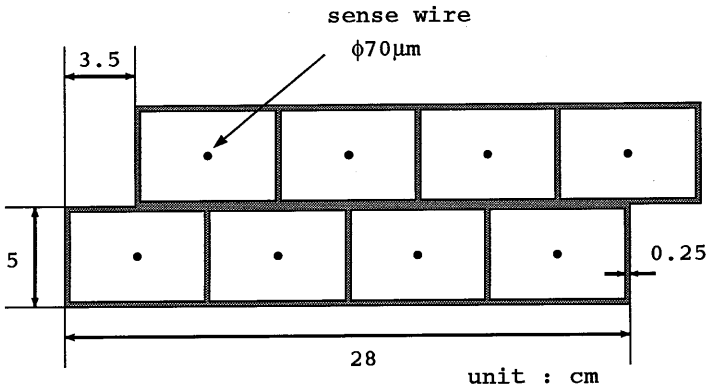

Figure 2.11: A module of muon chamber.

of the track. In this region, the main absorbing material along the particle path emitted from the interaction point consists of the lead glass calorimeter, their support rings made of 17.5 cm thick iron and 10.0 cm thick aluminum, the return yoke made of 30.0 cm thick iron and two muon filters, each comprising 20.0 cm thick iron. Thickness of each muon filter is chosen to be about 1 nuclear absorption length. Distances between the return yoke and the first muon filter and between 2 muon filters are chosen to minimize possible decays of surviving $\pi^{\pm}$ and $K^{\pm}$. Muons should penetrate at least 5.3 absorption length of material up to the outside of the VENUS.

2.3 Event trigger system

The trigger system is composed of two levels; a first-level trigger designed to work between beam crossings and a second-level trigger which is a slower software track trigger.

2.3.1 First-level trigger

The trigger decision must be made within a collision interval of 5 μsec, so the above system consists of hardware logics only. The first-level trigger is issued when the beam-crossing signal and the signal issued by trigger generation circuits coincide. Inputs to the trigger decision module are track patterns reconstructed by CDC and analog-sum signals from calorimeters as shown in Fig. 2.12. Details of these are as follows.

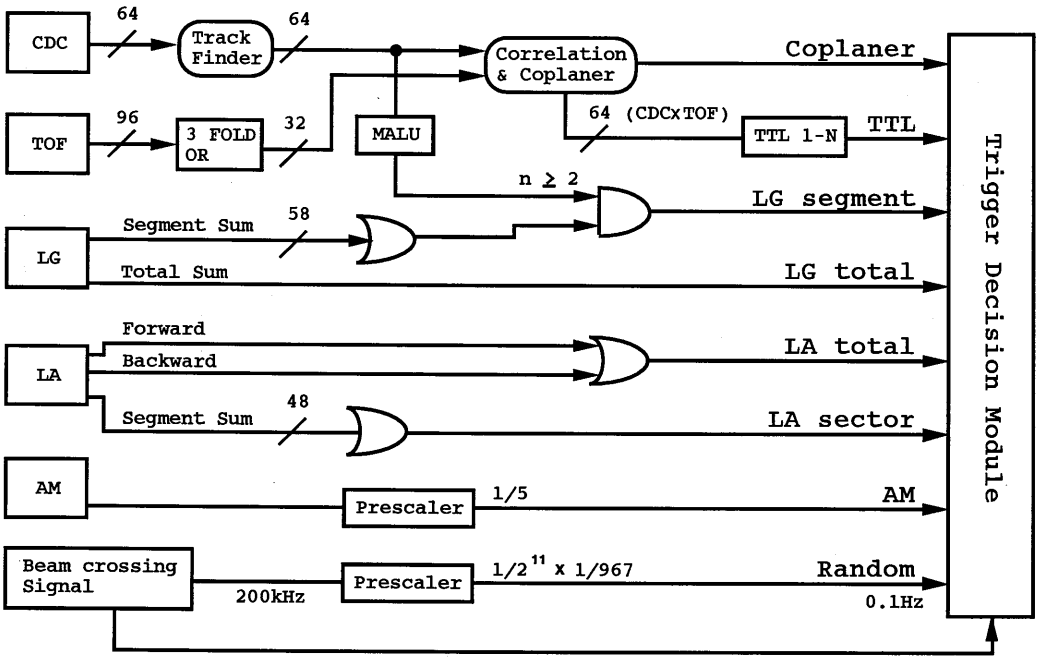

Figure 2.12: Trigger logic

Track pattern recognition with track-finder module in Fig. 2.12 is as follows. The axial-layers cells of CDC are grouped to 64 trigger-cells in each superlayer, divided in azimuth. A track-finder module recognizes tracks by comparing the trigger-cell hit pattern from inner 7 superlayers with a pre-loaded look-up table [40]. The pattern of the look-up table is so defined that the track finders should have nearly the full efficiency for tracks which have high transverse momentum p_{xy} with respect to the z axis as shown in Fig. 2.13.

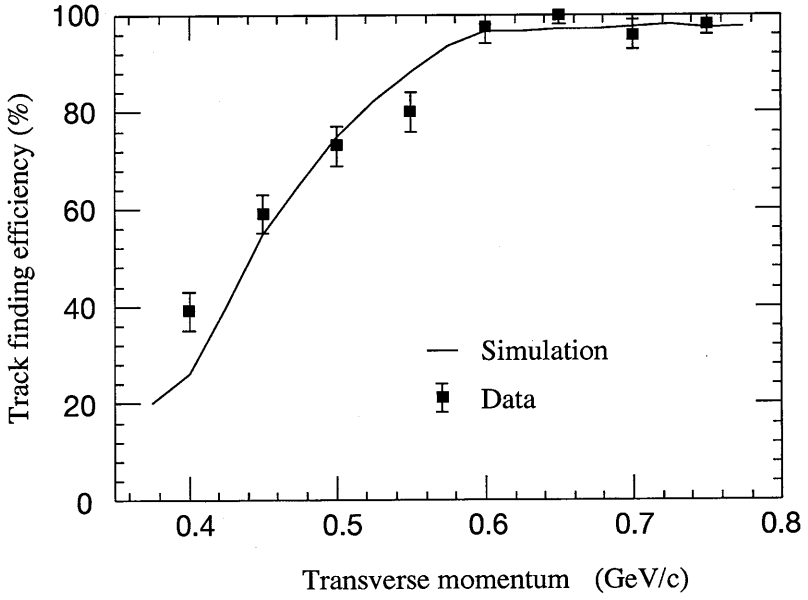

Figure 2.13: Trigger efficiency of the track finder

For event trigger, LG calorimeter is divided into 58 segments *i.e.* 7 segments in the z-direction and 8 or 10 segments in the ϕ direction. The analog-sum signal of each segment is used for LG segment trigger. Also all 58 segment-sum signals are sent to an analog-sum circuit and then the analog-sum signal is used for LG total trigger. Similar to LG, each of LA calorimeter is divided into 12 sectors in azimuth and each sector is further divided into inner ($0.91 \geq |\cos\theta| \geq 0.99$) and outer ($0.79 \geq |\cos\theta| \geq 0.91$) part. Thus analog-sum signals from the 48 sectors in both sides are used to form LA sector trigger. Analog-sum signals of 48 sectors are sent to an analog-sum circuit and then the analog-sum signal is used for LA total trigger.

The first-level trigger based on the above information are as follows.

- **Coplanar trigger**

  For the coplanar trigger condition, the acoplanarity angle between two tracks must be less than 10 °. The acoplanarity angle is defined as the supplementary angle in the x-y plane between the two tracks and expressed as

$$\theta_{\rm acop} = \cos^{-1}\left(\frac{-\overrightarrow{p_{t1}}\cdot\overrightarrow{p_{t2}}}{|\overrightarrow{p_{t1}}||\overrightarrow{p_{t2}}|}\right), \tag{2.9}$$

  where $\overrightarrow{p_{t1}}$ and $\overrightarrow{p_{t2}}$ are the momentum vectors projected onto the x-y plane.

- **Two-Track-Limited trigger (TTL)**

  Condition of the TTL trigger (the acoplanarity angle cut) is looser than that of the coplanar trigger and is extended to 25°.

- **LG segment sum**
  At least 2 tracks are recognized by "track finder" and at lease one of LG segments has an energy deposit larger then 0.7 GeV.

- **LG total sum**
  A total energy deposit in LG is lager than 3 GeV.

- **LA sector sum**
  At least one of LA sectors has an energy deposit larger then 2 GeV.

- **LA total sum**
  At least one side of LA has a total energy deposit lager than 4 GeV.

- **Active mask trigger**
  Total energy deposit larger than 10 GeV in back-to-back configuration[9].

- **Random trigger**
  Random trigger is made by beam-crossing signal. Beam-crossing signal is scaled down by a factor of 2 $\times 10^6$. This trigger occurs every 10 sec.

2.3.2 Second-level trigger

A second-level trigger uses a slower software. At the first-level, we find tracks in CDC by making use of the track finder. Its information is sent to another electronic circuit which makes a ϕ correlation by combining the information from TOF counters. Flexibility and high granularity in the first level trigger require an increased number of wires and a complex circuit. However, the logic in the ϕ correlation is limited by hardware restriction. Indeed, the TTL triggered events contain large backgrounds which originate from the interaction of the beam particles with the beam pipe. When a event is taken by the only TTL trigger, the second-level trigger is applied to the event. A micro-processor 68K20FPI carries out a refined track finding by combining CDC and TOF hit information in the ϕ regions where tracks have been found at the first-level trigger. The second-level trigger can improve the vertex resolution, and thus reduce the background events. It reduces the number of TTL triggered events to about 50 %. The total trigger rate is typically 5$\sim$7 Hz and dead time of it is 5 % though it strongly depends on the beam condition.

[9]The back-to-back configuration means that the signals are induced at both symmetric positions of a pair of active mask.

2.4 Data Acquisition (DA) System

The data acquisition system [41] has a tree-like structure as shown in Fig. 2.14. For the front-end electronics, several data buses such as CAMAC[10], TKO[11], and FASTBUS[12] are used. These buses handle about 30000 electronic readout channels in total. All digitized data from the front-end electronics of the detector components are transferred to FASTBUS memory buffers and collected by a 68K20FPI module on FASTBUS whenever an event trigger occurs. And then all data in 68K20FPI are read by an on-line computer VAX6320.

The collected data are sent to a main frame computer FACOM M1800 via optical fibers and then stored in an automatic loading cartridge tape library.

Representation	module name
68K20FPI	FASTBUS Processor Interface with 68020 micro-processor
DRB	general purpose bus of DEC
TDR	Trigger Decision Module
TFC	Track Finder for CDC
IOR	Input/Output Register
MUL	Majority Module
SSI	Simplex Segment interconnect
AT	Active Terminator of cable segment
T	Terminator of cable segment
FCI	FASTBUS–CAMAC Interface
MP	Memory Partner
CH	Controller Head
SCH	Super Control Head
MRB	Multi-Record Buffer
SMI	Segment Manager Interface
TAC	Time-to-Amplitude Converter
SADC	Scanning ADC
FADC	Flush ADC
CAT	Calibration & Trigger Module
STOS	Streamer Tube Operating System

Table 2.3: Lists of modules in the DA system

[10]CAMAC is an international standard of modularized electronics as defined by the ESONE Committee of the JRC, Ispra.

[11]TKO is a system of front-end electronics developed at KEK [44].

[12]The standard modular high-speed data acquisition and control system defined by ANSI/IEEE std 960-1986

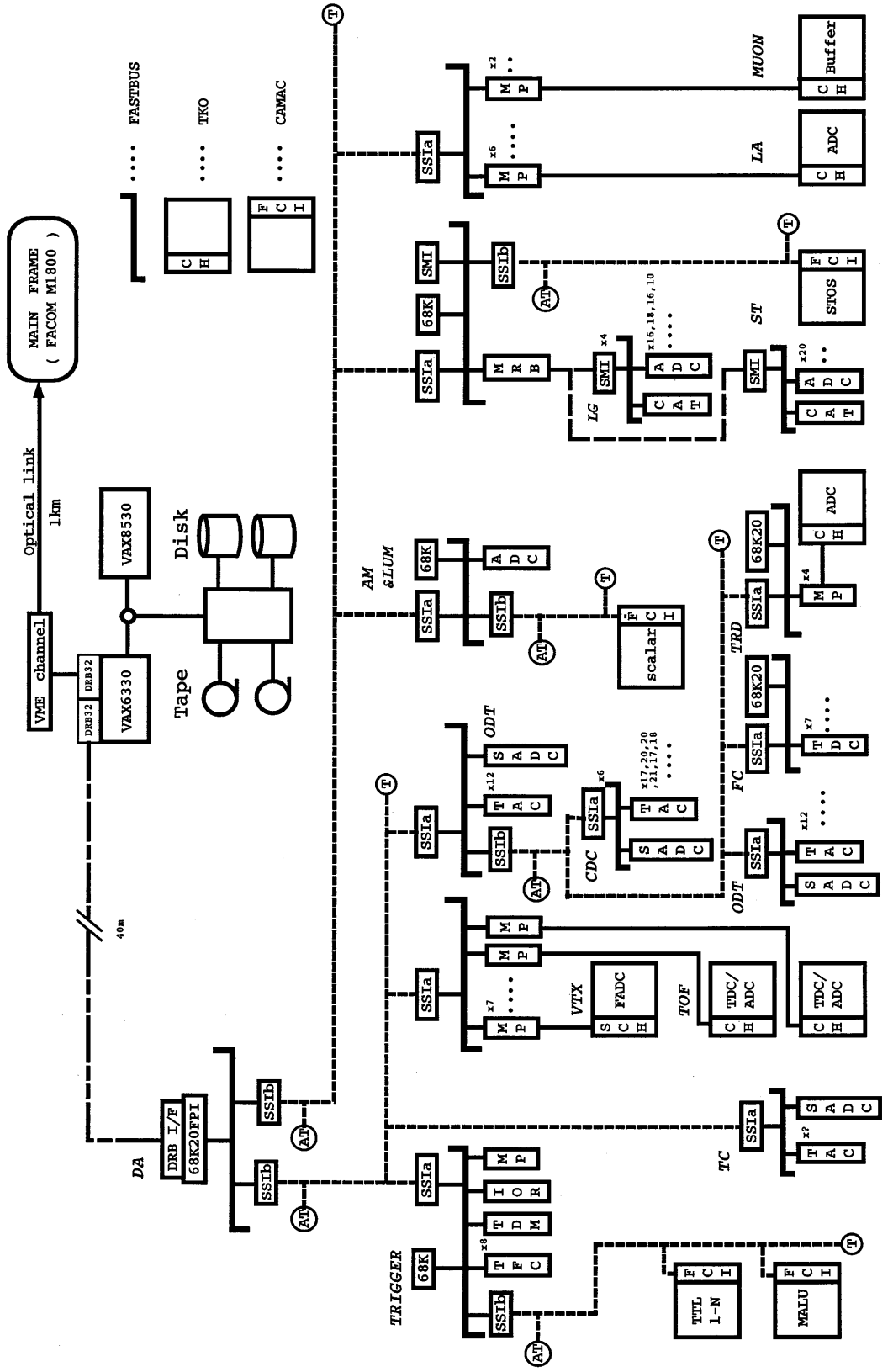

Figure 2.14: Data acquisition system of VENUS

Chapter 3

Event reconstruction and Data reduction

Data taken by the DA system are composed of digitized quantities from ADC, TDC and etc. So they are called "Raw data" and need to be reconstructed as tracks and clusters before physics analysis. Then the reconstructed events are classified into several categories, *e.g.* hadronic events, low multiplicity events and Bhabha events, depending on physics analysis. In this chapter, the method of event reconstruction and data reduction are presented.

3.1 Event reconstruction

Event reconstruction is a process to convert raw data to physical quantities such as tracks and clusters.

3.1.1 Track reconstruction in CDC

The measurement of momentum and charge of a charged particle is performed by reconstructing its trajectory in CDC. The track reconstruction in CDC is carried out by using the pattern recognition program named PERPR [45, 47].

Since a magnetic field of 7.5 kG is applied along the z-axis, the charged particle spirals in the 3 dimensional space and thus its trajectory makes a circle in the x-y plane. The projected momentum in the x-y plane p_{xy} (GeV/c) can be obtained from the relation

$$p_{xy} = 3.0 \times 10^{-4} \cdot B \cdot \rho \tag{3.1}$$

where B is the magnetic flux density in kG, and ρ is the radius of curvature in cm. In the PERPR program, track reconstruction in the x-y plane is done by using axial wire informations at first. If we succeed the above reconstruction, we try to reconstruct a track in the three dimension by using slant wire informations.

Reconstruction in the x-y plane.

The track reconstruction in the x-y plane is performed as follows,

1. An "initial road" is searched at the outermost two layers of CDC. If hits are found in both layers, the 'road' of a track is defined. Thus, four possible combinations of a track due to left-right ambiguity are taken into account as shown in Fig. 3.1.

2. Then candidate hits along the "road" are searched. The left-right ambiguity is solved by fitting with axial wire positions. To find a most likely track, the least χ^2 fit is performed by eliminating hits of poor quality. If χ^2 exceeds 5.0, the track is abandoned.

3. The curvature of the track is calculated from the above formula and some relevant quantities such as charge and p_{xy} are calculated.

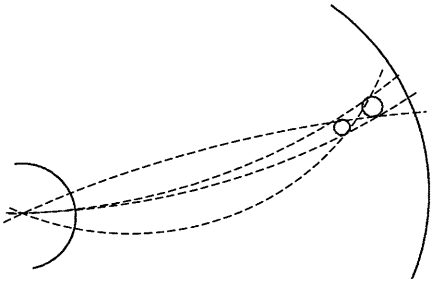

(a). Define initial road at the outermost two layers

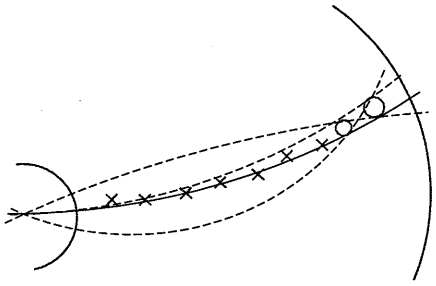

(b), Search hit cells along the load

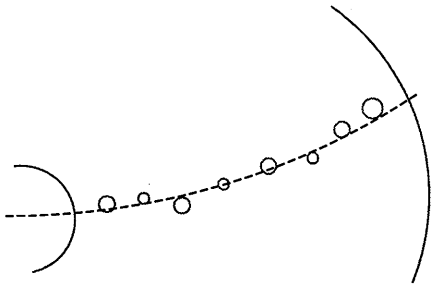

(c). Obtain the most probable trajectory

Figure 3.1: Track reconstruction procedure: (a) to determine the initial road, (b) to search for hit cells along the road and then make a trajectory fit, and (c) to obtain the most probable trajectory

Reconstruction in the z-s plane.

Slant-layer hits are used in association with axial-layer hits to determine a three-dimensional trajectory. Since slant wires are inclined by 3.5 degrees with respect to axial wires, the z coordinate of the track can be given by

$$z = \frac{\ell}{2} - \frac{d}{\tan\alpha}, \tag{3.2}$$

where d is the distance between the axial track and the stereo hit, α is the slant angle (3.5°) and ℓ is the wire length of the slant wire projected onto the beam axis.

The overall trajectory can be expressed in a linear form as

$$z = \frac{dz}{ds}s + Z_{\min} \tag{3.3}$$

where $Z_{\min}$ is the distance at the closest approach in the x-y plane, s is the length of arc element and dz/ds is the gradient. The track finding algorithm is similar to that for the x-y plane. These configuration of CDC track is illustrated in Fig. 3.2.

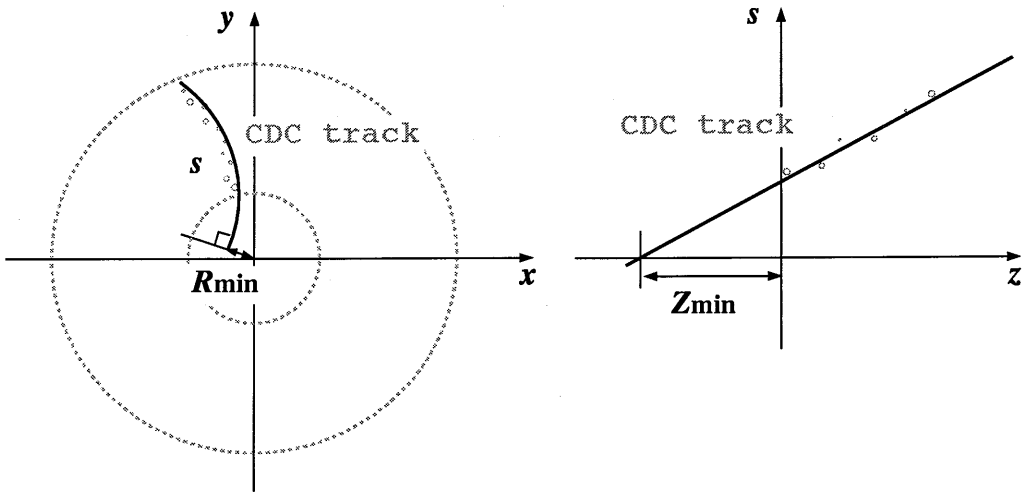

Figure 3.2: Definition of track parameters: (a) $R_{\min}$ and (b) $Z_{\min}$. Both figures show in the case of negative values.

Here the distance of the closest approach to the interaction point in the x-y plane is defined as $R_{\min}$. We define $R_{\min}$ to be positive (negative) if the interaction point lies inside (outside) the circle of a track.

Tracking performance.

For charged tracks in the range of $|\cos\theta| \leq 0.75$ where they are able to pass through all axial and slant layers of CDC, tracking performance has been evaluated using Bhabha scattering events. The vertex resolutions for high-p_{xy} tracks have been found to be

$$\sigma_{\text{vertex}}(xy) \simeq 460 \quad \mu\text{m}$$
$$\sigma_{\text{vertex}}(z) \simeq 0.67 \quad \text{cm}$$

In the same way, the angular resolutions in the azimuthal and polar angles have been estimated to be

$$\sigma_\theta = 8\sin^2\theta \quad \text{mrad}$$
$$\sigma_\phi = 1.3 \quad \text{mrad}$$

The measurement of the polar angle is much less accurate than that for the azimuthal angle. The momentum resolution is found to be

$$\frac{\sigma_p}{p} = \sqrt{(0.013)^2 + (0.008 \times p_{xy})^2} \tag{3.4}$$

with p and p_{xy} in GeV/c in a magnetic field of 7.5 kGauss using cosmic ray and Bhabha data samples. The first term in Eq. (3.4) is contribution from multiple coulomb scattering by materials in the tracking volume, *i.e.* the chamber gas and the wires. The second term is due to measurement error in the drift distance. The reconstruction efficiency for the high-p_{xy} charged tracks in the range of $|\cos\theta| \leq 0.75$ has been studied by collinear Bhabha events and found to be better than 99.9 % in the x-y plane.

3.1.2 LG Clustering

Since an electromagnetic shower generally spreads over several LG blocks, the shower energy and its incident position should be determined by an appropriate clustering method.

Clustering method.

The intrinsic limitations in spatial resolution are firstly given by detector granularity, and secondly given by lateral spread of the electromagnetic shower which is mainly caused by multiple scattering of low-energy electrons that no longer radiate any photons and drift away from the shower center axis. A proper scaling variable for the lateral shower distribution is the *Molière radius* [1] R_M which corresponds to 2.8 cm for lead-glass (DF6).

Accordingly, several blocks share the shower energy permitting the measurement of the shower center position. The clustering and the measurement of the shower center are performed as follows:

1. Starting from a module which contains the highest energy, neighboring modules are examined whether they belong to the same cluster or not. Thus, a "connected region" is formed by searching all neighboring modules adjacent in the ϕ or θ direction.

2. The shower energy is calculated by summing up the energies in the same cluster.

3. The incident position of the showering particle is determined by the energy weighted average of the position of LG blocks in a cluster as follows:

$$x_{\text{cluster}} = \frac{\sum E^{\alpha} x}{\sum E^{\alpha}}, \tag{3.5}$$

where x is the central ϕ- or θ-position of a block $\alpha = 0.34$ which was optimized by a shower simulation calculation using EGS4 program [48].

Performance of LG cluster reconstruction.

The energy resolution for an electron evaluated using $e^+e^- \rightarrow e^+e^-, e^+e^-\gamma$ and $e^+e^-e^+e^-$ events is given as

$$\frac{\sigma_E}{E} = 0.025 + \frac{0.07}{\sqrt{E}}, \tag{3.6}$$

where E is in GeV. The first term accounts for the effects such as instrumental noise, shower leakage and inter-calibration error, whereas the second term come from the statistical fluctuation of the number of photoelectrons. The angular resolution of the calorimeter can be studied by comparing the measured shower center position with CDC track extrapolated to LG module surface for large angle Bhabha scattering. The angular resolution has been measured to be

$$\begin{aligned} \sigma_{\theta}^{LG} &= 4.0 \text{ mrad}, \\ \sigma_{\phi}^{LG} &= 5.2 \text{ mrad}. \end{aligned} \tag{3.7}$$

[1] Molière radius is given by $R_M = 21 X_0/E_c$, where E_c is the critical energy for the detector material in MeV.

3.1.3 LA Clustering

Clustering method.

The cluster finding algorithm for LA is similar to that for LG except that only adjacent towers are included in the search and not for towers in diagonal direction. The center of the cluster is measured by a shower-profile method. It is known that the lateral shower spread $E(x)$ of the electromagnetic shower can be expressed by the following double exponential form [49]:

$$E(x) \cong E_1 \exp(-\frac{|x|}{\lambda_1}) + E_2 \exp(-\frac{|x|}{\lambda_2}), \tag{3.8}$$

where x is the lateral distance from the shower center, and λ_1 and λ_2 represent the shower extension. The first term is the central component which describes the multiple coulomb scattering of the electrons and positrons in the material. The second term is the peripheral component which arises via isotropic propagation of photons. In principle, the shower center can be obtained by solving the above equation but this is generally difficult. To make the problem easier, only one exponential term has been considered. The slope parameter λ has been taken as a function of lateral energy so that

$$\lambda = g(y), \tag{3.9}$$

with

$$y = \ln \frac{1}{2}(\frac{E_i}{E_{i+1}} + 1), \tag{3.10}$$

where E_i represents the energy deposit in the i-th tower. The function $g(y)$ has been parameterized for high-energy electromagnetic showers by using EGS4.

Performance of LA cluster reconstruction.

The energy resolution of LA calorimeter has been studied using radiative Bhabha scattering events, and found to be

$$\frac{\sigma_E}{E} = 0.016 + \frac{0.102}{\sqrt{E}}, \tag{3.11}$$

where E is in GeV. Similar to LG, the first and second term are due to intrinsic noise and statistical fluctuation, respectively. The normalization factor for the energy calibration is given by measuring the energies of Bhabha events. The angular resolution of the calorimeter has been studied by the same method as that used for LG. It is obtained to be

$$\sigma_\theta^{LA} = 2.9 \quad \text{mrad}, \tag{3.12}$$

$$\sigma_\phi^{LA} = \frac{2.6}{\sin\theta} \quad \text{mrad}, \tag{3.13}$$

where errors are determined by fitting the result.

3.1.4 The transition radiation energy clustering in TRD

We measure the transition radiation energy in TRD in order to separate electrons from pions. Energy clustering in TRD is necessary to calculate the transition radiation energy for each charged particle. The TRD detector has four modules of a pair of radiator and X-ray chamber as mentioned in Chap. 2.2.4. We can measure the transition radiation energy in each module independently.

Energy clustering in TRD.

The transition radiation energy $E_{\rm TRD}$ for a CDC track is calculated as follows.

1. We extrapolate an CDC track to TRD and then search for wire hits.

2. To calculate the transition radiation energy at a module, the pulse height of the hit wires (i) are summed.

$$E_{\rm TRD} = \sum_i ADC_i \cdot c_i(z,\phi) \cdot g(t) \cdot \frac{d}{L} \tag{3.14}$$

where ADC_i is the pulse height given by the ADC modules and c_i is the gain correction factor as a function of wire position (z and ϕ). Furthermore, $g(t)$ is a gain factor at a time of t. The gain and its correction factors are described bellow. The variables d and L are the thickness of the chamber (2cm) and the path length of the track, respectively. The pulse heights are thus normalized to those for a normal incident track. If a wire is hit by more than one track, the accumulated pulse height is divided among them in proportion to the corresponding gain factors $c_i(z,\phi) \cdot g(t)$ and path length L.

Gain correction.

Gain variation of X-ray chambers is due to two different sources. The first one may be called "local effects" and is time independent. The variation of wire displacement due to gravitational sag and deformation of the cathode surface belong to this category. These effects are supposed to be stable in time, but cause a local difference in gain. It is calibrated by measuring the mono-chromatic X-ray from ^{109}Cd (E_γ = 22 KeV) [50].

The second one may be called "global effects" and is time dependent. The variation of atmospheric pressure, temperature and gas composition belong to this category. So there is a gain stabilization system which consists of a gas gain monitor and a control system of supplied high voltage. The gas gain monitor is composed of ^{55}Fe X-ray source and X-ray chamber itself. We continually monitor and record the peak values of the ^{55}Fe X-ray measured by X-ray chambers during the data taking. In order to correct this global effects, we made a offline database of gain variation as a function of time period (t).

3.2 Data reduction

To study the forward-backward asymmetry of events which contain c or b quarks, it is necessary to reduce a lot of physical backgrounds such as two-photon process ($\gamma\gamma \rightarrow$ hadrons) and τ pair production ($e^+e^- \rightarrow \tau^+\tau^-$) from all of obtained events.

3.2.1 Hadronic event selection

Hadronic events produced via a single photon or Z^0 boson ($e^+e^- \rightarrow \gamma/Z^0 \rightarrow q\bar{q} \rightarrow$ hadrons) are characterized by the a large charged multiplicity $N_{\rm good}$, large visible energy $E_{\rm vis}$, small balance of momentum along the beam direction $P_{\rm bal}$ and large invariant mass of jets $M_{\rm jet}$. We select hadronic events by the requirements as follows.

1. $E_{\rm cal} > 5$ **GeV**
   $E_{\rm cal}$ is defined as the total energy deposit in LG and LA calorimeter within $|\cos\theta| < 0.89$. This cut is effective to reduce two-photon events. Two-photon process is collision of two virtual photons emitted by beam particles.

2. $N_{\rm good} \geq 5$
   $N_{\rm good}$ is defined as the number of good tracks, where good track means well reconstructed track in CDC which satisfies the following requirements,

$$\begin{array}{lcl} N_{\rm axial\ wire\ hits} & \geq & 8 \\ N_{\rm slant\ wire\ hits} & \geq & 4 \\ |R_{\rm min}| & < & 2\ {\rm cm} \\ |Z_{\rm min}| & < & 20\ {\rm cm} \\ |\cos\theta| & < & 0.85 \\ p_{xy} & \geq & 0.2\ {\rm GeV}/c \end{array}$$

   where p_{xy} is the amount of a projected momenta into the x-y plane. This cut is effective to reduce lepton pair production and two-photon events.

3. $E_{\rm vis} > E_{\rm beam}$
   $E_{\rm vis}$ means total visible energy and is defined as a sum of absolute momentum of good tracks and total energy deposit in LG and LA calorimeter. This cut is also effective to reduce two-photon backgrounds.

4. $P_{\rm bal} \leq 0.4$
   P_{bal} means momentum and energy balance along the beam direction and is defined as below,

$$P_{\rm bal} = \frac{\sum p_z + \sum E_z}{E_{\rm vis}} \tag{3.15}$$

where p_z and E_z are z component of momenta of a good track and a cluster energy, respectively. This cut is effective to reduce two-photon backgrounds.

5. $M_{\mathrm{jet}} > 3$ **GeV**$/c^2$

   We define a pair of jet masses M_{jet} as an invariant mass of particles which belongs to each hemisphere divided by a plane perpendicular to the thrust axis. We require that at least one of them should be larger then 3 GeV$/c^2$. This cut is effective to reduce tau pair events.

Figure 3.3 shows the distributions of each cut variables after all of the above selections, where plot and histogram indicate the experimental and Monte Carlo data, respectively.

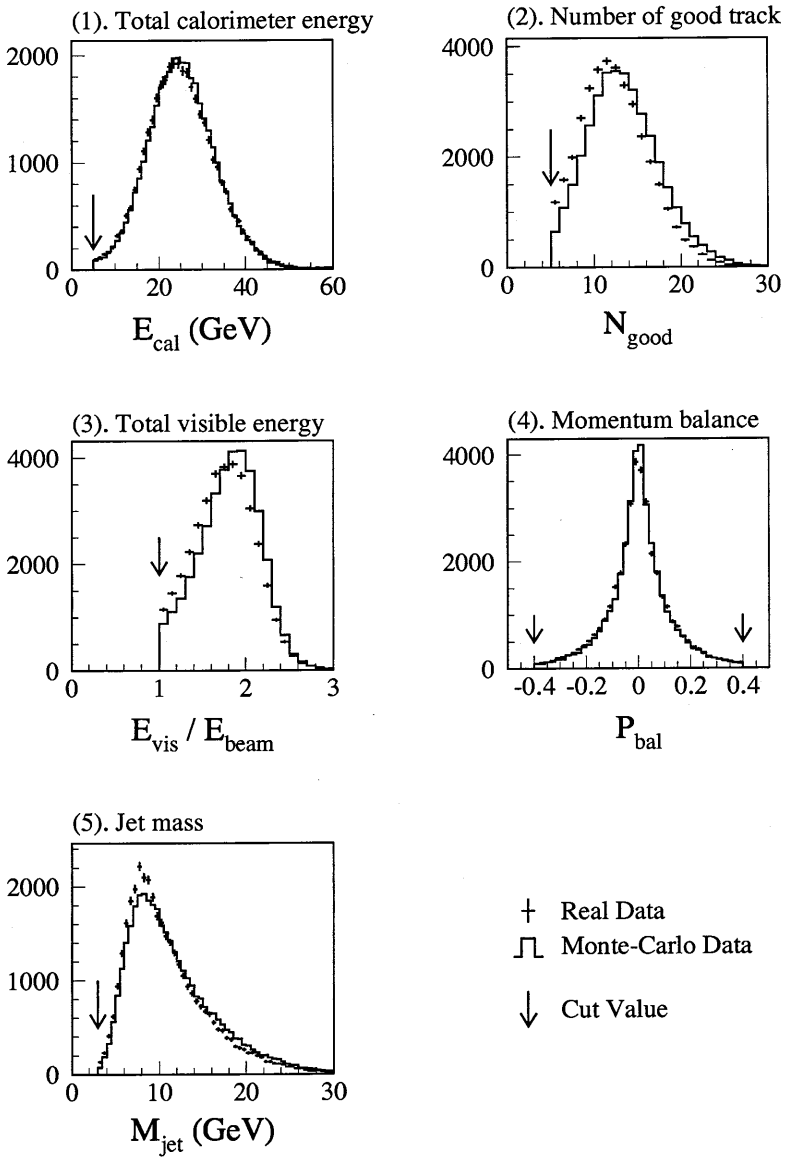

Figure 3.3: Distributions of the cut variable after hadronic event selection

3.2.2 Rejection of hadronic events with hard initial-state photon radiation

If one or more photons are emitted in the initial-state, the effective center-of-mass energy of the subsequent e^+e^- collision, $\sqrt{s'}$, is lowered from the nominal center-of-mass energy $\sqrt{s} = 58$ GeV as shown in Fig. 3.4a. When we study the quark pair production, only events of which $\sqrt{s'} \simeq \sqrt{s}$ is interesting for us. Therefore we reject events in which photons in the initial-state radiation have a large energy. On the other hand, photons in the final-state radiation don't lower the energy s' and associate with the corresponding quark jets as shown in Fig. 3.4b. To reject only events with initial-state photon radiation, we also require that the photons isolate from the jets.

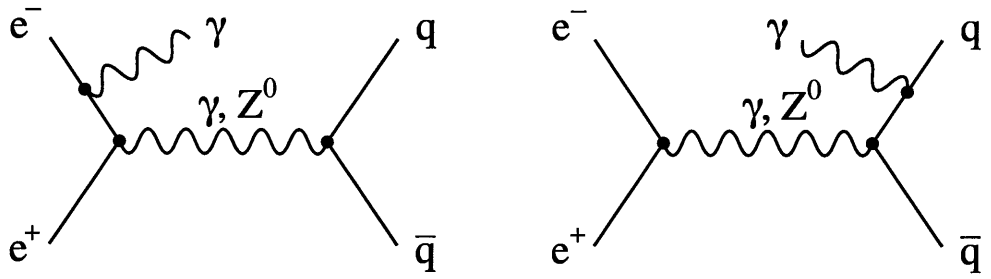

Figure 3.4: Feynmann diagram of quark pair production (a) with initial- state photon radiation, (b) with final-state photon radiation.

Events which fulfill any of the following requirements are rejected as hadronic events with hard initial-state photon radiation.

1. There exists a LG or LA cluster with $E_{\text{cluster}} > 0.75 E_{\text{beam}}$.
2. When a LG or LA cluster with $E_{\text{cluster}} > 0.5 E_{\text{beam}}$ exists, we require that the number of tracks in the 30° cone around an axis which connects the center-of-gravity of the cluster to the interaction point is less than two as a requirement of photon isolation.
3. No track exists in either of the hemispheres.

We have studied effects of these rejection by using Monte Carlo simulation. Figure 3.5 shows the spectra of the scaled effective center-of-mass energy (s'/s), where dashed line indicates all of hadronic events, solid line indicates events just before the rejection and shaded histogram indicates those after the rejection. Low s' events ($s'/s < 0.5$) are obviously reduced.

Figure 3.6 shows a typical hadronic event with hard initial-state photon radiation. In this event, an initial-state photon is clearly isolated and the other hadrons are collimated to the opposite direction against the photon.

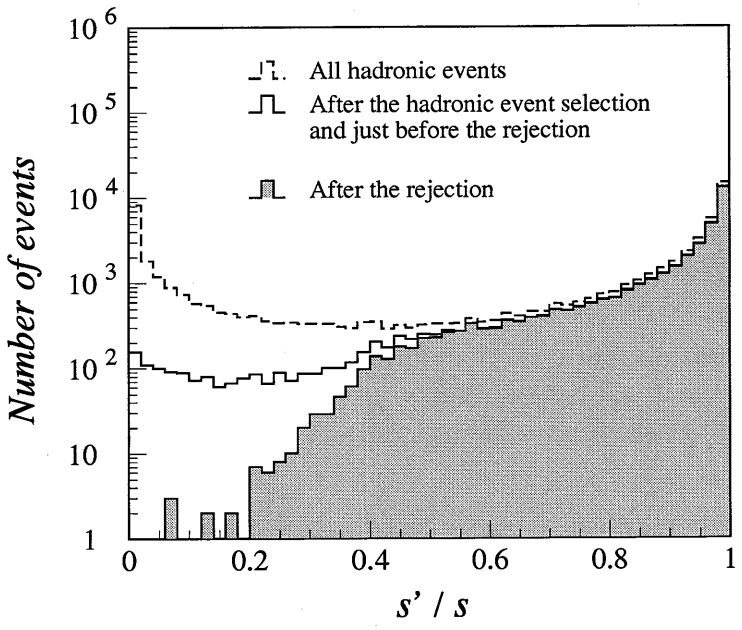

Figure 3.5: Effective center-of-mass energy (s'/s) spectra of hadronic events. Solid and shaded histograms indicate events before and after the rejection, respectively. All of the hadronic events generated initially are also indicated by dashed histogram.

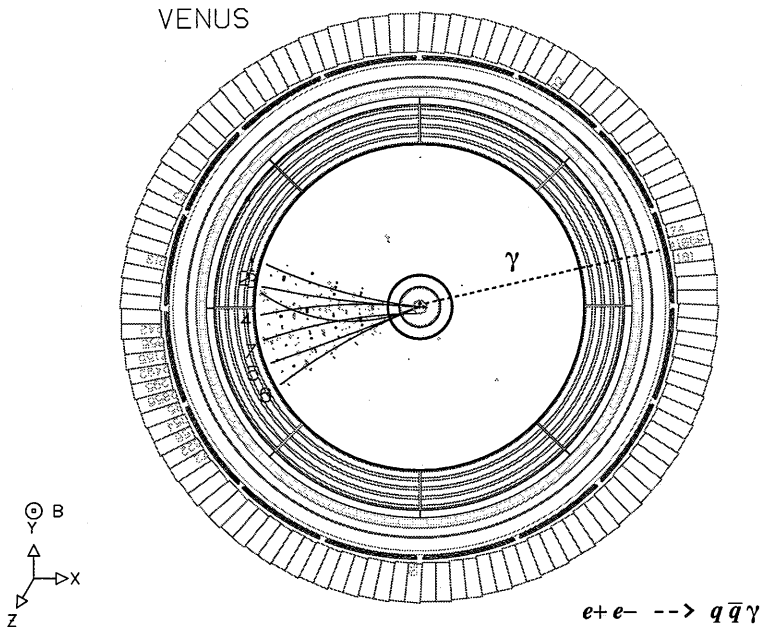

Figure 3.6: A hadronic event with hard initial-state photon radiation

3.2.3 Rejection of radiative Bhabha events and electron inclusive events in two-photon process

After the above selections, some backgrounds which include electrons still remain. Two such examples are radiative Bhabha events and electron inclusive reaction in two-photon process as shown in Fig. 3.7.

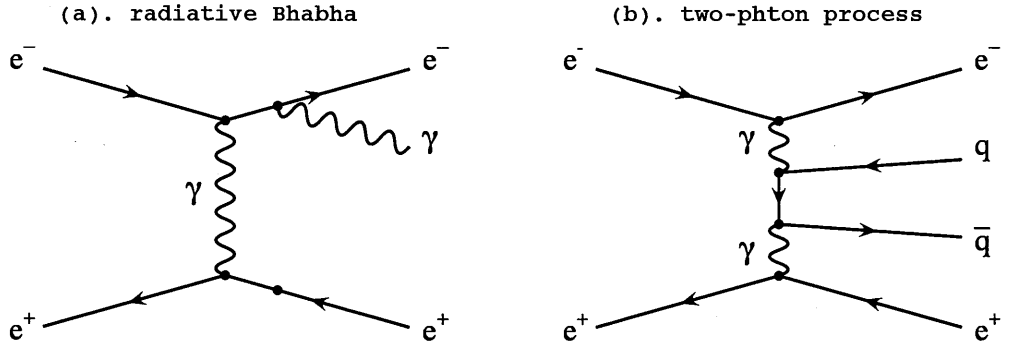

Figure 3.7: Feynmann diagrams of (a).radiative Bhabha and (b).two-photon process.

A remaining typical radiative Bhabha event is shown in Fig 3.8. Both of primary electron and positron radiate photons and then each photon converts into a pair of electron and positron. In this case, the numbers of charged tracks increase up to six and energy deposit in the calorimeters become large, thereby this type of events satisfy all the selection criteria.

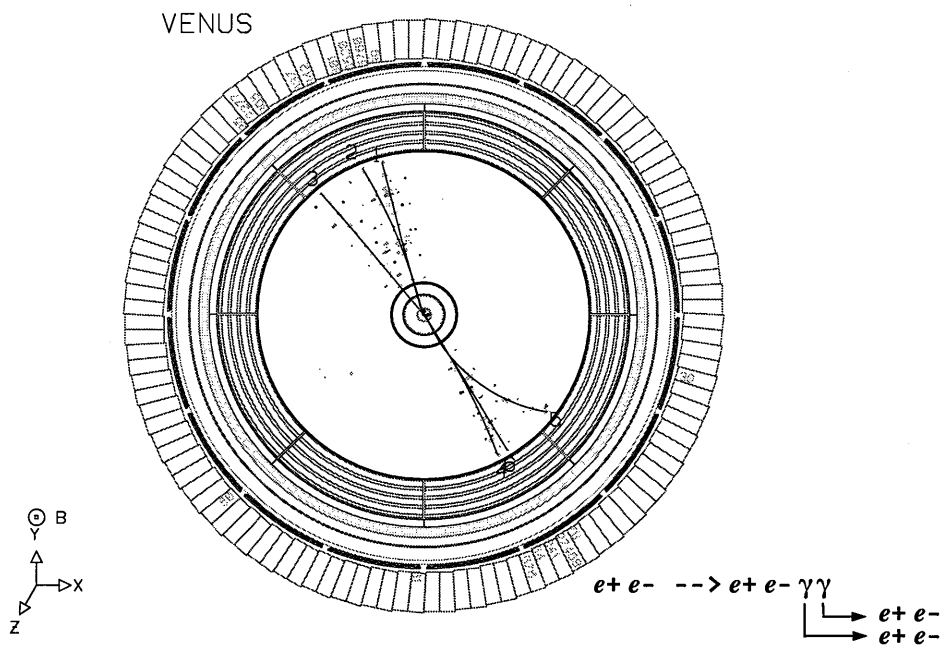

Figure 3.8: Radiative Bhabha event

Some of two-photon events, in which either or both of scattered electron (positron) would be detected in the VENUS detector, also remain. To study the forward-backward asymmetry by tagging prompt electrons, these backgrounds are harmful and not negligible. A typical electron inclusive event in two-photon process is shown in Fig. 3.9.

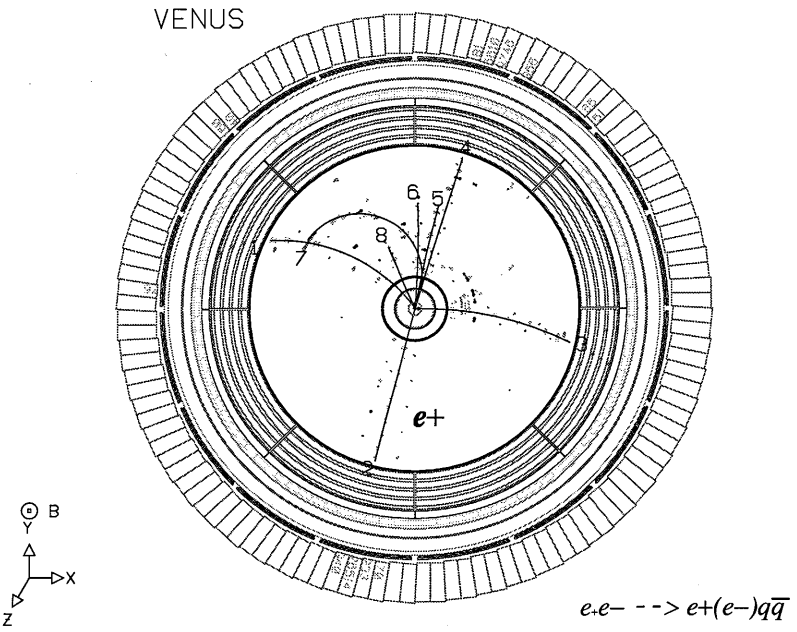

Figure 3.9: Electron inclusive event in two-photon process

To reduce these backgrounds, we reject events which satisfy any of the following criteria.

1. To reduce the radiative Bhabha events, we reject those which have two energetic clusters in LG or LA associated with CDC tracks. Here energetic cluster is defined as clusters which have energies larger than 15 GeV.

2. To reduce the electron inclusive events in two-photon process, we reject those in which there exist only one track whose E/p is lager than 0.7 in each of the hemispheres, Here, E/p is the ratio of the corresponding energy deposit E of a cluster to the momentum p of the track. If the tracks correspond to electrons, the values of E/p are ~ 1.

3.2.4 Summary

The efficiencies of all the selections described above are evaluated by using the event generator JETSET 7.3 [52] and the detector simulator VMONT (see Appendix C). It is found to be 74.9% for prompt lepton inclusive events as shown in Table 3.1. Because prompt leptons have high momentum, the efficiencies of the lepton inclusive events are higher than those for the ordinary hadronic events.

Selection & Rejection	Efficiency for ordinary hadron events	Efficiency for prompt lepton inclusive events
Hadronic event selection	73.0%	77.2%
Hard initial photon radiation event rejection	70.0%	75.1%
Radiative Bhabha & two-photon event rejection	69.7%	74.9%

Table 3.1: Efficiency of hadronic event selections.

The two-photon background is also studied by using Monte Carlo simulations of hadron-hadron scattering (VDM) [53], hard scattering of the partons (QPM) [54] and resolved photon process[2] (LAC) [55]. Contamination of these two-photon backgrounds in the final hadronic sample is found to be 0.5%. Similar to two-photon backgrounds, tau pair contamination is estimated to be 0.1%.

Selection & Rejection	Two-photon events	Tau pair events
Hadronic event selection	1.09%	0.18%
Hard initial photon radiation event rejection	0.55%	0.14%
Radiative Bhabha & two-photon event rejection	0.53%	0.14%

Table 3.2: Background contamination in hadronic event sample.

After all selections, 31830 (27428) events are obtained with the corresponding integrated luminosity of $\int \mathcal{L}dt = 262.4$ (226.7) pb^{-1} for electron (muon) analysis.

[2]For low Q^2 photon, partons of hadronic component in a photon play an important role. The two-photon collision via these partons interaction is called "resolved photon" process.

Chapter 4

Prompt electron tag

This chapter consists of three sections. First, we describe methods of electron identification and evaluation of their efficiencies. Second, we describe rejection of electrons from photon conversion, which are serious backgrounds for prompt electrons. Finally, we estimate the amount of backgrounds in the prompt electron candidates.

4.1 Electron identification

In this section, we describe methods of electron identification using the central drift chamber, the lead-glass calorimeter and the transition radiation detector in the VENUS detector.

An electron has two features to be distinguished from the other particle. First, it makes an electromagnetic shower in the calorimeters. Since LG and LA calorimeters are specified to detect the electromagnetic showers, they cannot detect whole of hadronic showers induced by hadrons. Therefore the electron is distinguished by comparing the corresponding momentum measured by CDC.

Second is the fact that the electron is the lightest charged particle. Since it is lighter than the other charged particle by two orders of magnitude, only the electron has very large Lorentz factor $\gamma \geq O(1000)$ in a wide momentum range (p=1$\sim$29 GeV/c). The transition radiation detector uses this feature to distinguish electrons from the other particles.

4.1.1 Electron identification with LG calorimeter

In detail, electron identification with LG is classified into two categories. First, we use the consistency of LG cluster energy with the corresponding momentum in CDC as mentioned above. Second, we use the informations of the shower shape.

The consistency of the calorimeter energy with the corresponding momentum is checked by the value of E/p. The ratio E/p should have a peak at around unity for an electron track, while it should be much smaller than 1 for the other charged particles.

First of all, we select the tracks by the following requirements.

$N_{\text{axial wire hits}}$	$\geq$	8
$N_{\text{slant wire hits}}$	$\geq$	4
$\lvert R_{\min}\rvert$	$<$	2 cm
$\lvert Z_{\min}\rvert$	$<$	20 cm
$\lvert\cos\theta\rvert$	$<$	0.68
p	$\geq$	1.0 GeV/c

Then we extrapolate the tracks to LG and calculate an energy of the electro-magnetic shower E as follows.

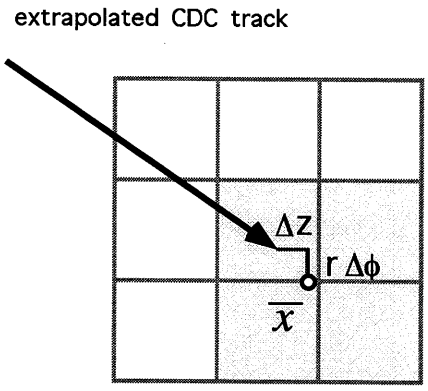

Figure 4.1: A cluster of LG blocks.

At first, we find the lead-glass block to be hit using CDC information. Next, around this block we find a maximum energy cluster of 2×2 array out of surrounding nine lead-glass blocks as shown in Fig. 4.1. Since the mean $\langle E/p\rangle$ and the deviation $\sigma_{E/p}$ of the E/p distribution for the electron are slightly dependent on their momentum, we rescale E/p to the following variable,

$$\mu = \frac{E/p - \langle E/p\rangle}{\sigma_{E/p}} \tag{4.1}$$

where $\langle E/p\rangle$ and $\sigma_{E/p}$ are given as a function of the electron momentum using the isolated electron samples beforehand. Here the isolated electron samples consist of single track events and Bhabha events, which are described in Appendix A.1.2 and A.1.1. The resulting μ distribution for the electron has a Gaussian shape with a unit variance, as shown in Fig. 4.2a. Figure. 4.2b shows that for pions. Pion samples are selected from hadronic events by using TRD information ($E_{\text{TRD}} < 5$ keV) as mentioned below. We choose a cut value $\mu \geq -2.5$ to select electrons.

The second set of variables for our electron identification with LG makes use of the fact that lateral spread of the shower is narrower for electrons than for pions with their hadronic interactions. Therefore, the center of gravity of the shower coincides with the track impact point better for electrons than for pions. We define the center of gravity ($\bar{x}$) in our chosen clusters made of four blocks as

$$\bar{x} = \sum E_i x_i / \sum E_i \tag{4.2}$$

The variables E_i and x_i denote the cluster energy and the center position of the four LG blocks ($i = 1, 2, 3, 4$). We define the variables $r\Delta\phi$ and Δz as the distance between $\bar{x}$ and the impact point on the block surface, extrapolated from the track measured by CDC. Distributions of $r\Delta\phi$ and Δz for the electron and the pion are also shown in Fig. 4.2a and 4.2b, respectively. We choose cut values of $r\Delta\phi$, $\Delta z < 6.5$ cm to select electrons.

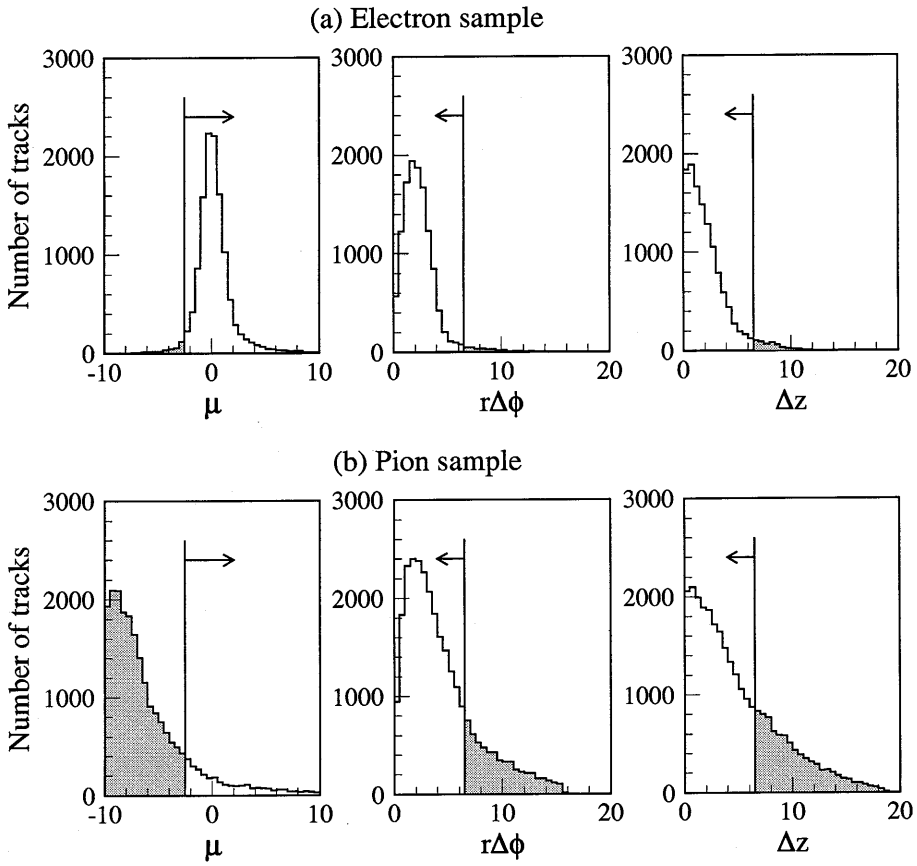

Figure 4.2: Distributions of the variables μ, $r\Delta\phi$ and Δz (a) for the electron and (b) for the pion.

4.1.2 Electron identification with the transition radiation energy (E_{TRD}).

Electrons, which have momentum of p >1 GeV/c, radiate X-ray called "transition radiation" at the boundary of two media. These transition radiation occur in the radiator box filled with polypropylene fibers and helium gas. Then the X-ray chamber, which is located just behind the radiator box, measures the transition radiation energy together with the ionization loss of the electron inside the chamber. In the case of pions, only ionization energies are measured. There are four modules, each of which consists of a pair of radiator box and X-ray chamber. Electrons are distinguished by pions by using the independent informations of four modules.

Because ionization energies fluctuate with the Landau distribution, a normal mean of the energies has long tail toward the side of larger energy deposit. This tail deteriorates the capability of the e/π separation. To reduce this tail, we use the truncated mean energy E_{TRD} which is calculated by discarding the largest energy deposit in the four energies. Figure 4.3 shows the distribution of the truncated mean energy for isolated electron and muon samples. We assume that the energy deposits of pions are the same as those of muons. Here isolated muon sample is two-photon events of $e^+e^- \rightarrow e^+e^-\mu^+\mu^-$, which is described in Appendix A.2.2,

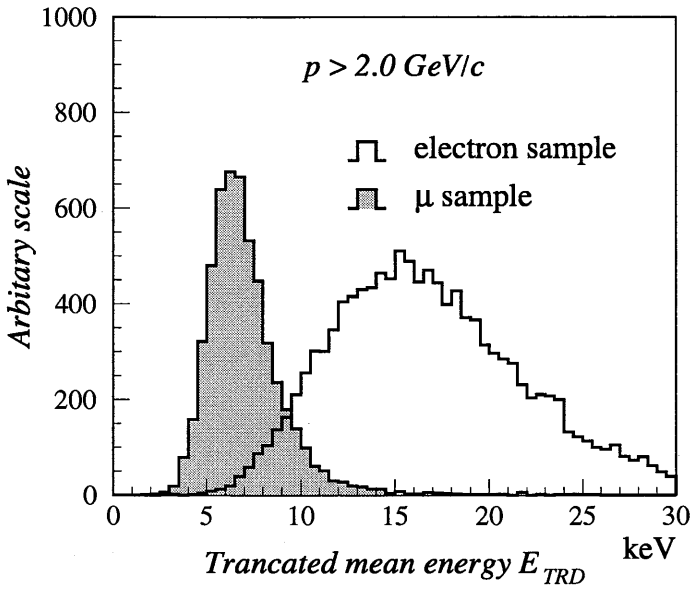

Figure 4.3: Truncated mean energy of TRD for electrons and muons

To separate electrons from the other particles, we apply a cut on the E_{TRD} spectrum in order to get a nearly constant electron efficiency of 80%. Since the pulse height for electrons increases with their momentum, so does the cut value. The values of $E_{\mathrm{TRD}}^{\mathrm{cut}}$ which gives about 80% electron efficiency is shown in Fig. 4.4. As a result, the pion efficiency is found to be around 3%.

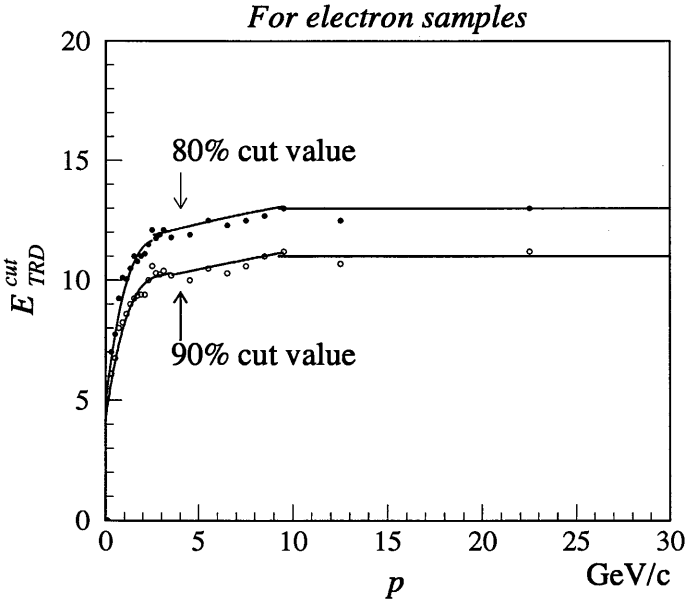

Figure 4.4: Cut value $E_{\mathrm{TRD}}^{\mathrm{cut}}$ as a function of the electron momentum.

4.1.3 The electron identification efficiency

Since particles from quark pair production are collimated in a narrow region, which is called as "jet", the electron track may overlap with nearby hadron tracks. Thus, the efficiency of electrons in hadronic jet is lower than that for the isolated case. The probability that an electron overlaps with other tracks becomes larger if the electron is closer to a jet axis, where the hadronic tracks are crowded. Therefore, we must give the electron efficiency in hadronic jets as a function of their momentum (p) and transverse momentum (p_t) with respect to the jet axis. Here jet axis is defined by the jet clustering with JADE algorithm as mentioned in Chap. 1.4.

To study the reduction in the electron efficiency due to overlapping, we use an isolated electron sample such as single track events together with hadronic event. We can simulate the electrons from heavy flavour decays in hadronic jets by embedding an isolated electron track onto hadronic events. We then reconstruct these embedded events with applying our electron identification procedure. From this study we found the electron identification efficiency with LG and TRD as a function of p and p_t. They are listed in Table 4.1 and 4.2. Errors in these table come from the limited statistics of our event sample.

p (GeV/c)	$p_t < 0.8$ (GeV/c)	$p_t > 0.8$ (GeV/c)
1 – 2	81.5 ± 1.9 %	89.4 ± 1.3 %
2 – 3	83.6 ± 2.0 %	89.2 ± 0.8 %
3 – 4	86.1 ± 2.0 %	91.3 ± 0.6 %
4 – 5	87.1 ± 2.4 %	91.3 ± 0.8 %
5 – 7	88.5 ± 1.9 %	91.3 ± 0.7 %
7 – 10	85.2 ± 2.3 %	91.8 ± 0.9 %
10 – 15	75.3 ± 3.4 %	89.4 ± 1.7 %
15 – 29	79.3 ± 4.3 %	87.3 ± 3.0 %

Table 4.1: Efficiency of LG method for electron in hadronic events.

p (GeV/c)	$p_t < 0.8$ (GeV/c)	$p_t > 0.8$ (GeV/c)
1 – 2	71.5 ± 2.1 %	73.6 ± 1.7 %
2 – 3	70.3 ± 2.3 %	77.9 ± 0.9 %
3 – 4	78.8 ± 2.1 %	77.1 ± 0.8 %
4 – 5	73.0 ± 2.9 %	75.4 ± 1.1 %
5 – 7	77.5 ± 2.3 %	74.9 ± 1.0 %
7 – 10	75.1 ± 2.6 %	74.5 ± 1.4 %
10 – 15	75.9 ± 3.3 %	76.2 ± 2.2 %
15 – 29	75.8 ± 5.4 %	80.2 ± 3.6 %

Table 4.2: Efficiency of TRD method for electron in hadronic events.

In determining probabilities to misidentify as an electron in hadronic events, we take advantage of the fact that we have two independent devices (LG and TRD) to identify electrons. We now reverse the role to select electrons into one to select clean pion sample in a device. This clean pion sample selected in one device enables us to determine the probability of pion misidentification in the other device. In practice, we select pion tracks of high purity by TRD with requirement that $E_{\rm TRD} < 5$ keV. Hereafter this pion sample is called "TRD pion sample". This selection provides an electron efficiency of 0.08% and impurity of electron is therefore negligibly small. The μ distribution of TRD pion sample is shown in Fig. 4.5 as shaded histogram and that of electron candidates, which are selected with TRD: *i.e.* $E_{\rm TRD} > E_{\rm TRD}^{\rm cut}$, is also shown by dots. They are normalized by the number of samples in the control region of $\mu < -7$.

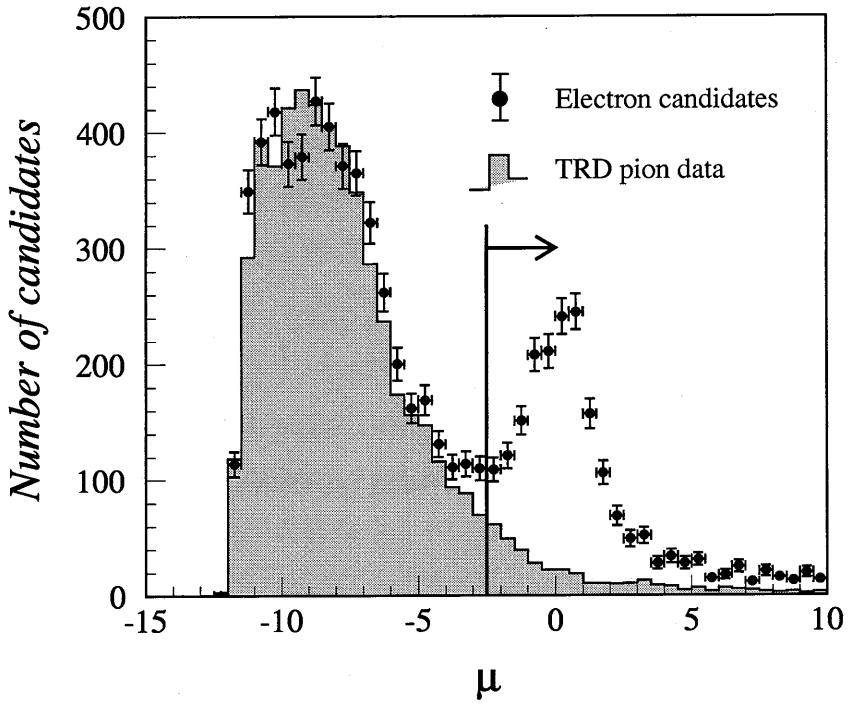

Figure 4.5: Distribution of μ in hadronic events. Plot and histogram indicate electron candidates and TRD pion samples, respectively.

Similarly, an independent selection of very clean pion tracks is made with LG by requiring $E/p < 0.5$ and this pion sample is called "LG pion sample" hereafter. The electron contamination in LG pion sample is also very small because the selection efficiency for electrons is 0.5%. In this way the pion misidentification probability of LG method is evaluated by TRD pion sample, and that of TRD method by LG pion sample. The corresponding probabilities of pion misidentification are given in Table 4.3 and 4.4, also in the same bins of p and p_t.

p (GeV/c)	$p_t < 0.8$ (GeV/c)	$p_t > 0.8$ (GeV/c)
1 – 2	5.8 ± 0.2	3.2 ± 0.4
2 – 3	4.3 ± 0.3	2.3 ± 0.5
3 – 4	5.7 ± 0.5	3.7 ± 0.7
4 – 5	5.5 ± 0.7	5.1 ± 1.0
5 – 7	5.8 ± 0.7	5.0 ± 1.0
7 – 10	5.6 ± 0.9	6.4 ± 1.5
10 – 15	2.4 ± 1.0	3.3 ± 1.5
15 – 29	9.8 ± 3.1	5.1 ± 3.0

Table 4.3: Pion misidentification probability of LG method for pion in hadronic events.

p (GeV/c)	$p_t < 0.8$ (GeV/c)	$p_t > 0.8$ (GeV/c)
1 – 2	9.6 ± 0.2 %	5.3 ± 0.3 %
2 – 3	8.4 ± 0.2 %	5.9 ± 0.4 %
3 – 4	9.1 ± 0.4 %	6.4 ± 0.6 %
4 – 5	9.3 ± 0.4 %	7.8 ± 0.5 %
5 – 7	9.3 ± 0.5 %	8.2 ± 0.6 %
7 – 10	11.0 ± 0.7 %	9.0 ± 0.8 %
10 – 15	8.4 ± 0.9 %	8.1 ± 1.0 %
15 – 29	9.5 ± 1.2 %	8.9 ± 1.5 %

Table 4.4: Pion misidentification probability of TRD method in hadronic events.

4.2 Rejection of electrons from photon conversions

Electron candidates which fulfill the electron identification criteria described above, contain not only electrons from heavy quark decay, but also those from Dalitz decay of neutral pions or conversions of photons in matter. The latter two are not "prompt electrons" and are called "conversion electrons" in this analysis.

We have two methods to reject the conversion electrons. The one is to tag them with their topology of a pair of oppositely charged tracks. The other is the informations of VTX chamber. Since most of conversions occur between VTX chamber and CDC as shown below, absence of corresponding track in VTX chamber indicates that the track is an conversion electron. By using the information of VTX chamber we can evaluate the efficiencies of the first method independently.

4.2.1 Rejection by the topology

If a pair of oppositely charged tracks satisfy all the four criteria described below, they are considered as conversion electrons to be rejected.

1. The minimum distance Δ between a pair of tracks is less than 1.5 cm.
   If a pair of the tracks come from a photon conversion, these trajectories should meet at a point exactly. Due to the uncertainties in track reconstruction, most of them either overlap or are separated slightly by a minimum distance Δ as shown in Fig. 4.6.

2. The opening angle $\theta_{\rm conv}$ between the two tracks at the crossing point is small.
   If both tracks are reconstructed in three dimensions, we require $\cos\theta_{\rm conv} > 0.85$. If one of the two tracks is not reconstructed in three dimensions, we require $\cos\theta_{\rm conv} > 0.95$ in the x-y plane, respectively.

3. The direction of the momentum sum vector $\overrightarrow{p_1} + \overrightarrow{p_2}$ is consistent with that of conversion point $\overrightarrow{v_\gamma}$.
   In practice, we require that the angle α is smaller than 0.15 rad, where α is the angle between the momentum sum vector $(\overrightarrow{p_1} + \overrightarrow{p_2})$ of the track pair and the direction vector $(\overrightarrow{v_\gamma})$ from the e^+e^- interaction point to the photon conversion point.

4. The invariant mass M_{ee} of a pair of tracks is less than 0.2 GeV.
   The invariant mass is calculated by assuming an electron mass.

Figure. 4.7 shows distribution of the conversion points, which is defined as the midpoint of the closest approach of the candidate track pairs as defined for the above criteria. Monte Carlo data is also indicated as histogram. Clear peaks are found at $R \sim 15$ and 25 cm. They correspond to the outer wall of the vertex chamber and support cylinder of the trigger chamber, whose thickness correspond to the 3.9% and 2.9% radiation length, respectively. They are consistent with each other within their statistical error.

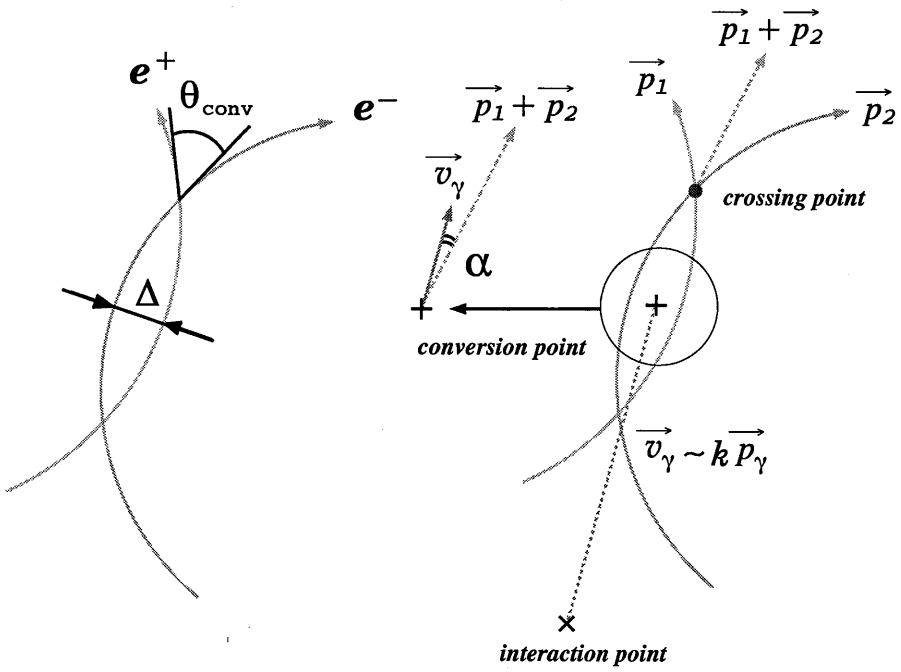

Figure 4.6: Definition of the variables Δ, θ_{conv}, and α.

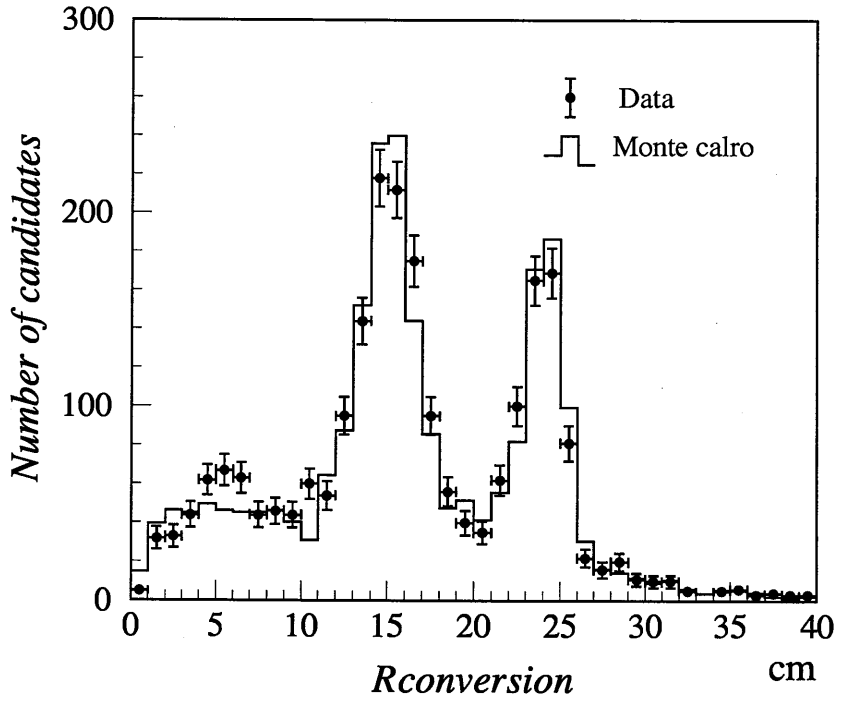

Figure 4.7: Conversion points distribution of the photon conversion pairs. Monte Carlo prediction is also shown in histogram.

4.2.2 Estimation of the rejection probability

We evaluate the rejection probability for prompt electrons by assuming that pions are the same as prompt electrons in the view of the topology. Therefore we evaluate the accidental rejection probability of prompt electron by using pion samples. Pion samples are available by the requirements of $E/p < 0.5$ or $E_{\rm TRD} < 5$ keV as mentioned in the previous section. By applying of the rejection procedure to these samples, we find the accidental rejection probabilities to be 14.7 $\pm$ 0.4 % and 14.6 $\pm$ 0.2 % for LG and TRD pion samples, respectively. They are consistent within the statistical error with each other. Table 4.5 shows the probability of LG pion sample in bins of p and p_t.

p (GeV/c)	$p_t < 0.8$ (GeV/c)	$p_t > 0.8$ (GeV/c)
1 – 2	15.2 $\pm$ 0.6 %	4.3 $\pm$ 0.9 %
2 – 3	15.0 $\pm$ 0.9 %	8.7 $\pm$ 1.8 %
3 – 4	15.6 $\pm$ 1.2 %	8.1 $\pm$ 2.0 %
4 – 5	13.5 $\pm$ 1.5 %	10.6 $\pm$ 2.7 %
5 – 7	12.8 $\pm$ 1.4 %	5.6 $\pm$ 1.6 %
7 – 10	10.7 $\pm$ 1.6 %	8.0 $\pm$ 2.1 %
10 – 15	6.6 $\pm$ 1.4 %	4.8 $\pm$ 1.6 %
15 – 29	7.4 $\pm$ 2.8 %	5.1 $\pm$ 3.0 %

Table 4.5: Rejection probability of pions tagged with LG. This is used as the probability for prompt electrons.

For the evaluation of the rejection efficiency for the conversion electrons, we use the conversion track sample tagged with VTX chamber. We select those tracks by requiring no corresponding track segments in VTX chamber as described above. The corresponding tracks are found by taking into account the effect of multiple coulomb scattering. This selection provides the conversion track sample with its purity of 65.6 $\pm$ 2.5%. By examining thus selected sample the rejection probability for conversion electrons is found to be 84.4 $\pm$ 1.0 $\pm$ 0.4 %, after the correction due to the purity. The first error is statistical and the second one is due to the uncertainty in the purity of the sample. It is consistent with that of Monte Carlo prediction of 83.7 $\pm$ 0.8 %.

Once we have confirmed the reliability of the Monte Carlo prediction, we will use the rejection probability for the conversion electron for each bin of p and p_t as evaluated by a Monte Carlo simulation as listed in Table 4.6.

p (GeV/c)	$p_t < 0.8$ (GeV/c)	$p_t > 0.8$ (GeV/c)
1 – 2	80.3 ± 0.6 %	68.6 ± 4.2 %
2 – 3	82.3 ± 1.2 %	80.8 ± 4.0 %
3 – 4	80.8 ± 1.9 %	88.2 ± 3.7 %
4 – 5	81.3 ± 2.7 %	89.6 ± 4.4 %
5 – 7	78.9 ± 3.2 %	87.5 ± 4.4 %
7 – 10	78.2 ± 4.4 %	93.8 ± 4.3 %
10 – 15	81.3 ± 5.6 %	83.3 ± 8.8 %
15 – 29	80.3 ± 8.6 %	87.4 ± 9.2 %

Table 4.6: Rejection probability of conversion electrons

4.3 Background estimation

After the selection with LG and TRD and together with the rejection of the conversion electrons, a total of 2129 candidates are obtained with corresponding integrated luminosity of $\int \mathcal{L}dt = 262.4$ pb^{-1}.

In this section, we evaluate the amount of pion and conversion electron backgrounds in the candidates. The amount of backgrounds are calculated by solving the following equations,

$$N_{\text{before}} = N_p/\epsilon_p + N_{bg}/\epsilon_{bg} \tag{4.3}$$

$$N_{\text{after}} = N_p + N_{bg}. \tag{4.4}$$

N_{before} and N_{after} are the number of candidates before and after selection. N_p, N_{bg}, ϵ_p and ϵ_{bg} are the number and the efficiency of prompt electrons and backgrounds, respectively. As a result, N_{bg} is expressed by the following formula,

$$N_{bg} = \frac{\epsilon_{bg}}{\epsilon_p - \epsilon_{bg}} (\epsilon_p N_{\text{before}} - N_{\text{after}}). \tag{4.5}$$

In the following section, we perform the background estimation with this method for pion and the conversion electron backgrounds, respectively.

4.3.1 Pion backgrounds

We have three ways to obtain the number of pion backgrounds as shown in Fig. 4.8.

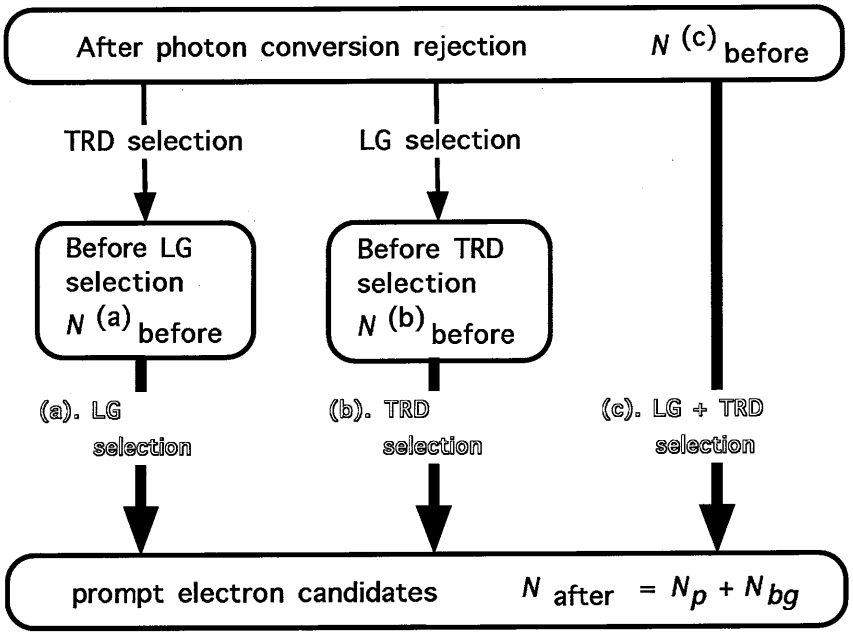

Figure 4.8: Flow chart of prompt electron selection

N_{before} are 13047, 8530 and 142001 for (a), (b) and (c) in Fig. 4.8, respectively. As the results, the total numbers of pion background are

$$\text{(a)} \quad N_{bg} = 582.8 \pm 8.5 \pm 9.4, \tag{4.6}$$

$$\text{(b)} \quad N_{bg} = 583.7 \pm 5.9 \pm 16.6 \tag{4.7}$$

and

$$\text{(c)} \quad N_{bg} = 601.3 \pm 1.7 \pm 17.1. \tag{4.8}$$

The first error is statistical and the second one is due to the uncertainty of the efficiencies. The evaluated numbers for (a), (b) and (c) are consistent with each other within the errors.

4.3.2 Conversion electrons

The amount of conversion electrons is evaluated by the same method as that used for pion backgrounds. The number of candidates N_{before}, after selections with LG and TRD and just before the rejection of conversion electrons, is 4406. The number of final electron candidates N_{after} is 2129 as mentioned above. By using Tables 4.5 and 4.6, we obtain the number of conversion electrons in the final electron sample.

We summarize the numbers of electron candidates, pion and conversion backgrounds in Table 4.7. The first error is statistical and the second one is due to the uncertainty of the selection efficiencies.

p	(p_t)	$N_{\text{cand.}}$	N_π	$N_{\text{conv.}}$
1 – 2	< 0.8	771	$256.56 \pm 4.11 \pm 9.55$	$305.83 \pm 9.45 \pm 12.17$
	> 0.8	69	$15.79 \pm 0.74 \pm 2.23$	$20.52 \pm 3.21 \pm 4.09$
2 – 3	< 0.8	330	$78.40 \pm 1.93 \pm 5.57$	$76.85 \pm 4.54 \pm 6.62$
	> 0.8	65	$6.08 \pm 0.38 \pm 1.26$	$7.25 \pm 1.47 \pm 1.94$
3 – 4	< 0.8	192	$58.78 \pm 1.92 \pm 5.35$	$34.18 \pm 3.33 \pm 4.43$
	> 0.8	48	$7.98 \pm 0.56 \pm 1.64$	$3.35 \pm 0.73 \pm 1.21$
4 – 5	< 0.8	123	$37.63 \pm 1.51 \pm 4.74$	$12.60 \pm 2.07 \pm 2.38$
	> 0.8	75	$7.28 \pm 0.64 \pm 1.60$	$0.25 \pm 0.41 \pm 0.32$
5 – 7	< 0.8	128	$42.21 \pm 1.65 \pm 5.35$	$15.65 \pm 2.45 \pm 3.18$
	> 0.8	83	$12.36 \pm 0.82 \pm 2.66$	$2.60 \pm 0.70 \pm 1.08$
7 – 10	< 0.8	74	$25.36 \pm 1.25 \pm 4.51$	$7.54 \pm 1.73 \pm 2.05$
	> 0.8	82	$13.64 \pm 0.98 \pm 3.34$	$0.72 \pm 0.29 \pm 0.55$
10 – 15	< 0.8	40	$5.48 \pm 0.38 \pm 2.27$	$2.38 \pm 0.85 \pm 0.90$
	> 0.8	34	$4.64 \pm 0.41 \pm 2.13$	$0.87 \pm 0.50 \pm 0.57$
15 – 29	< 0.8	11	$8.16 \pm 0.98 \pm 2.95$	$0.78 \pm 0.50 \pm 0.44$
	> 0.8	4	$3.38 \pm 0.43 \pm 2.11$	$0.40 \pm 0.25 \pm 0.34$

Table 4.7: Table of electron candidates and estimated background in bins of p and p_t.

Chapter 5

Prompt muon tag

5.1 Muon identification with the barrel muon chambers

In this section, we describe a method of muon identification using the barrel muon chamber system. The barrel muon chamber system, as mentioned in Chap. 2.2.9, is the outermost device in the VENUS detector and consists of four sectors, *i.e.* left, right, up and bottom sectors. Each sector consists of two iron plates called "muon filters" interleaved with drift chambers as shown in Fig. 5.1. The thickness of each muon filter is chosen to be about one nuclear absorption length of 20 cm. To reach the outermost layer of the muon chamber, a particle produced at e^+e^- interaction point must pass through at least 5.3 nuclear absorption length. Most of the hadrons stop at LG, the return yoke or the muon filters. Only muons can penetrate all of them. This feature is used to distinguish muons from hadrons.

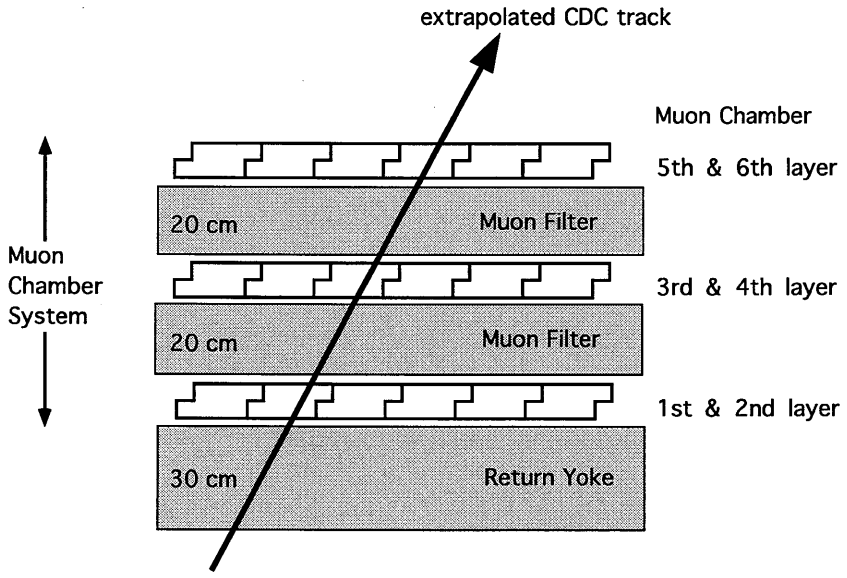

Figure 5.1: Schematic view of muon chamber system.

5.1.1 Extrapolation to the muon chamber system

Only tracks which satisfy the following requirements are extrapolated to the muon chamber system.

$N_{\text{axial wire hits}}$	$\geq$	8
$N_{\text{slant wire hits}}$	$\geq$	4
$\lvert R_{\text{min}}\rvert$	$<$	2 cm
$\lvert Z_{\text{min}}\rvert$	$<$	20 cm
$\lvert\cos\theta\rvert$	$<$	0.7
p	$\geq$	2.0 GeV/c

In the extrapolation, we take into account the energy loss and the bending effects due to the magnetic field in the return yoke. When a muon has momenta of 2 GeV/c, the typical magnitude of the energy loss is 1.2 GeV.

After extrapolation to the muon chamber system, we look for muon chamber hits around the extrapolated track. Figure 5.2 shows the distribution of normalized distance of the muon chamber hits from the extrapolated track. Here we used a muon sample in two-photon production events ($e^+e^- \to e^+e^-\mu^+\mu^-$). This sample is called "isolated muon sample" in this analysis. Selection of the isolated muon sample is described in Appendix A.2.2. The normalization factor σ_d^i is determined for each i-th layer by considering both multiple Coulomb scattering and extrapolation error. The amount of multiple Coulomb scattering is calculated by using particle momenta and path length in the materials.

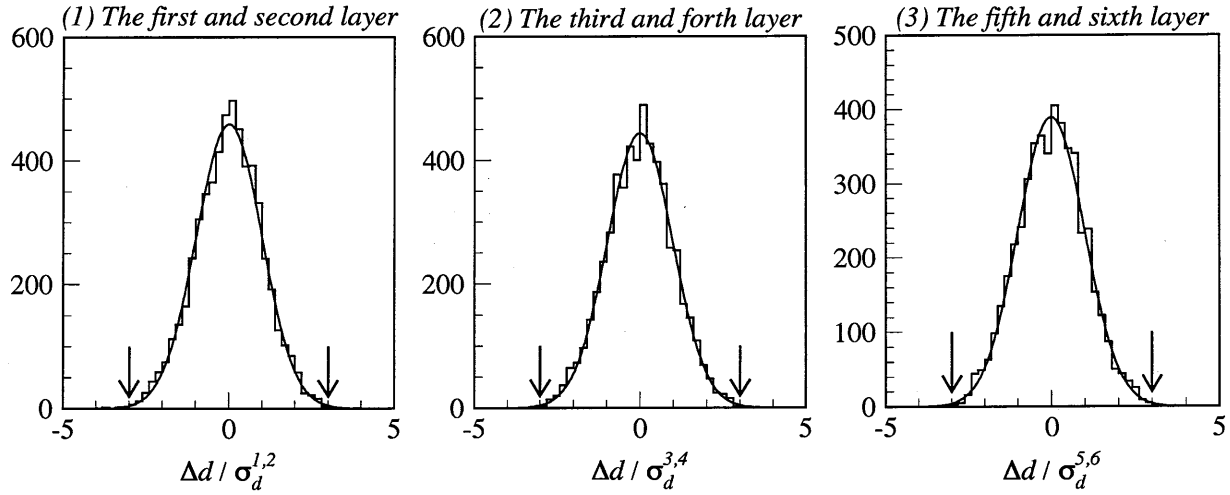

Figure 5.2: Normalized distance ($\Delta d/\sigma_d$) distributions for isolated muon sample, where Δd is the distance between the chamber hit position and that extrapolated from CDC, and σ_d^i is calculated from multiple Coulomb scattering.

Table 5.1 summarizes the standard deviation of the normalized distance at each layer and sector. Since all of the standard deviations are about unity, the deviations close to unity indicate that the scale factors based on multiple Coulomb scattering are reasonable.

layer	sector				
	1	2	3	4	total
1 & 2	0.97	1.00	0.98	1.06	1.00
3 & 4	0.99	0.96	0.95	1.06	0.99
5 & 6	0.99	0.96	0.98	1.07	0.99

Table 5.1: Standard deviation of normalized distance in each sector and layer.

Those hits within $3\sigma_d^i$ are used to reconstruct a muon local track. The probability to find muon chamber hits in more than 4 out of 6 layers is 89% for the isolated muon sample with $p > 2$ GeV/c. as shown in Fig. 5.3.

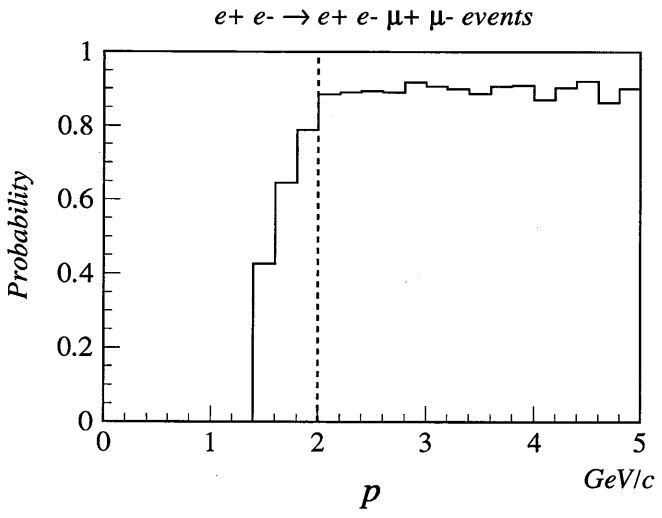

Figure 5.3: Probability that the hits are found in more than 4 layers as a function of muon momentum.

5.1.2 Local track reconstruction

Since we have six layers of muon chambers, we can reconstruct a muon track using their hit informations alone, independent of CDC track. The local track reconstruction is done by the least-squares method [56, 57]. In estimating the chi-squares, we properly take into account the correlation of the hits among different layers due to the multiple scattering effects. To get the best estimation of the track, the fit quality $\chi^2_{\rm fit}$ is defined as the following equation,

$$\chi^2_{\rm fit} = \sum_{ij} [\, r_i - l_i(\vec{\alpha}) \,]\; C^{-1}_{ij}\; [\, r_j - l_j(\vec{\alpha}) \,] \tag{5.1}$$

where r_i is drift distance recorded at the corresponding wire in the i-th layer, l_i is distance from the wire to the local track $\vec{\alpha}$ as shown in Fig. 5.4, and C_{ij} is correlation matrix among the layers.

The local track $\vec{\alpha}$ is represented by the position $d_{\rm in}$ and the direction $\phi_{\rm in}$ at outer surface of the return yoke in the x-y plane, that is $\vec{\alpha} = \vec{\alpha}(d_{\rm in}, \phi_{\rm in})$. We choose a cut value of 0.0027 on the chi-square probability of the least squares fit. This provides an efficiency of 93% for the isolated muon sample. Figure 5.5 shows the chi-square probability for the isolated muon sample.

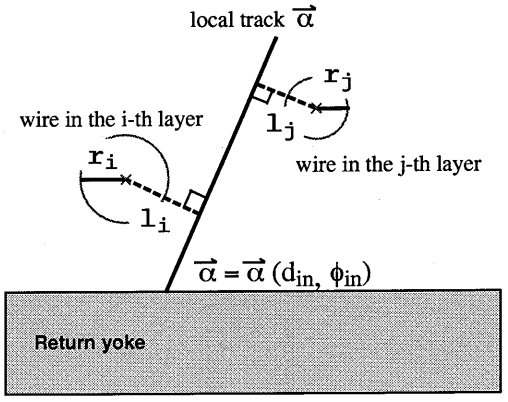

Figure 5.4: Parameters used in local track reconstruction.

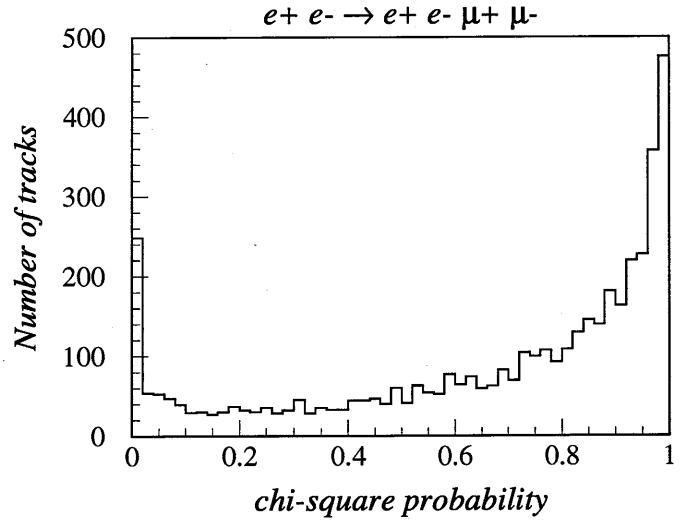

Figure 5.5: Chi-square probability for the isolated muon sample.

5.1.3 Track matching

We now have the local tracks reconstructed in the muon chambers. We check the consistency between the local and extrapolated tracks by comparing their position $d_{\rm in}$ and angle $\phi_{\rm in}$. Figure 5.6 shows the definition of the matching parameters (Δd and $\Delta\phi$). They are difference of position and angle in x-y plane from the extrapolated track, respectively.

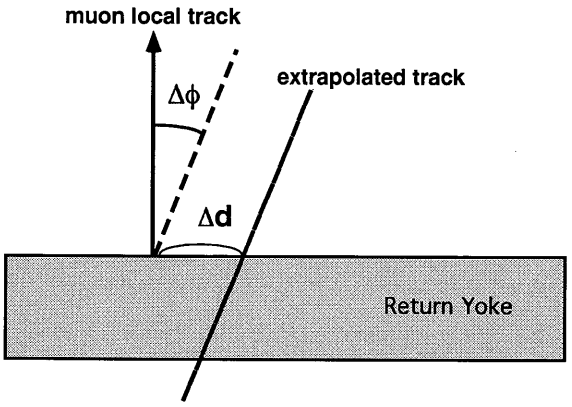

Figure 5.6: Matching parameters (Δd and $\Delta\phi$) between CDC and muon local track at the outer surface of the return yoke.

As shown in Fig. 5.7, a clear positive correlation exists between the two variables. This correlation is obvious because the two variables tend to increase (decrease) at the same time as the multiple scattering effects on the track is large (small). In order to take into account this correlation, we redefine the matching parameters as follows:

$$A = \frac{\Delta d}{\sigma_d}, \qquad B = \frac{\Delta\phi}{\sigma_\phi}, \tag{5.2}$$

$$X = \frac{A - B}{1.075}, \qquad Y = \frac{A + B}{2.150}, \tag{5.3}$$

where normalization factors (1.075 and 2.150) are determined to obtain Gaussian distributions with a unit variance for the new variables (X and Y) for the isolated muon sample. To evaluate the quality of matching, we also define the following variable,

$$\chi^2_{\rm matching} = X^2 + Y^2. \tag{5.4}$$

To have a good matching quality we require $\chi^2_{\rm matching} < 9.0$. This is determined by using the isolated muon sample as shown in Fig. 5.7 with a solid ellipse. This provides an efficiency of 90% for the isolated muon sample as shown in Fig. 5.8.

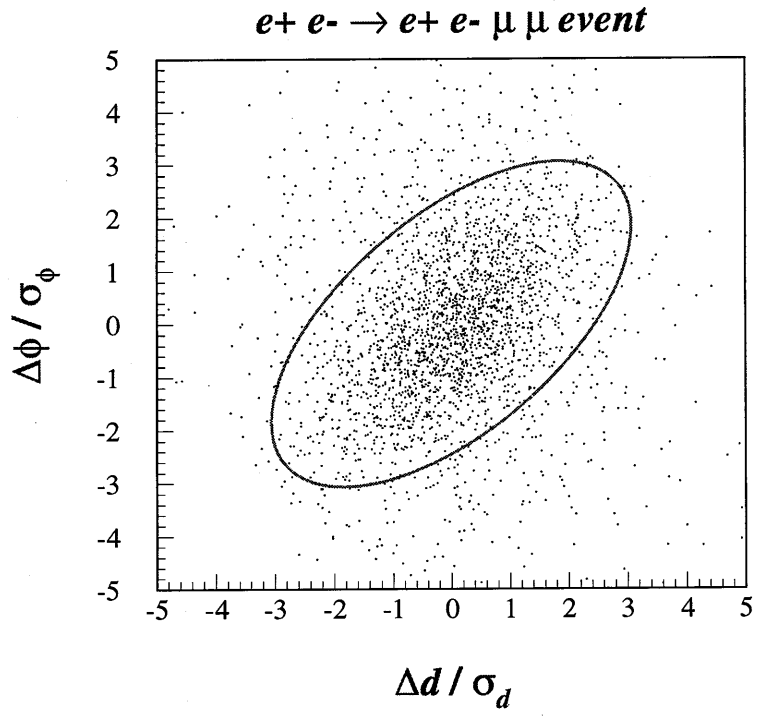

Figure 5.7: Matching parameters between CDC and muon local track for the isolated muon sample

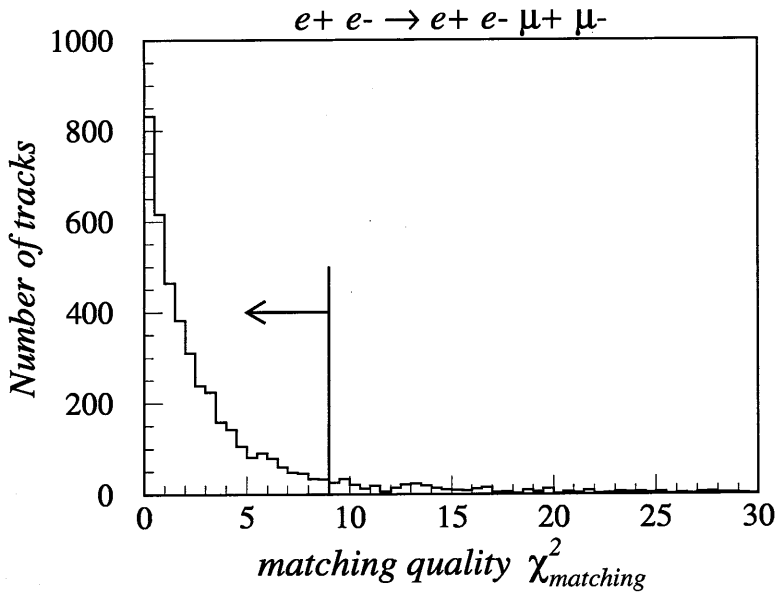

Figure 5.8: Distribution of the matching quality χ^2_{matching} for the isolated muon sample.

5.2 The muon identification efficiency

First, we estimate the efficiency for the isolated muon sample when we apply the muon identification described in the previous section. The results are summarized in Table 5.2.

Selection	# of tracks
after track selection	5323
4/6 hits requirement	4757
local track reconstruction	4401
matching between CDC track	3942
Efficiency	74.1 ± 0.6%

Table 5.2: Muon identification efficiency for the isolated muon sample.

Next, we estimate the efficiency of the muon identification in the hadronic events. The efficiency is evaluated by using embedding method similar to that is applied for electron identification in hadronic events. Table 5.3 shows efficiencies of muon identification in hadronic events in bins of p and p_t.

p (GeV/c)	p_t <0.8 (GeV/c)	p_t >0.8 (GeV/c)
2 – 3	69.1 ± 1.2 %	66.5 ± 0.9 %
3 – 4	70.1 ± 1.8 %	70.1 ± 1.5 %
4 – 5	72.3 ± 2.6 %	68.8 ± 2.4 %
5 – 7	69.8 ± 2.6 %	63.6 ± 2.8 %
7 – 10	66.9 ± 3.7 %	67.1 ± 3.8 %
10 – 15	68.6 ± 6.6 %	66.6 ± 4.6 %
15 – 29	57.6 ± 2.7 %	57.0 ± 3.2 %

Table 5.3: Muon identification efficiency in hadronic events.

We have a total of 27428 hadronic events which corresponds to the integrated luminosity of $\int \mathcal{L}dt = 262.4$ pb^{-1}. When we apply the present muon identification to our total hadronic event sample, we obtain 1411 muon candidates in total.

5.3 Hadron misidentification

In this section, we describe hadron misidentification. Sources of hadron misidentification in our extraction of muon sample are classified into two categories. The first one is π's and K's produced in the hadronic events which decay into muons in flight. It is difficult to distinguish those muons from prompt muons. Those hadrons are called "decaying hadrons" in this analysis. The second category is hadrons which survive from the interaction in the absorption materials. They are called "non-decaying hadrons".

5.3.1 Estimation of the misidentification probability

To evaluate the misidentification probability, we use samples of τ and K_S* decays.

The pion sample from τ decays is selected in τ pair production events. The selection is made for three-prong τ decays (see Appendix A.3.1). For example, a three-prong τ decay is the following processes,

$$e^+e^- \to \tau^+\tau^- \to \begin{cases} \tau^+ \to \pi^\pm\pi^\mp\pi^\pm X \\ \tau^- \to \mu^-\overline{\nu}_\mu\nu_\tau \end{cases} \tag{5.5}$$

This sample has a small impurity of muons coming from $\tau^- \to \mu^-\overline{\nu}_\mu + \gamma \to \mu^-\overline{\nu}_\mu + e^+e^-$. The impurity in this sample is found to be 0.14%. This corresponds to the number of the final candidates of 0.8 in Table 5.4. After correction for this impurity, the probability is found to be $0.68 \pm 0.32\%$. The error is due to statistics of the sample.

Another independent evaluation is made with $K_S \to \pi^+\pi^-$ sample selected by their lifetime and invariant mass in hadronic events. Similar to τ decays, the K_S decay samples contain muons with an impurity of 0.5% and the number of muons is expected 5.7 out of 16 in Table 5.2. After the correction, the probability is found to be $0.64 \pm 0.25\%$.

Sample	τ decays	K_S decays
after track selection	765	1617
4/6 hits requirement	27	73
local track reconstruction	12	32
matching between CDC track	6	16
misidentification probability	0.68 $\pm$ 0.32%	0.64 $\pm$ 0.25%

Table 5.4: Hadron misidentification probability for pion control samples.

Since the statistics of τ/K_S decay samples is not enough, momentum (p) and transverse momentum (p_t) dependence of the probability cannot be studied in hadronic events. Therefore

*K_S denotes neutral kaon of short lifetime.

detailed study relies on Monte Carlo simulation. In the detector simulator VMONT, decay of hadrons, energy loss and nuclear scattering in the materials are simulated. Details of simulation is described in Appendix C.

The misidentification probability in hadronic events thus evaluated by Monte Carlo simulation are shown in Table 5.5. The error is due to the limited statistics of the Monte Carlo data sample. The evaluated probability is consistent with those from τ decays or K_S decays sample.

p (GeV/c)	$p_t < 0.8$ (GeV/c)	$p_t > 0.8$ (GeV/c)
2 – 3	0.64 ± 0.03 %	0.47 ± 0.07 %
3 – 4	0.52 ± 0.04 %	0.49 ± 0.09 %
4 – 5	0.27 ± 0.04 %	0.32 ± 0.08 %
5 – 7	0.23 ± 0.03 %	0.22 ± 0.06 %
7 – 10	0.07 ± 0.02 %	0.12 ± 0.05 %
10 – 15	0.08 ± 0.04 %	0.05 ± 0.04 %
15 – 29	0.04 ± 0.04 %	0.00 ± 0.00 %

Table 5.5: Hadron misidentification probability evaluated with Monte Carlo simulation.

5.4 Background estimation

In the 1411 muon candidates, the number of backgrounds which results from misidentification of hadrons is estimated by a Monte Carlo simulation as follows.

p (GeV/c)	(p_t)	$N_{\text{cand.}}$	N_{bg}
2 – 3	< 0.8	439	$292.3 \pm 10.7 \pm 58.5$
	> 0.8	90	$36.1 \pm 3.8 \pm 7.2$
3 – 4	< 0.8	212	$137.1 \pm 7.4 \pm 27.4$
	> 0.8	64	$28.4 \pm 3.3 \pm 5.7$
4 – 5	< 0.8	125	$73.8 \pm 5.4 \pm 14.8$
	> 0.8	50	$18.8 \pm 2.7 \pm 3.8$
5 – 7	< 0.8	122	$57.4 \pm 4.8 \pm 11.5$
	> 0.8	83	$24.4 \pm 3.1 \pm 4.9$
7 – 10	< 0.8	82	$37.0 \pm 3.8 \pm 7.4$
	> 0.8	50	$12.9 \pm 2.3 \pm 2.6$
10 – 15	< 0.8	34	$14.1 \pm 2.4 \pm 2.8$
	> 0.8	37	$8.2 \pm 1.8 \pm 1.6$
15 – 29	< 0.8	11	$1.6 \pm 0.8 \pm 0.3$
	> 0.8	12	$4.3 \pm 1.3 \pm 0.9$

Table 5.6: Table of prompt muon candidates and hadron backgrounds in bins of p and p_t.

The first error is statistical and the second is systematic as described in Appendix B. The systematic error is common to each bin of p and p_t.

Chapter 6

Evaluation of the cross-section and its asymmetry

We have selected samples of 2129 electron and 1411 muon candidates. The data correspond to the integrated luminosity $L = \int \mathcal{L} dt = 262.4$ and 226.7 pb^{-1} for electrons and muons, respectively.

As mentioned in Chap. 1.4 heavy quarks (c and b quark) tend to fragment harder than light quarks (u, d and s quark), hence produce leptons of higher p. Using this feature we can separate lepton candidates into c, b quark and background contributions statistically. Background contributions are well understood by evaluating hadron misidentification and conversion rejection probability with several control samples and Monte Carlo simulation as described in the previous chapters. Hence we can measure the total cross-section of heavy quark pair production from p and p_t spectrum, and measure the forward backward asymmetry from the angular distribution of the thrust axis containing the leptons.

6.1 Cross-section of heavy quark pair production

In the quark pair production, the sources of observed leptons are categorized as follows.

1. Semileptonic decays of c hadrons: denoted cp.
2. Semileptonic decays of b hadrons: denoted bp.
3. Cascade decays from a b quark ($b \to c \to l$): denoted bc.
4. Cascade decays from a b quark via $b \to u$ transition ($b \to u \to l$): denoted bu.
5. Decays of a τ from a b decay ($b \to \tau \to l$): denoted $b\tau$.
6. Leptons from non-prompt sources or hadrons misidentified as leptons: denoted bg.

Observed numbers of lepton candidates in bins of (p, p_t) are expressed by the sum of the terms corresponding to the sources described above,

$$\begin{aligned} N_{\rm data}(p,p_t) &= \{\ \sigma_c B_c P_{cp}(\langle x_c\rangle, p, p_t) \\ &+ \sigma_b B_b P_{bp}(\langle x_b\rangle, p, p_t) \\ &+ \sigma_b B_{bc} P_{bc}(\langle x_b\rangle, p, p_t)\cdot(1+\alpha) \\ &+ \sigma_b B_{bu} P_{bu}(\langle x_b\rangle, p, p_t) \\ &+ \sigma_b B_\tau P_{b\tau}(\langle x_b\rangle, p, p_t)\ \}\cdot 2L\cdot\varepsilon(p,p_t) \\ &+ N_{bg}(p,p_t) \end{aligned} \tag{6.1}$$

Here σ_c and σ_b are the cross-sections of c and b quark pair production event. B_c and B_b are semi-leptonic branching ratios of the c and b hadrons. B_{bc}, B_{bu} and $B_{b\tau}$ are $b \to c + l\nu_l$ and $u + l\nu_l, b \to \tau \to l$ decay branching ratio, respectively.

$P_i(\langle x_q\rangle, p, p_t)$ is the probability that a lepton produced from a type i decay ($i = cp, bp, bc, bu, b\tau$) is found in a bin of (p, p_t), which is expressed as follows

$$P_i(\langle x_q\rangle, p, p_t) = \frac{\displaystyle\int_0^1 D(x,\epsilon_q)\cdot W_i(x,p,p_t)\ dx}{\displaystyle\int_0^1 D(x,\epsilon_q)\ dx}\ , \tag{6.2}$$

where $\langle x_q\rangle$ is the mean of x: $\langle x_q\rangle = \int xD(x,\epsilon_q)\ dx\ /\ \int D(x,\epsilon_q)\ dx$. We use $\langle x_q\rangle$ instead of ϵ_q as a fragmentation parameter in the following analysis. $D(x,\epsilon_q)$ is the Peterson function formulated with the scaled energy of the hadron $x = E_{\rm hadron}/E_{\rm beam}$, defined as

$$D(x,\epsilon_q) = \frac{1}{x}\left(1 - \frac{1}{x} - \frac{\epsilon_q}{1-x}\right)^{-2}. \tag{6.3}$$

$W_i(x,p,p_t)$ is the probability that the daughter lepton is found in a bin of (p, p_t) for a parent hadron with the scaled energy x. This is evaluated by the Monte Carlo simulation beforehand.

α is the branching ratio of $b \to c\bar{c}s$. L is integrated luminosity which corresponds to 262.4 (226.7) pb^{-1} for the electron (muon) sample. $\varepsilon(p,p_t)$ is the efficiency for leptons to pass all of the lepton selection criteria. $N_{bg}(p,p_t)$ represents the number of backgrounds which is listed in the previous chapters.

The fragmentation parameter $\langle x_q\rangle$ and the semileptonic decay branching ratio B_q are fixed to the world average values as listed in Table 6.1 [1].

[1] Among them, those used values for $B_c, B_b, \langle x_c\rangle$ and $\langle x_b\rangle$ are found to be consistent with the independent fit to our data, where the cross-sections are fixed to the Standard Model predicted values. The details are described in Appendix D.

parameter	world average values
B_c	9.8 ± 0.5 %
B_b	11.13 ± 0.29 %
B_{bc}	7.9 ± 0.8 %
B_{bu}	0.3 ± 0.2 %
$B_{b\tau} = \mathrm{BR}\ (b \to \tau\nu_\tau X)$	0.48 %
$\cdot\ \mathrm{BR}\ (\tau \to e\nu_e\nu_\tau)$	
$\alpha = \mathrm{BR}\ (b \to c\bar{c}s)$	16.5 %
$\langle x_c \rangle$	0.51 ± 0.02
$\langle x_b \rangle$	0.70 ± 0.02

Table 6.1: World average values of the parameters [58, 59].

Then we perform a fit using σ_q as free parameters. Figures 6.1 and 6.2 show the best fits of p and p_t spectrum of electron and muon sample, respectively. In these figures, plot and histogram indicate the experimental data and the fit result of each contribution (c, b, $b \to c, u, \tau$ processes and background).

The observed cross-section σ_q^{obs} can be related to the effective Born cross-sections σ_q by the following equation,

$$\sigma_q = \frac{\sigma_q^{\mathrm{obs}}}{(1+\delta)\cdot\epsilon_H} \tag{6.4}$$

where ϵ_H is the efficiency for hadronic event selection and δ is the radiative correction factor which is evaluated by the program ZFITTER [63]. These values are summarized in Table 6.2.

		c quark	b quark
Efficiency	ϵ_H	0.716	0.809
Radiative correction	$1+\delta$	1.291	1.085
	$(1+\delta)\cdot\epsilon_H$	0.924	0.878

Table 6.2: Efficiency of hadronic event selection (ε_H) and radiative correction factor (δ).

By using this relation, we finally obtain the effective Born cross-sections of c and b quark pair production as follows.

	Effective Born cross-section [pb]		
	electron sample	muon sample	combined fit result
σ_c	$45.8 \pm 4.4 \pm 4.5$	$31.4 \pm 4.7 \pm 7.1$	$45.3 \pm 3.2 \pm 3.8$
σ_b	$20.0 \pm 1.5 \pm 1.3$	$19.3 \pm 1.9 \pm 1.1$	$19.3 \pm 1.1 \pm 0.8$

Table 6.3: Measured values of effective Born cross-sections.

The first error is statistical and the second error is systematical due to the uncertainties of the fragmentation parameters, branching ratios and normalization factors. Here normalization factors are integrated luminosity, efficiency of hadronic event selection and normalazation factor of background. We assume that overall uncertainty of integrated luminosity and efficiency of hadronic event selection is 5%. Table 6.4 lists contribution of each systematic error source.

Error source	c quark	b quark
Fragmentation	0.64	0.15
Branching ratio	1.63	0.46
Normalization	3.39	0.77
Total	3.84	0.84

Table 6.4: Source of systematic errors.

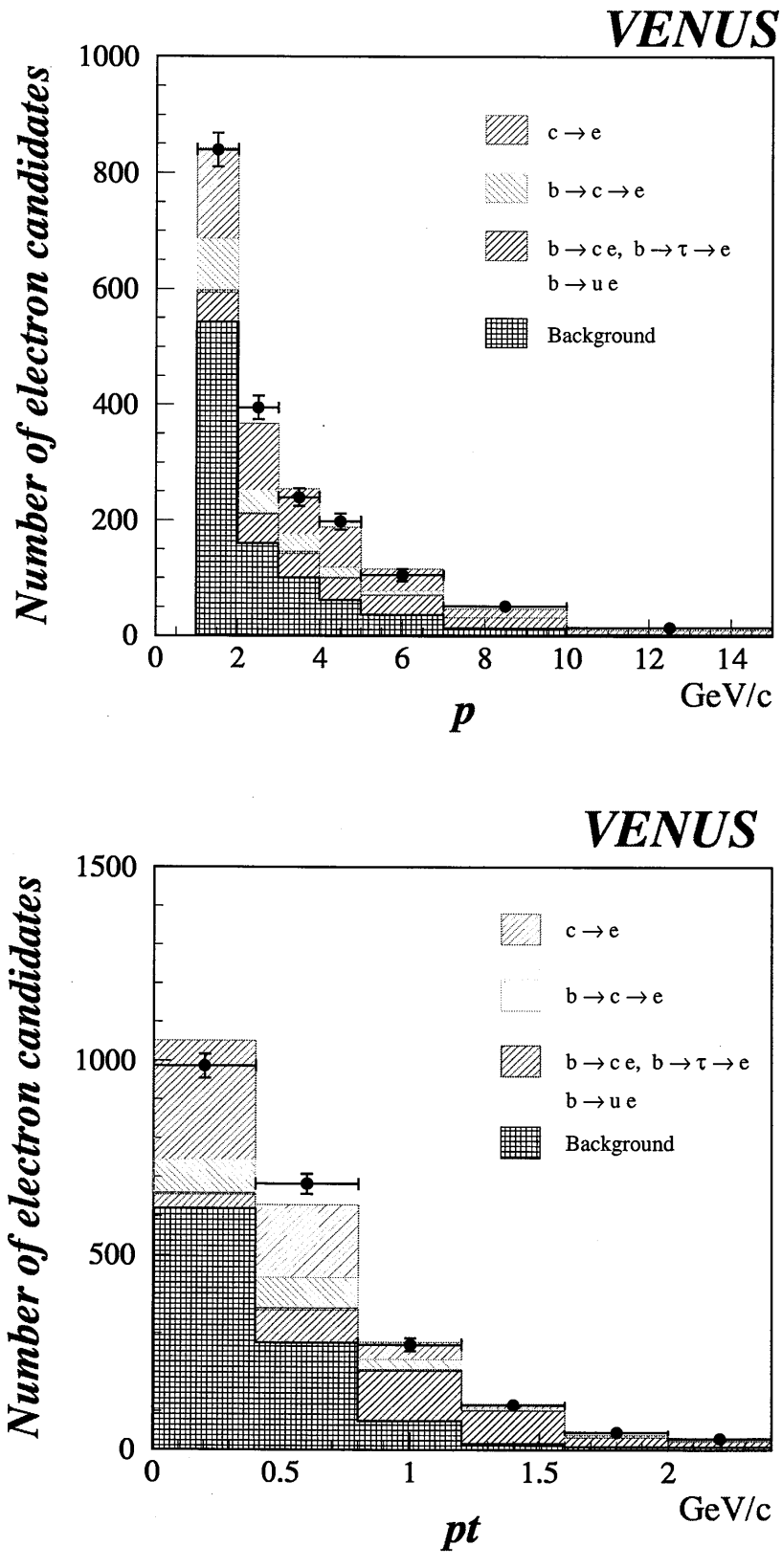

Figure 6.1: Momentum p and transverse momentum p_t spectrum of electron candidates.

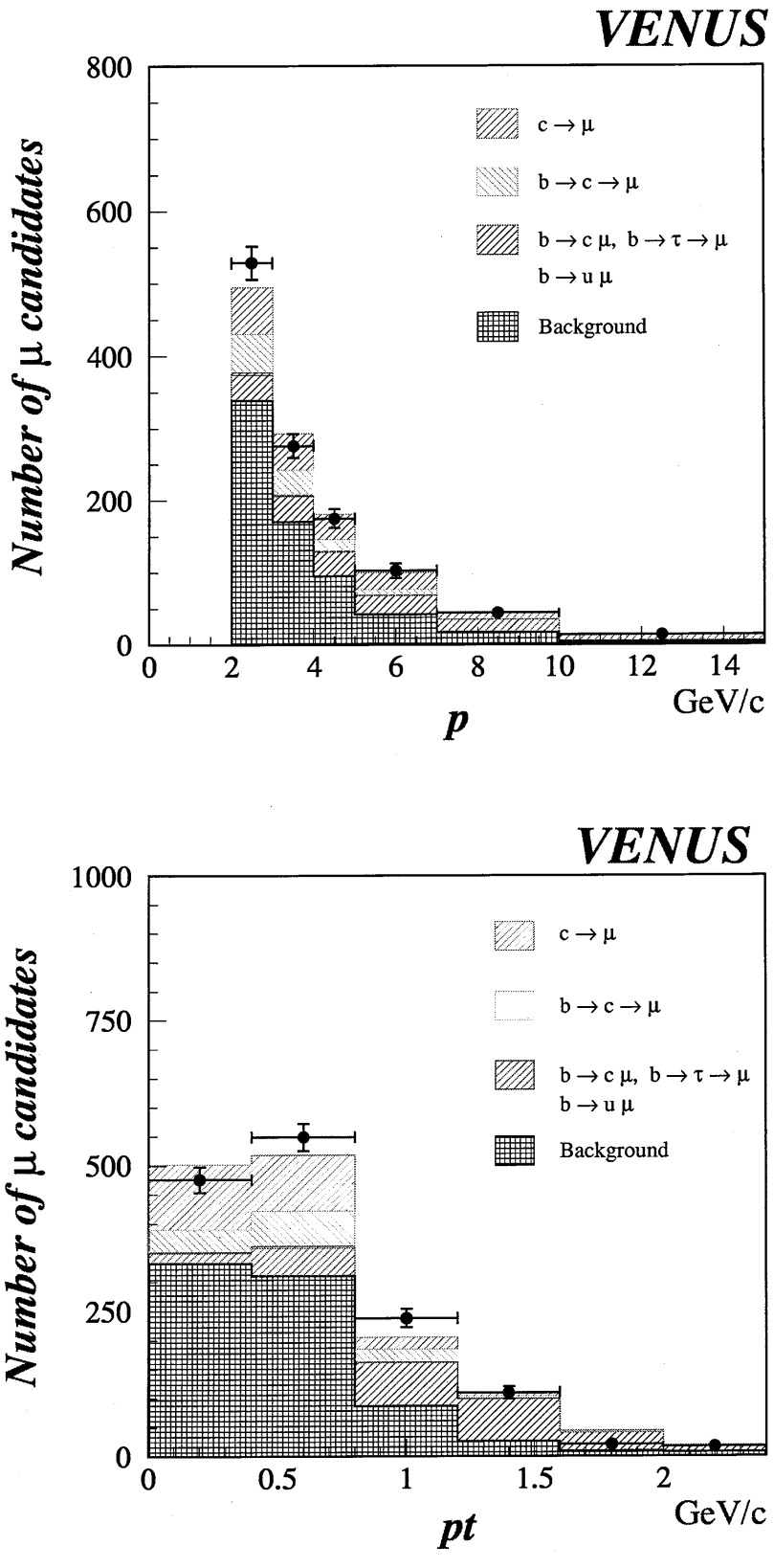

Figure 6.2: Momentum spectrum p and transverse momentum p_t of muon candidates.

6.2 Forward-backward asymmetry of heavy quarks

In order to measure the forward-backward asymmetry in the process $e^+e^- \to c\bar{c}$ and $b\bar{b}$, we define a production angle of quark (not anti-quark) by introducing a variable z as $z = -Q\cos\theta_{\rm thrust} = -Q\ \hat{t}\cdot\hat{e}$, where Q is the charge of the prompt lepton. The direction of $\hat{t}$ is determined by the thrust axis and the hemisphere containing the lepton track and $\hat{e}$ is the unit vector in the e^- beam direction. The uncertainty in the determination of the quark direction is found to be about 6° according to Monte Carlo simulation. We divide the lepton candidates into two categories: one for lower p_t ($p_t < 0.8$ GeV/c) and the other for higher p_t ($p_t > 0.8$ GeV/c). The sample with lower (higher) p_t is expected to be enriched with prompt leptons from c decays (b decays).

We determine $A_{\rm FB}$ of the c and b quarks to fit these angular distributions by using the following expression,

$$\begin{aligned} N^j_{data}(z) &= N^j_{cp}\ (1+z^2-\frac{8}{3}A^c_{\rm FB}\ z)\ \eta^j(z) \\ &+ (N^j_{bp}+N^j_{b\tau}+N^j_{bu})\ (1+z^2+\frac{3}{8}A^b_{\rm FB}\ z)\ \eta^j(z) \\ &+ N^j_{bc}\ (1+z^2-\frac{3}{8}\kappa\ A^b_{\rm FB}\ z)\ \eta^j(z) \\ &+ N^j_{bg}(z) \qquad\qquad (j=1,2) \end{aligned} \tag{6.5}$$

where the index j represents either the lower or higher p_t sample and N^j_i is the number of prompt leptons ($i = cp, bp, bc, bu, b\tau$) corresponding to each term of Eq. 6.1. $N^j_{bg}(z)$ is the angular distributions for the backgrounds, which is estimated by a Monte Carlo simulation beforehand. Their normalization factors are constrained to the total number N^j_{bg} which is described in the previous chapters.

N^j_{bc} includes the contribution of leptons both from $b \to c \to l^+$ and $b \to c\bar{c}s, \bar{c} \to l^-$. The wrong charge assignment from these contributions is taken into account by the factor $\kappa = (1-\alpha)/(1+\alpha) = 0.72$.

The correction factor due to the detector acceptance $\eta^j(z)$ is obtained from a Monte Carlo simulation as shown in Figs. 6.3 and 6.4. It is taken to be symmetric in z; $\eta^j(-z) = \eta^j(z)$ and is normalized as

$$\int_{-1}^{1}(1+z^2)\ \eta^j(z)\ dz = 1.$$

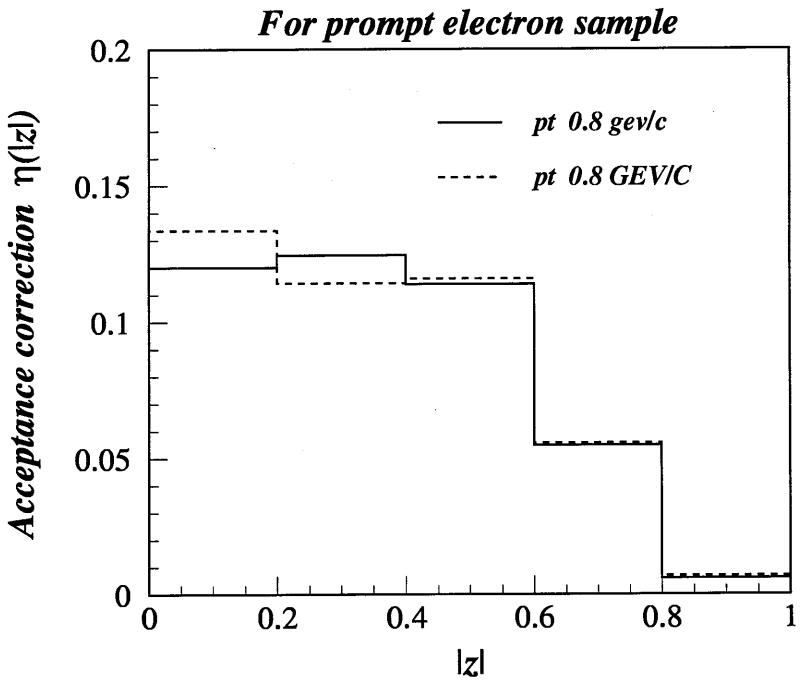

Figure 6.3: Acceptance correction factor for prompt electron sample.

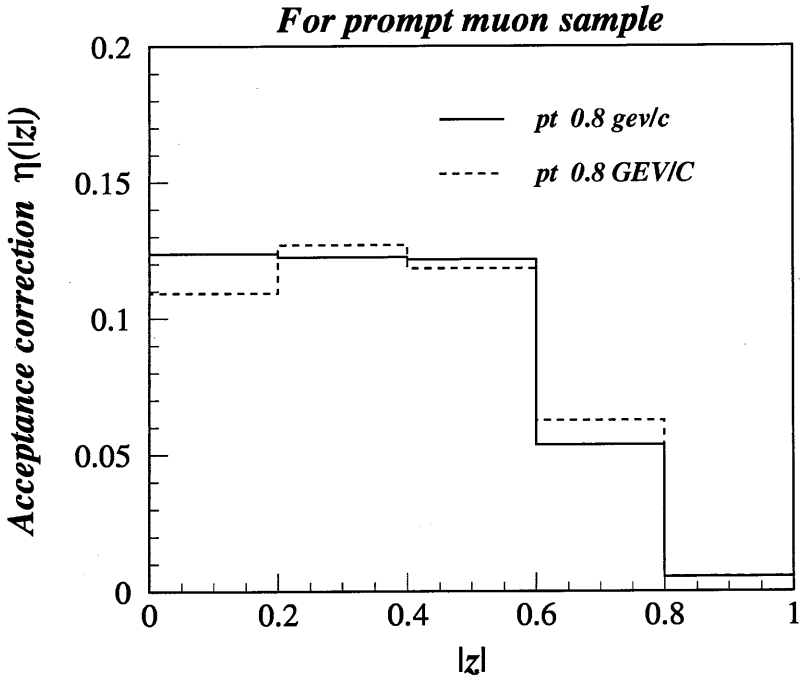

Figure 6.4: Acceptance correction factor for prompt muon sample.

We fit the angular distribution of z with Eq. 6.5. using $A_{\rm FB}^c$ and $A_{\rm FB}^b$ as free parameters. The z distributions for lower and higher p_t regions are shown in Fig. 6.5 and 6.6 for electron and muon samples, respectively. The best fits are also shown in histograms.

In order to obtain the forward-backward asymmetry at the lowest order, photon and gluon radiation effects must be taken into account. Their combined effects are found to decrease the absolute values for $A_{\rm FB}^c$ and $A_{\rm FB}^b$ by 0.05 and 0.04, respectively, while the QCD correction alone is estimated to be 0.02 for both $A_{\rm FB}^c$ and $A_{\rm FB}^b$. Finally, we obtained $A_{\rm FB}$ for the c and b quarks at the lowest order as follows.

	Forward-backward asymmetry		
	electron sample	muon sample	combined result
$A_{\rm FB}^c$	$-0.48 \pm 0.09 \pm 0.03$	$-0.48 \pm 0.12 \pm 0.03$	$-0.47 \pm 0.07 \pm 0.03$
$A_{\rm FB}^b$	$-0.34 \pm 0.13 \pm 0.01$	$-0.45 \pm 0.15 \pm 0.01$	$-0.38 \pm 0.10 \pm 0.01$

Table 6.5: Measured values of forward-backward asymmetry.

Similar to cross-section measurements, contribution of each systematic error are listed in Table 6.6.

Error source	c quark	b quark
Fragmentation	0.005	0.002
Branching ratio	0.016	0.008
Normalization	0.014	0.010
Total	0.027	0.012

Table 6.6: Source of systematic errors.

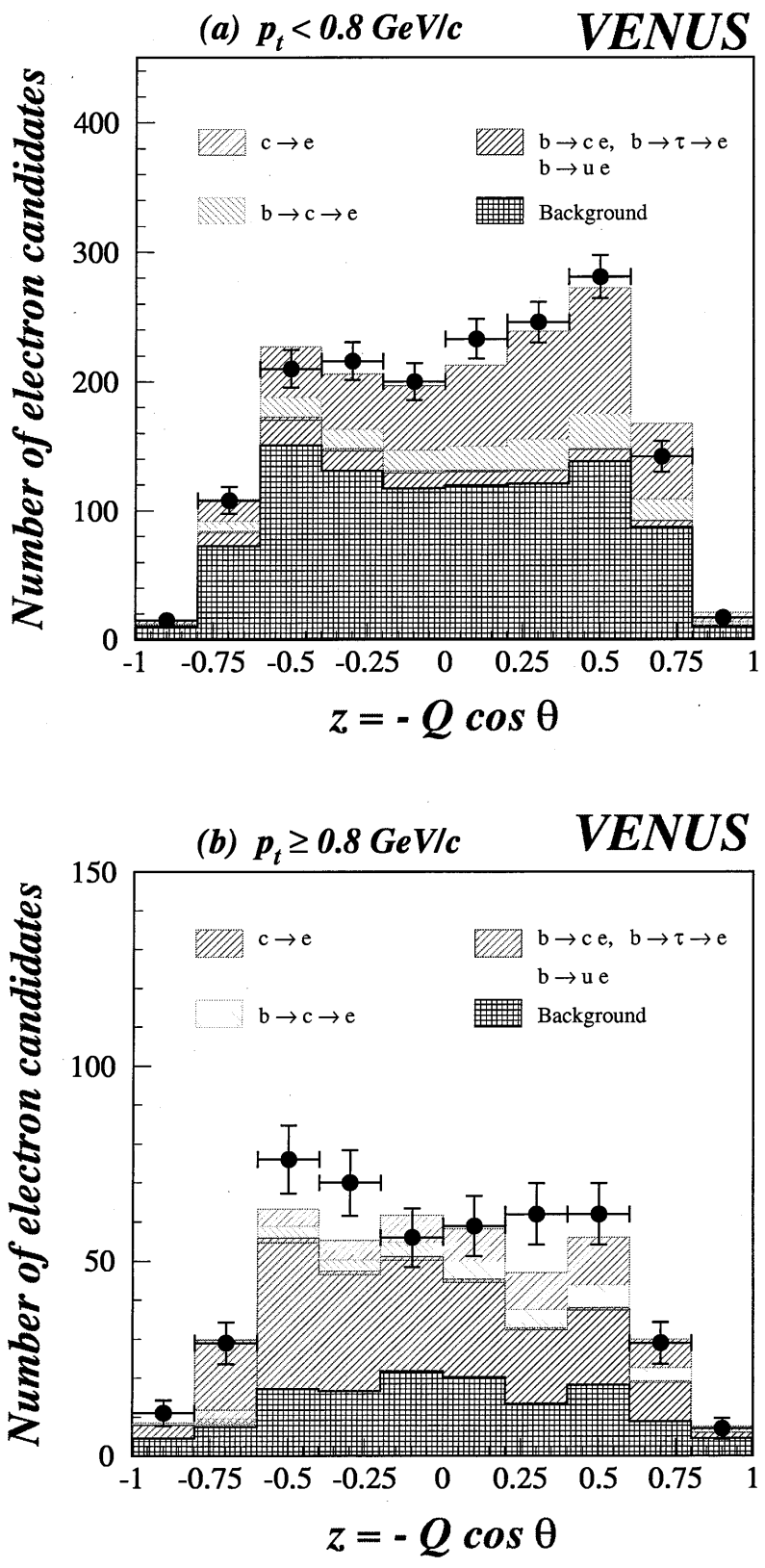

Figure 6.5: z distributions of electron candidates

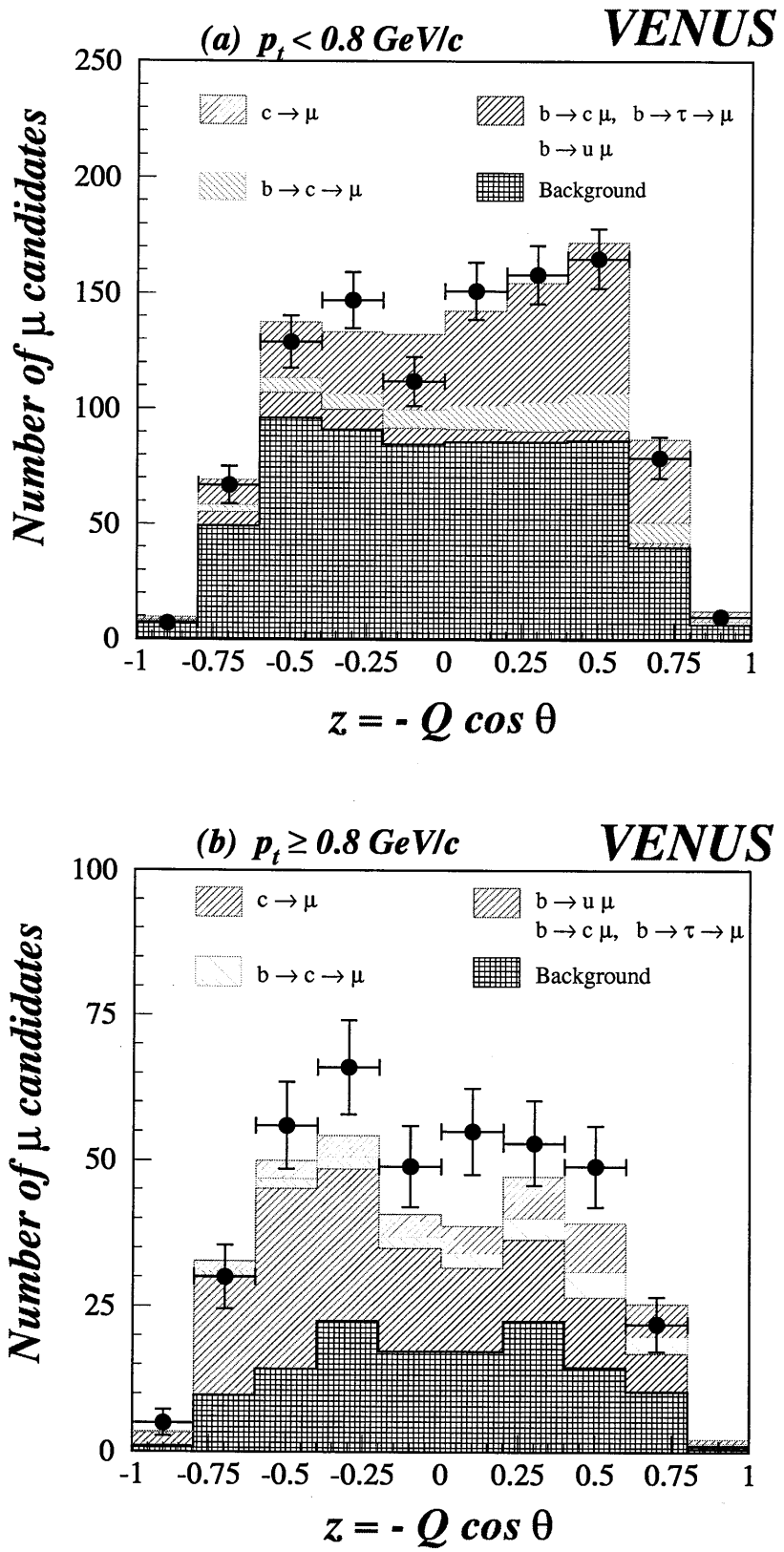

Figure 6.6: z distributions of muon candidates

Chapter 7

Discussion

We have derived values of the cross-section and forward-backward asymmetry of heavy quark pair production by using prompt leptons in e^+e^- annihilation at $\sqrt{s} = 58$ GeV. In this chapter these measured values are used to investigate a possible contribution from contact interaction.

7.1 Cross-section

From p and p_t spectrum of prompt lepton candidates, we obtain the effective Born cross-sections of heavy quark pair production to be

$$\begin{aligned} \sigma_c &= 45.3 \pm 3.2 \pm 3.8 \text{ pb} \\ \sigma_b &= 19.3 \pm 1.1 \pm 0.8 \text{ pb} . \end{aligned}$$

Both σ_c and σ_b obtained here are consistent with the Standard Model prediction, σ_c^{SM}=45.5 pb and σ_b^{SM}=16.8 pb, where the Standard Model parameters are fixed to the following values [58]; $\sin^2\theta_W = 0.228$, $M_Z = 91.175$ GeV, and $\alpha_s(M_Z) = 0.120$.

7.2 Forward-backward asymmetry

From fits to the angular distribution z of the events containing prompt leptons, the forward-backward asymmetries of the heavy quarks are measured to be

$$\begin{aligned} A_{FB}^{c} &= -0.47 \pm 0.07 \pm 0.03 \\ A_{FB}^{b} &= -0.38 \pm 0.10 \pm 0.01 \ . \end{aligned}$$

To compare the Standard Model prediction with the experimental result, the effect of B^0–$\overline{B^0}$ mixing must be included. Because of the mixing effect, a produced B^0 meson decays as $\overline{B^0}$ through the box diagrams shown in Fig. 7.1.

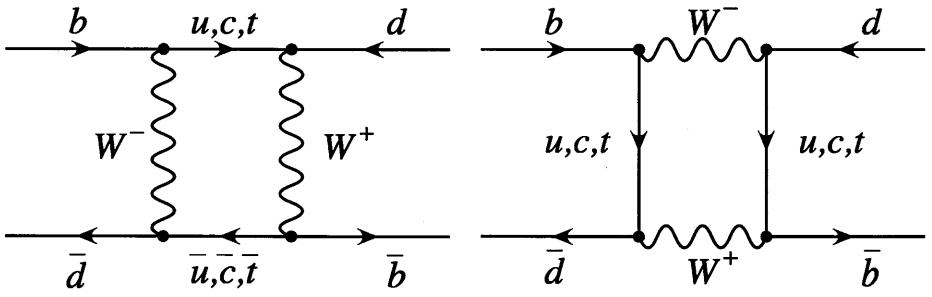

Figure 7.1: Box diagram of B^0–$\overline{B^0}$ mixing.

The mixing, therefore, dilutes the forward-backward asymmetry of the b quarks. Mixing effect in c quarks is known to be negligible. Then the b quark asymmetry $A_{\rm FB}^{b}$ to be observed is related to that $A_{\rm FB}^{b\,\rm Born}$ with no-mixing as follows

$$A_{\rm FB}^{b} = (1 - 2\chi)\ A_{\rm FB}^{b\,\rm Born} \ , \tag{7.1}$$

where χ is the average mixing probability of B^0 meson. When we substitute the value of $\chi = 0.1246 \pm 0.0073$ [62], the predicted value of $A_{\rm FB}^{b}$ is -0.44.

Our results for $A_{\rm FB}^{c}$ and $A_{\rm FB}^{b}$ are consistent with the Standard Model prediction of -0.49 and -0.44, respectively, taking the mixing effect into account. Figures 7.2 and 7.3 plot the present results together with those from other previous experiments. The Standard Model prediction is also drawn there.

Our result gives the most precise measurement of $A_{\rm FB}^{c}$ at $\sqrt{s} = 58$ GeV. By using large samples of electron and muon candidates we have reduced the statistical error by factor of two with respect to the previous VENUS analysis using prompt electron or the previous TOPAZ analysis combined with D^* and prompt electron tagging. We have also reduced the systematic error by well understanding misidentification and conversion electron rejection probability with several control samples and Monte Carlo simulation. For $A_{\rm FB}^{b}$ AMY's result is the most precise measurement. They categorized prompt muon inclusive events into $b\bar{b}$ and non-$b\bar{b}$ events by

using neural networks based on event-by-event characteristics. Therefore they can subtract c quark decays and backgrounds and reduce statistical error. But there are some arguments on the systematic error of the neural networks.

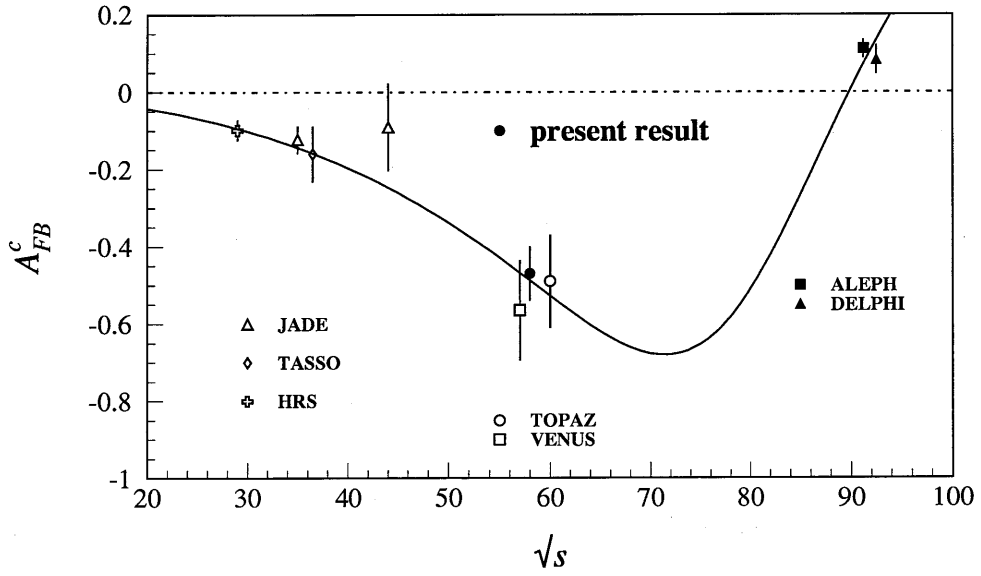

Figure 7.2: Forward-backward asymmetry of c quarks measured by various experiments as a function of the center of mass energy. Solid line indicates that of the Standard Model prediction.

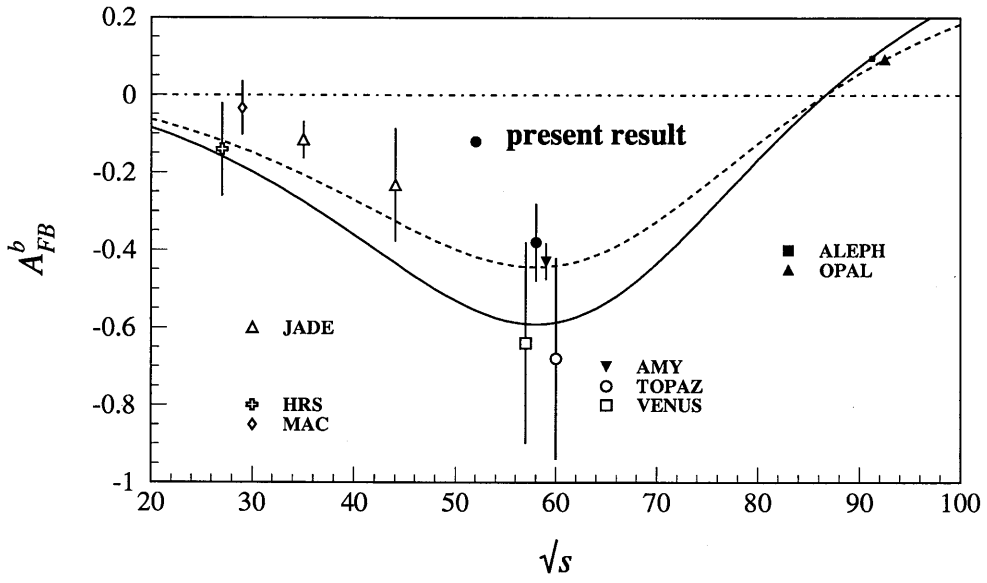

Figure 7.3: Forward-backward asymmetry of b quarks measured by various experiments as a function of the center of mass energy. Solid and dashed line indicate that of the Standard Model prediction without and with B^0–$\overline{B^0}$ mixing effect, where we assume that $\chi = 0.1246$.

7.3 Compositeness of heavy quarks

Since both of the measured cross-section and the forward-backward asymmetry of the heavy quarks are consistent with the Standard Model prediction, we will set the limit for new physics. If quarks are made of constituents, new interactions among quarks appear at the binding energy scale of those constituents. At energies much below the compositeness scale Λ, these interactions are suppressed by inverse powers of Λ. The dominant effect should come from the contact interactions with four fermions. The effective Lagrangian of the contact interaction is usually expressed as

$$\mathcal{L}^{\text{contact}} = \frac{g^2}{\Lambda^2} \sum_{i,j=L,R} \eta_{ij} \ \bar{e}_i \gamma^\mu e_j \ \bar{q}_i \gamma_\mu q_j \tag{7.2}$$

for $e^+e^- \to q\bar{q}$ process.

By convention, the unknown coupling constant g is set to $g^2/4\pi = 1$ and the magnitude of the coefficients η is set to be unity. A number of models (choice of η_{ij} parameters) are considered. They are summarized in Table 7.1. The L, R, V and A denote the left-handed, right-handed, vector and axial vector couplings, respectively. The signs ($\pm$) of the η_{ij} indicate positive or negative interference with the Standard Model amplitude.

Model	η_{LL}	η_{RR}	η_{LR}
$LL^{\pm}$	± 1	0	0
$RR^{\pm}$	0	± 1	0
$AA^{\pm}$	± 1	± 1	± 1
$VV^{\pm}$	± 1	± 1	∓ 1

Table 7.1: Different models of the four fermions contact interaction

In the presence of the contact interaction, the differential cross section for $e^+e^- \rightarrow q\bar{q}$ can be written in the lowest order as

$$\begin{aligned} \frac{4s}{3\pi^2\alpha^2}\frac{d\sigma}{d\cos\theta} &= [\ |\mathcal{A}^{eq}_{LR}(s)|^2 + |\mathcal{A}^{eq}_{RL}(s)|^2\ ]\left(\frac{t}{s}\right)^2 \\ &+ [\ |\mathcal{A}^{eq}_{LL}(s)|^2 + |\mathcal{A}^{eq}_{RR}(s)|^2\ ]\left(\frac{u}{s}\right)^2 \end{aligned} \tag{7.3}$$

with $t = -\frac{1}{2}s(1-\cos\theta)$ and $u = -\frac{1}{2}s(1+\cos\theta)$. The helicity amplitudes $\mathcal{A}(i,j=L,R)$ are

$$\mathcal{A}^{eq}_{i,j=L,R} = Q_e Q_q + g^e_i g^q_j\ \chi(s) + \frac{\eta_{ij}}{\alpha}\frac{s}{\Lambda^2} \tag{7.4}$$

The third term is the effect of contact interaction. Here α is the electromagnetic coupling constant. The left- and right-handed couplings, g^q_L and g^q_R, of the quark q to the Z^0 boson are given by

$$g^q_L = \frac{e}{\sin\theta_W\cos\theta_W}(I_3 - Q_q\sin^2\theta_W) \tag{7.5}$$

$$g^q_R = \frac{e}{\sin\theta_W\cos\theta_W}(-Q_q\sin^2\theta_W) \tag{7.6}$$

where e is the electron charge, Q_q is the electric charge of the quark q in units of $|e|$, I_3 is the third component of the weak isospin and θ_W is the electroweak mixing angle.

The lower limit at 95% CL[1] is defined as the Λ value which give the cross-section or forward-backward asymmetry separated by 1.64σ from the measurement. For example, the expected forward-backward asymmetry of c quark is shown as a function of the compositeness scale Λ in Fig. 7.4. In this figure dashed and dotted lines indicate the our measured value of c quark asymmetry and the $\pm 1.64\sigma$ deviated values, respectively.

[1]CL denotes confidence level.

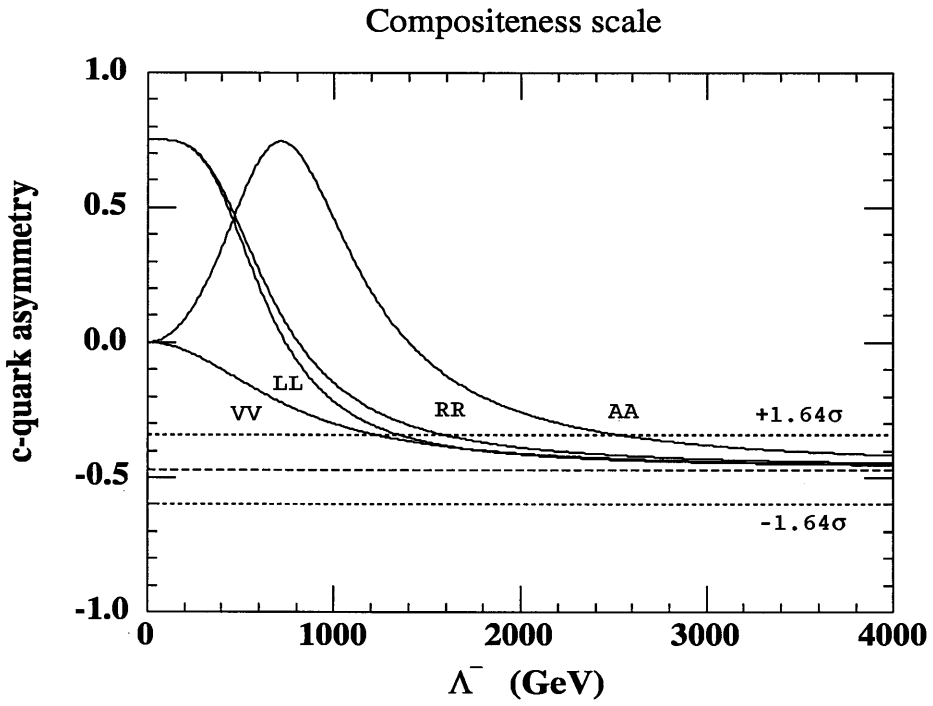

Figure 7.4: Forward-backward asymmetry of c quarks is plotted against the compositeness scale. Dashed line show the 95% CL (1.64σ) limits calculated from our measurement.

We note that Eq. 7.3 uses only the lowest order amplitudes (Born term). Therefore conversion of effective Born cross-section to Born cross-section is nessesary. We use the following values as Born cross-sections.

$$\begin{aligned}
\sigma_c^{\mathrm{Born}} &= 37.0 \pm 4.3 \quad \mathrm{pb} \\
\sigma_b^{\mathrm{Born}} &= 18.9 \pm 1.5 \quad \mathrm{pb} \\
A_{\mathrm{FB}}^{c\ \mathrm{Born}} &= -0.47 \pm 0.08 \\
A_{\mathrm{FB}}^{b\ \mathrm{Born}} &= -0.51 \pm 0.10
\end{aligned}$$

As mentioned in the previous section, $A_{\mathrm{FB}}^{b\ \mathrm{Born}}$ is corrected with the B^0–$\overline{B^0}$ mixing effects. The errors are quadratic sum of statistical and systematic errors. Using the above values, we can set the lower limits on the compositeness scale Λ as values at crossing points with the 1.64σ band allowed by data.

Our results are summarized in Tables 7.2 and 7.3. A typical lower limit on compositeness scale of 2 TeV corresponds to 10^{-4} fm (10^{-19} m). These are as strict as the previous PETRA results [64]. For some models our results set new lower limits on the compositeness scale of Λ. This result is unique in a sense of specifying a quark flavour and using the total cross-section. Many experiments have set the lower limits on quarks (not specify quark flavour) and electron (positron) compositeness by using the total cross-section and forward-backward asymmetry. On heavy (c and b) quarks and electron compositeness only PETRA experiments set by using the

forward-backward asymmetry. These are the first and most stringent results on heavy quarks and electron compositeness by using total cross-section and forward-backward asymmetry.

	Lower limits of Λ (TeV)							
	LL		*RR*		*VV*		*AA*	
	+	−	+	−	+	−	+	−
VENUS	0.7	1.3	1.1	1.5	2.0	2.5	2.0	2.1
PETRA	1.1	1.6	1.1	1.7	0.7	0.7	2.1	3.2

Table 7.2: 95% CL lower limit on the compositeness scale of the *eecc* contact interaction. Previous PETRA result used measurements of the forward-backward asymmetry at the JADE, TASSO and HRS experiments.

	Lower limits of Λ (TeV)							
	LL		*RR*		*VV*		*AA*	
	+	−	+	−	+	−	+	−
VENUS	1.1	1.6	2.0	2.2	3.9	4.3	3.4	3.0
PETRA	1.2	0.5	1.4	0.8	0.7	0.9	2.4	1.4

Table 7.3: 95% CL lower limit on the compositeness scale of the *eebb* contact interaction. Previous PETRA result used measurements of the forward-backward asymmetry at the JADE experiments.

Chapter 8

Conclusion

We have selected prompt leptons produced in hadronic events to investigate heavy quark pair production in e^+e^- annihilation using a full data set of the VENUS experiments. Muon identification has been improved by introducing local track reconstruction algorithm in the muon chambers and imposing connectivity between a CDC track and the local muon track. The efficiency for muon is about 70% while that for hadron is 0.5% at p >2 GeV/c. In the electron identification, the estimation of the gamma conversion has become much more reliable by using the information of the vertex chamber. We have reduced its uncertainty to less than 10%. Thus, we have obtained the best data on the heavy quark production at TRISTAN energy, especially for charm quark.

From fits to the lepton p and p_t spectra, the effective Born cross-sections of heavy quark pair production are measured to be

$$\begin{aligned} \sigma_c &= 45.3 \pm 3.2 \text{ (stat.)} \pm 3.8 \text{ (syst.)} \text{ pb} \\ \sigma_b &= 19.3 \pm 1.1 \text{ (stat.)} \pm 0.8 \text{ (syst.)} \text{ pb.} \end{aligned}$$

And from fits to the angular distribution of the thrust axis of the events containing prompt leptons, the forward-backward asymmetries of heavy quark pair production are measured to be

$$\begin{aligned} A_{FB}^c &= -0.47 \pm 0.07 \text{ (stat.)} \pm 0.03 \text{ (syst.)} \\ A_{FB}^b &= -0.38 \pm 0.10 \text{ (stat.)} \pm 0.01 \text{ (syst.).} \end{aligned}$$

Both the cross-section and the forward-backward asymmetry of the b and c quarks measured here are consistent with the Standard Model prediction.

The deviation from the Standard Model prediction is tested in terms of the compositeness scale Λ. Typically we have obtained $\Lambda_{eecc}^{VV+} > 2.0$ TeV and $\Lambda_{eebb}^{VV+} > 3.9$ TeV at 95% CL as new limits on the possible existence of the compositeness of quarks.

Appendix A

Events samples

To study the capability of lepton identification, we use several controlled samples of muon, electron and pion. In this chapter, we describe how to select the above particle samples.

A.1 Electron samples

In the e^+e^- collision experiment, large amount of electron (positron) can be observed in their elastic scattering ($e^+e^- \to e^+e^-$), which is called "Bhabha scattering" and is contributed by two diagrams as shown in Fig. A.1. In elastic scattering, scattered electron (positron) should has beam energy ($E_{\rm beam}$=29 GeV). But due to the effect of initial-state radiation some scattered electron (positron) has relatively low momentum. We use these radiative Bhabha events as electron samples.

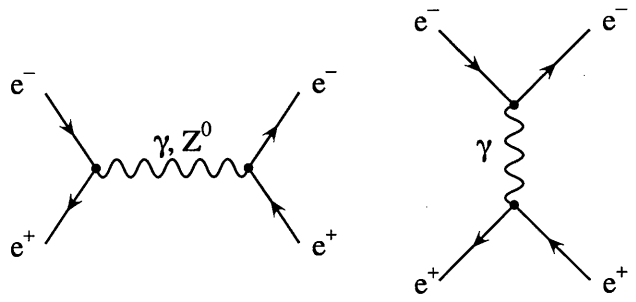

Figure A.1: Feynman diagram of $e^+e^- \to e^+e^-$ process.

A.1.1 Bhabha events ($e^+e^- \to e^+e^-(\gamma)$)

To select Bhabha events, we require the following conditions: (1). There is only two CDC track. (2). Total energy on LG is greater than 5 GeV. This selection is effective to reduce muon pair production events ($e^+e^- \to \mu^+\mu^-$), because muon do not induce an electro-magnetic shower in the calorimeter.

A.1.2 Single track events

As a low momentum electron sample, we use events in which either an electron or positron and radiated photons are observed and the other electron goes by the beam pipe as shown in Fig. A.2.

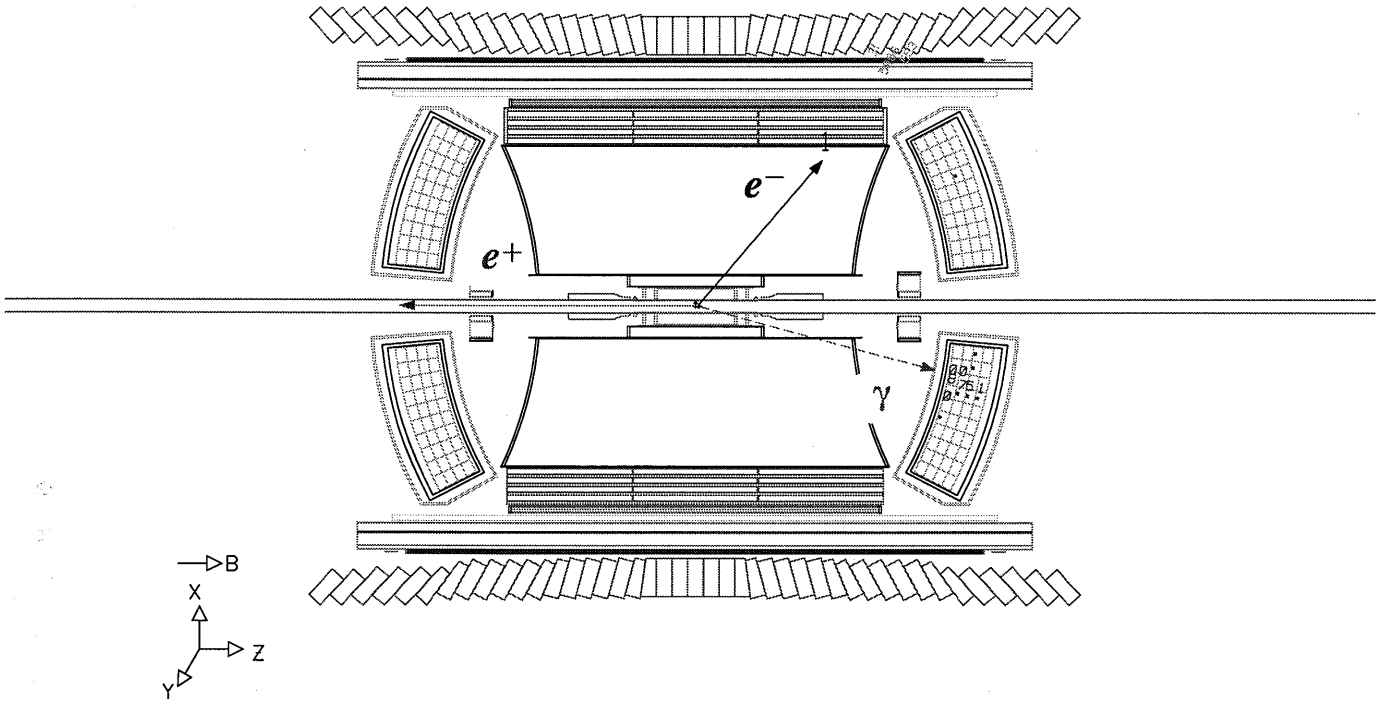

Figure A.2: A typical single track event.

Since the condition of track trigger needs at least two tracks, most of single track events are triggered by requiring LG energy deposit (as mentioned in 2.3.1; total deposited energy in LG is greater than 3 GeV.). Therefor single tracks of muon or hadrons are not triggered and only radiative Bhabha events are triggered as single track samples. Single track must be well reconstructed[1] by CDC. We have obtained 27034 single track events as an electron sample.

Both of single track and Bhabha event samples have clear peaks of $\mu \sim 0$ ans their shower shapes are consistent with electromagnetic showers as shown in Fig. A.3.

[1] $N_{axial\ wire\ hits} \geq 8$, $N_{slant\ wire\ hits} \geq 4$, $|R_{min}| < 2$ cm, $|Z_{min}| < 20$ cm, $p_{xy} > 0.2$ GeV/c and $|\cos\theta| < 0.8$

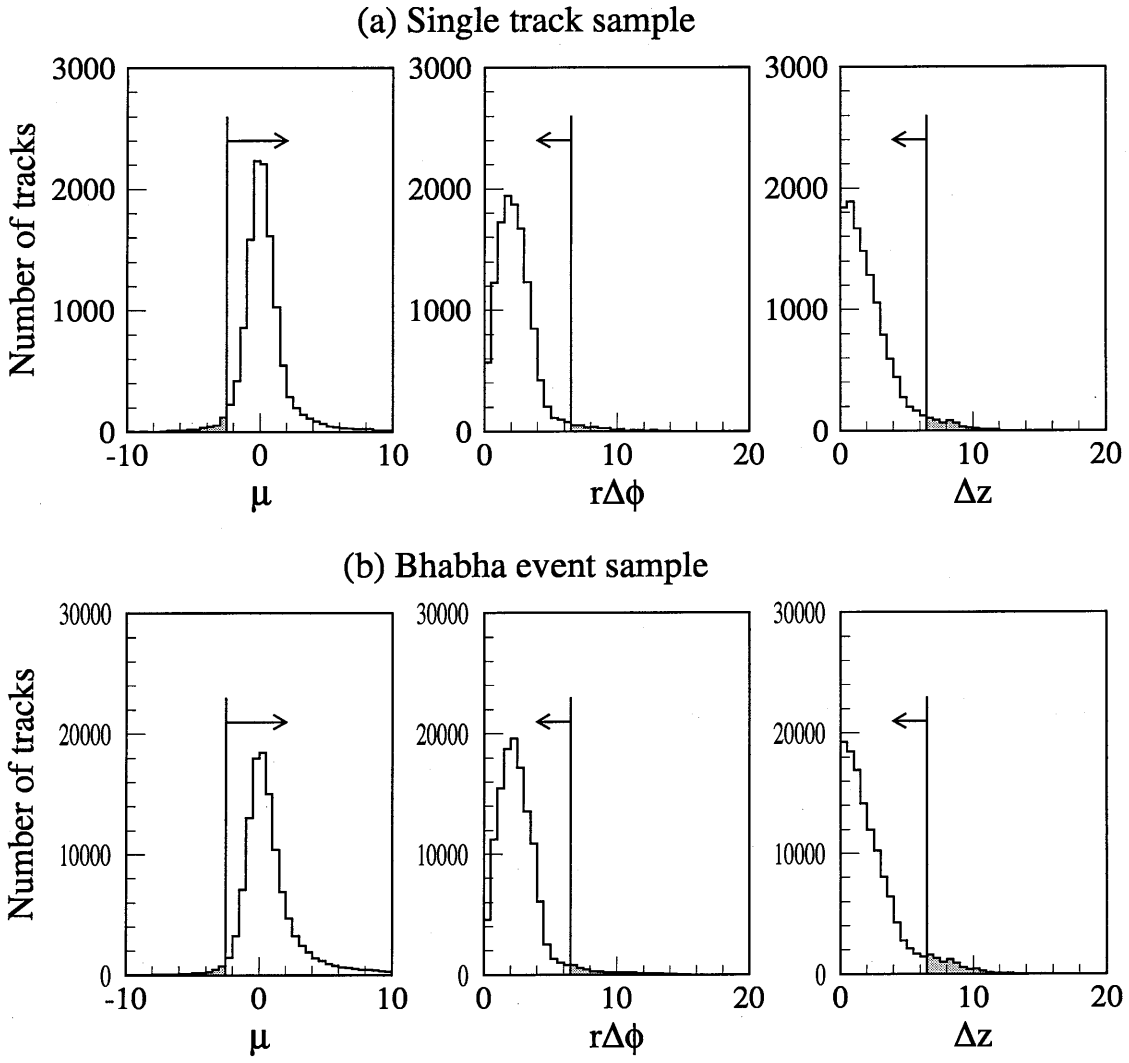

Figure A.3: Distributions of μ, $r\Delta\phi$ and Δz of (a). single track sample and (b). Bhabha event sample.

A.2 Muon samples

As muon samples, we use radiative muon pair production via single γ or Z^0 exchange ($e^+e^- \to \mu^+\mu^-$) and muon pair production via two-photon process ($e^+e^- \to e^+e^-\mu^+\mu^-$).

A.2.1 $e^+e^- \to \mu^+\mu^-\gamma$ events

We use radiative muon pair production events as a muon sample. Because we need a wide momentum range of muon sample, we select only radiative events similar to that of electron sample.

1. $N_{\rm good} = 2$
   There are only two well reconstructed tracks.

2. (The number of neutral cluster) ≥ 1
   A neutral cluster is defined as that of E >1.0 GeV and without the corresponding CDC tracks.

3. $E_{\rm vis} \geq 0.5\sqrt{s}$
   To reduce two-photon processes, we require a large visible energy.

4. p >2.0 GeV/c
   Our interest is this momentum region.

5. E_{LG} <1.5 GeV
   To reduce electron, we require a small cluster energy corresponding to the CDC track.

6. $\mid \varphi_{12} + \varphi_{23} + \varphi_{31} - 360.0 \mid < 1.0°$
   Two tracks and a neutral cluster must be in a plane.

After the above selection, we have obtained 2930 events as a muon sample.

A.2.2 $e^+e^- \to e^+e^-\mu^+\mu^-$ events

As a low momentum sample of muon, we use muon pair production in two-photon process ($e^+e^- \to e^+e^-\mu^+\mu^-$) as shown in Fig. A.4. We select only those reactions in which both of scattered electron and positron go to the beam pipe. Then a signal is the existence of only two muon tracks with considerably low total energy.

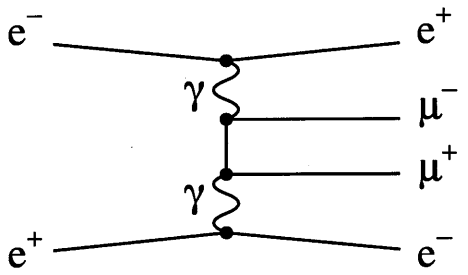

Figure A.4: Feynman diagram of $e^+e^- \to e^+e^-\mu^+\mu^-$ process.

This muon sample is selected by the following requirements,

1. $N_{\rm good} = 2$, $\Sigma\ Q_i = 0$, $p \geq 1.5$ GeV/c
   There are only two well reconstructed[2] tracks of which total charge is neutral. Both momenta are greater than 1.5 GeV/c.

2. $E_{\rm vis} \leq 0.5\ E_{\rm beam}$
   $E_{\rm vis}$ is a visible energy as described in Chap. 3.2.1. In the two-photon process produced muons have considerably lower momentum than those produced via single γ or Z^0 exchange. Namely visible energy tends to be small.

3. $|\Sigma\ \overrightarrow{p_{xy}}| \leq 0.4$ GeV/c
   Since two-photon system is boosted along beam (z) direction, we cannot require a momentum balance along the z direction. To reduce events in which $e^{\pm}$ beams interact with the beam pipe or gas in it, we require a momentum balance in the x-y plane.

4. $|\Delta{\rm TOF}| < 5$ nsec
   To reject muon of cosmic ray events, time-of-flight of both particles should consistent with beam crossing time.

5. $E_{\rm LG} < 1.0$ GeV
   $E_{\rm LG}$ is a cluster energy corresponding to CDC track. This selection is effective to reject electrons with $p > 1.5$ GeV/c, namely to reject $e^+e^- \to e^+e^-e^+e^-$ events.

After this selection, we have obtained 6756 events as a muon sample.

[2] $N_{\rm axial\ wire\ hits} \geq 10$, $N_{\rm slant\ wire\ hits} \geq 4$, $|R_{\rm min}| < 2$ cm, $|Z_{\rm min}| < 15$ cm and $|\cos\theta| < 0.7$

Background estimation

Most of this muon sample events have the center-of-mass energies of two-photon system (W) greater than 3.0 GeV/c^2 as shown in Fig. A.5, because we require that muon momentum is greater than 1.5 GeV/c.

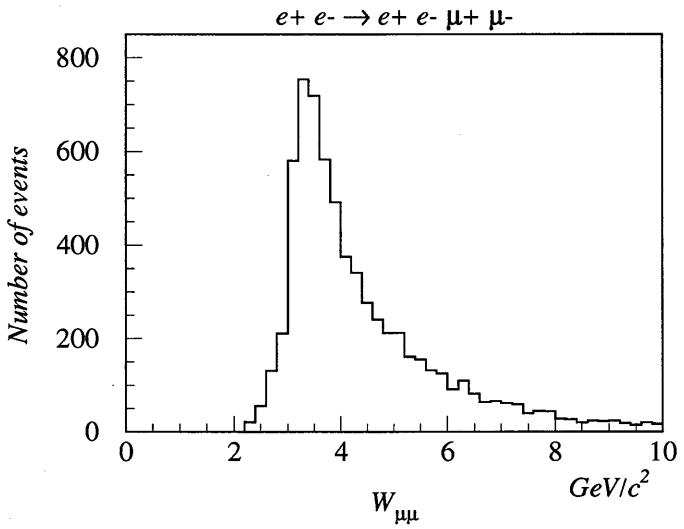

Figure A.5: Invariant mass distribution of this muon samples. It corresponds to the center-of-mass energy of two-photon system; $W_{\mu\mu} = W$

To estimate the contamination of $e^+e^- \to e^+e^-\pi^+\pi^-/e^+e^-K^+K^-$ events, we calculate cross-section of these events in the region of $W > 3.0$ GeV/c^2. Cross-section in two-photon process is presented by the following formula [58],

$$\sigma_{e^+e^-\to e^+e^-X}(s) = \frac{\alpha^2}{\pi^2}\int_{0.0027}^{1}\frac{dz}{z}\left[f(z)\left(ln\frac{(-q^2)_{\max}}{m_e^2 z}-1\right)^2-\frac{1}{3}\left(ln\frac{1}{z}\right)^3\right]\sigma_{\gamma\gamma\to X}(zs) \quad . \quad \text{(A.1)}$$

Here $f(z)$ are formulated with z as,

$$f(z) = \left(1+\frac{1}{2}z\right)^2 ln\left(\frac{1}{z}\right)-\frac{1}{2}(1-z)(3+z), \quad \text{(A.2)}$$

$$z = W^2/s \quad . \quad \text{(A.3)}$$

The quantity $(-q^2)_{\max}$ depends on properties of the production system X, in particular, $(-q^2)_{\max} \sim W^2$ for lepton pair production ($X = \mu^+\mu^-$) and $(-q^2)_{\max} \sim m_\rho^2$ for hadron ($X = \pi\pi$ or KK).

We use measured cross-section of the $\gamma\gamma \to \pi\pi, KK$ process at CLEO experiment [66] as listed in Table A.1. For the $\gamma\gamma \to \mu\mu$ process, the lowest order QED calculation is used. It is formulated with W as

$$\sigma_{\gamma\gamma\to\mu\mu}(W; |\cos\theta^*| < 0.6) = \frac{205}{W^2}\ \text{nb} \quad , \quad \text{(A.4)}$$

where θ^* is production angle in the two-photon system. The region of $|\cos\theta^*| < 0.6$ is almost covered by the detector acceptance of $|\cos\theta| < 0.7$.

W	$\gamma\gamma \to \mu\mu$	$\gamma\gamma \to \pi\pi + KK$
3.0 – 3.5	19.5	0.59 ± 0.15
3.5 – 4.0	14.6	0.052 ± 0.048
4.0 – 5.0	10.3	0.041 (upper limit)
5.0 – 10.0	4.1	0.0

unit : nb

Table A.1: Cross-section $\sigma_{\gamma\gamma\to X}(W)$ in the region $|\cos\theta^*| < 0.6$ for muon pair and pion/kaon pair production as a function of W.

We calculate $\sigma_{e^+e^-\to e^+e^-\mu^+\mu^-}$ and $\sigma_{e^+e^-\to e^+e^-\pi^+\mu^-/K^+K^-}$ by using Eq. A.1 and Table A.1. As a result, we obtain these cross-sections in the region of $|\cos\theta^*| < 0.6$ and $W \geq 3$ GeV/c^2 to be 207.8 and 1.75 pb, respectively. Contamination of these backgrounds is estimated less than 1%. In our interest region of $p > 2$ GeV/c ($W \geq 4$ GeV/c^2), these background fraction is negligibly small.

The other backgrounds coming from $e^+e^- \to e^+e^-e^+e^-$ process is suppressed by the requirement of $E_{\rm LG} < 1.0$ GeV. Since the probability of that an electron with p=1.5 GeV/c has a cluster energy less than 1.0 GeV/c^2 is about 1.4%, contamination of this background is less than 0.02%.

A.3 Pion samples

Controlled samples of pion can be obtained by identifying their parent particle. Here these parent particles are τ lepton and K_S meson. In this section, we describe how to select τ pair events and K_S decays in hadronic events.

A.3.1 Tau decays in tau pair production events

Tau lepton has hadronic decay modes as well as its characteristic one-prong leptonic decay mode. Here we use the following reaction which give a 1 .vs. 3 topology in the detector as shown in Fig. A.6.

$$e^+e^- \to \tau^+\tau^- \to \begin{cases} \tau^+ \to \pi^\pm\pi^\mp\pi^\pm X & (X \text{ is any neutral particles}) \\ \tau^- \to l^-\overline{\nu}_l\nu_\tau & (l = e, \mu) \end{cases} \tag{A.5}$$

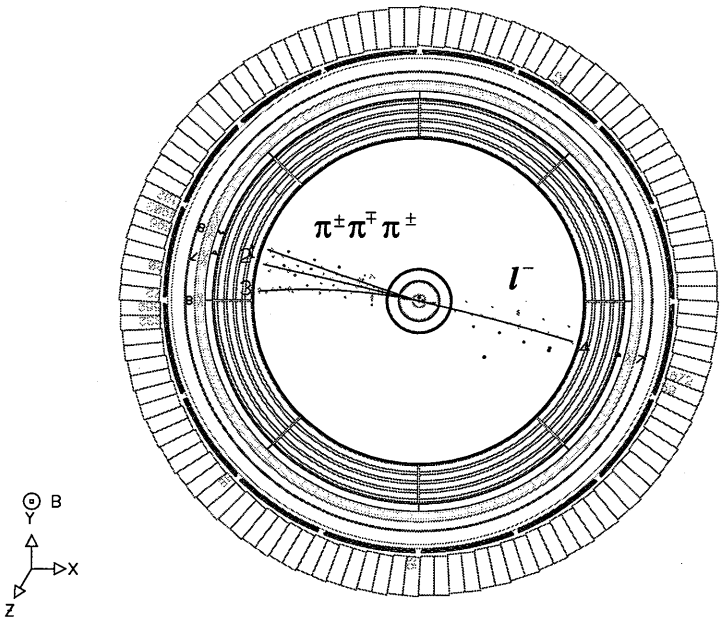

Figure A.6: Tau event samples

We require the following conditions to select tau pair events.

1. $N_{\text{good}} = 4$
   There are four tracks well[3] reconstructed in CDC.

2. $\Sigma E_{\text{LG}} \leq 0.75\ \sqrt{s}$
   To reduce hadronic events, we require a missing energy which is carried by neutrinos decaying from tau leptons.

[3] $N_{\text{axial wire hits}} \geq 10$, $N_{\text{slant wire hits}} \geq 4$, $|R_{\text{min}}| < 2$ cm, $|Z_{\text{min}}| < 15$ cm, $|\cos\theta| < 0.75$, $p \geq 2.0$ GeV/c

3. $E_{\rm vis} > 0.15\ E_{\rm beam}$
   To reduce two-photon events we reject events with considerably small visible energy.

4. $\Sigma|\overrightarrow{p}| \geq 0.25 E_{\rm beam}$
   This selection is effective to reduce the two-photon events.

5. $M_{\rm jet}$ <3.0 GeV/c^2
   We require that invariant mass of jets are consistent with tau mass (m_τ=1.7 GeV/c^2) as shown in Fig. A.7. This selection is effective to reduce hadronic events.

6. At least one charged particle of each hemisphere must have a momentum greater than 0.5 $E_{\rm beam}$.

7. $\cos\varphi \leq -0.8$
   We require that one particle is isolated from the other particles. The angle φ is defined as the angle between the isolated track and the most closest track.

After the above selection, we have obtained 511 tau pair events. Figure A.7 shows a distribution of the jet mass where histogram indicates a Monte Carlo prediction. Data and Monte Carlo prediction are consistent with each other within the errors.

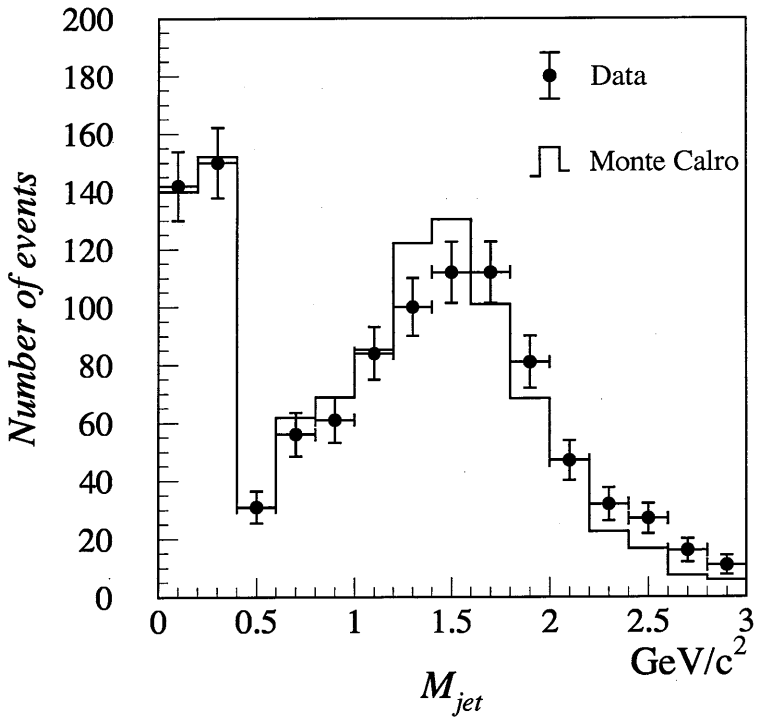

Figure A.7: Jet mass distribution of tau samples

Particles in the three prong side of these events are used as pion sample. This pion sample has a purity of 87.1% and muon impurity of 0.1% as listed in Table A.2. These are estimated by using a Monte Carlo simulation of the tau pair production.

$\tau \to \pi^{\pm}$	87.1%
$K^{\pm}$	2.5%
$e^{\pm}$	10.2%
$\mu^{\pm}$	0.1%

Table A.2: Components of τ decay sample.

A.3.2 Kaon (K_S) decays in hadronic events

K_S is a neutral kaon which decays predominantly into two pions with lifetime of 0.89×10^{-10} sec. Thereby, characteristic signals of K_S, its relatively long decay length (several cm) and two oppositely charged particles whose invariant mass coincides with the mass of K. K_S samples are selected by the following requirements in hadronic events.

1. Both of oppositely charged tracks are reconstructed successfully in 3 dimension.
2. Decay length[4] is greater than 7.0 cm.
3. An angle between momentum sum vector and a vector from interaction point to the decay point is less than 0.003 rad.
4. Difference of z position at the decay point is less than 3 cm.
5. To reject conversion electrons, invariant mass of them assuming electron masses is greater than 0.25 GeV/c^2.
6. Invariant mass of them assuming pion masses is less than 0.55 GeV/c^2.

Figure A.8 shows a typical K_S decay ($K_S \to \pi^+\pi^-$) in hadronic event.

[4]The decay point is defined as crossing point in the x-y plane. If two crossing points exist, we choose the closer one to the interaction point.

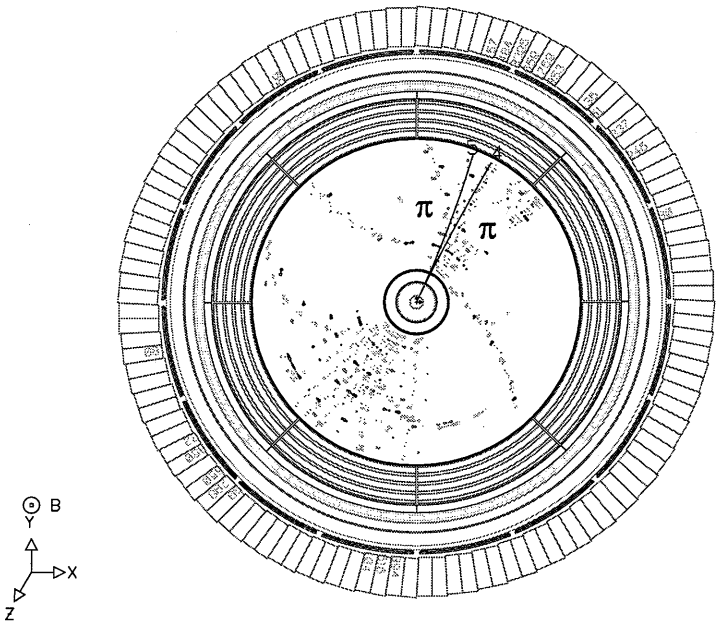

Figure A.8: K_S samples in hadronic events

After the above selection, we have obtained the 1958 K_S candidates. Figure A.9 shows a distribution of invariant mass. A clear peak is seen at the mass of charged kaon (~ 0.5 GeV/c^2). Shaded histogram indicate those of same sign charged track pairs, which is normalized in the controlled region of $M_{\pi\pi} > 0.6$ GeV/c^2. It corresponds to combinatorial background for K_S candidates. The number of combinatorial backgrounds is estimated to be 424 among 1985 K_S candidates.

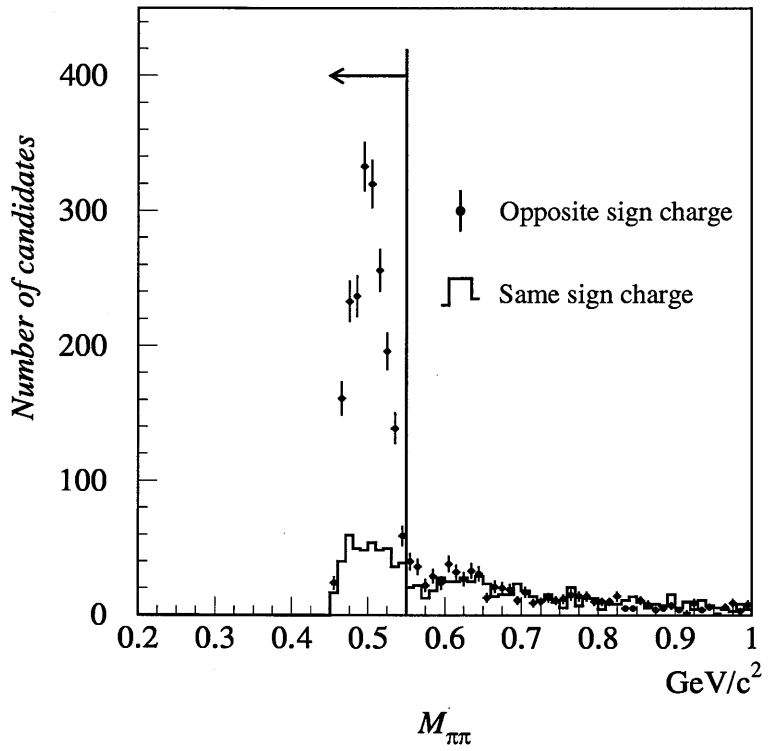

Figure A.9: K_S mass in hadronic events

This pion sample has a purity of 86.0% and muon impurity of 0.5% as listed in Table A.3, which is estimated by using a Monte Carlo simulation of the quark pair production.

$\pi^{\pm}$	86.0%
$K^{\pm}$	8.8%
$e^{\pm}$	1.3%
$P(\bar{P})$	3.7%
$\mu^{\pm}$	0.5%

Table A.3: Components of the K_S samples

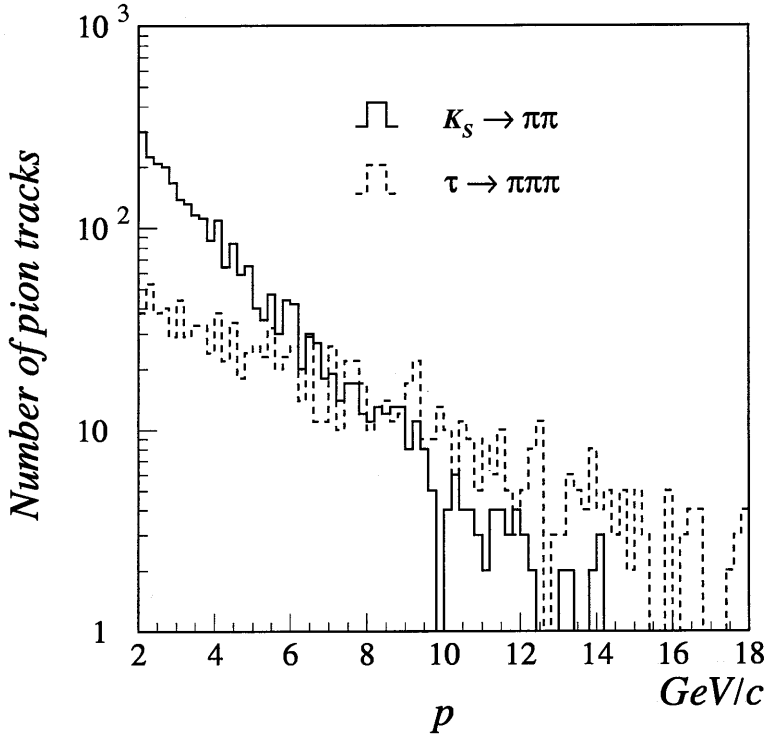

Figure A.10: Momentum distribution of τ and K_S samples.

Appendix B

Hadron misidentification as muon

Here we evaluate systematic errors of hadron misidentification probability as muon. Main uncertainty is due to the uncertainty of nuclear interaction in the material. Since pion and kaon lifetimes and their decay branches are well established, we assume that the uncertainty originated from decay in flight is less than 10%. Only when hadrons enter the calorimeters or return yoke, the number of decaying hadrons depend on the cross-section of nuclear interactions.

First of all, we check the capability to simulate nuclear interactions.

Simulation of the nuclear interaction.

If a nuclear interaction occurs with the detector, a particle is either scattered or produced more particles in its path. We study this effect by observing a distribution of crossing points of two CDC tracks. To enhance the tracks which scatter in the materials, we require that a three dimensionally reconstructed CDC track is far from interaction point ($|R_{\rm min}| > 1.0$ cm). Then we take all combinations among the above tracks and additional requirements are applied to the track pairs.

1. These track pairs have crossing points in the x-y plane and their z difference at the crossing point is less than 5 cm.

2. If both tracks satisfy the requirements $R_{\rm min} <0$, the pairs are rejected as photon conversion pairs. Because conversion electrons have negative value of $R_{\rm min}$ typically.

3. An absolute value of the momentum sum is restricted to be greater than 2 GeV/c, since this is the region of our interest.

After the above selections, a distribution of the crossing points is shown in Fig. B.1. Similar to photon conversion, clear peaks are seen at $R \sim 15$ and 25 cm. Plot and histogram are those of experimental data and Monte Carlo prediction, respectively. They are consistent with each other within the statistical error of 15%.

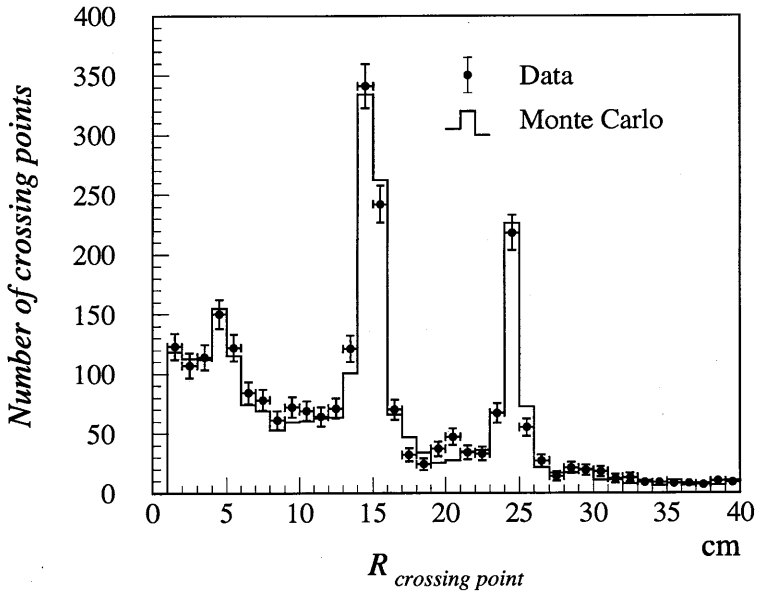

Figure B.1: Distribution of the crossing points in hadronic events

To evaluate the uncertainty of the simulation, we check the amount of the crossing points for the various nuclear cross-sections as shown in Table B.1. In the region of p >2 GeV/c, the dominant process among the nuclear interactions is inelastic interaction; when a pion has momenta of greater than 2 GeV/c, the cross-sections of elastic and inelastic interaction in carbon are 252 and 21 μb, respectively.

Since the statistical error of the number of crossing points is 15%, we can say that the uncertainty of inelastic cross-section is less than 20% as listed in Table B.1.

Nuclear interaction	Variation of its cross-section	Variation of the number of crossing points
inelastic	+20 %	+ 25 %
	−20 %	− 23 %
	+10 %	+ 8 %
	−10 %	− 12 %
elastic	+20 %	+ 2 %
	−20 %	− 2 %

Table B.1: Variation of the amount of the crossing points.

Uncertainty of the misidentification probability due to nuclear interactions.

Having proved the validity of our Monte Carlo in simulating nuclear interactions, we now study uncertainty of the misidentification probability by varying the cross-section of nuclear interactions. Tables B.2, B.3 and B.4 show the variation of the number of $\pi^{\pm}$, K^{+} and K^{-}, respectively, which are misidentified as muons.

Variation of cross-section		decaying hadrons	non decaying hadrons	Total
inelastic	+20%	− 5 %	− 60 %	−13 %
inelastic	−20%	+ 1 %	+141 %	+19 %
elastic	+20%	− 8 %	− 10 %	− 8 %
elastic	−20%	− 5 %	+ 30 %	− 1 %

Table B.2: Variation of $\pi^{\pm}$ backgrounds.

Variation of cross-section		decaying hadrons	non decaying hadrons	Total
inelastic	+20%	− 3 %	−35 %	−24 %
inelastic	−20%	− 3 %	+53 %	+35 %
elastic	+20%	− 9 %	− 3 %	− 5 %
elastic	−20%	+ 5 %	+ 6 %	+ 1 %

Table B.3: Variation of K^{+} backgrounds.

Variation of cross-section		decaying hadrons	non decaying hadrons	Total
inelastic	+20%	− 3 %	−43 %	−23 %
inelastic	−20%	− 5 %	+64 %	+39 %
elastic	+20%	+ 2 %	−10 %	− 4 %
elastic	−20%	+ 9 %	0 %	+ 4 %

Table B.4: Variation of K^{-} backgrounds.

From the above results, we can say that the systematic error of the hadron misidentification probability is due to the uncertainty of the number of particles which interact inelastically at the material and is estimated to be about 20%.

As another confirmation, we compare the matching quality distribution between experimental data and Monte Carlo data in hadronic events as shown in Fig. B.2.

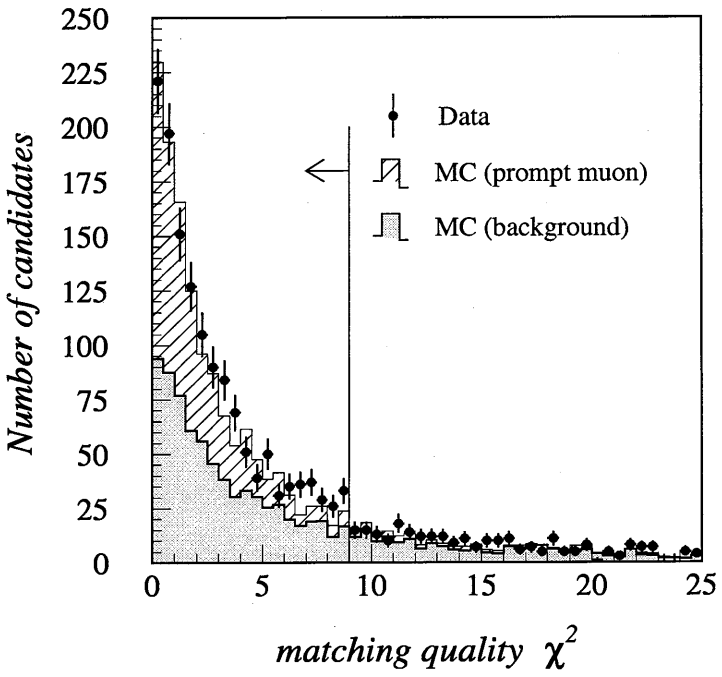

Figure B.2: Distribution of the matching quality χ^2_{matching} in hadronic events.

In the region of $\chi^2_{\text{matching}} > 9.0$, dominant source is misidentified hadrons as listed in Table B.5.

	The number of muon candidates in the region of $\chi^2_{\text{matching}} > 9.0$			
Data	366	(1.00)		
MC	346.7	(0.95)	··· 300.2	(Background)
			··· 46.5	(Prompt muon)

() ··· ratio of data to Monte Carlo

Table B.5: The number of muon candidates in the region of $\chi^2_{\text{matching}} > 9.0$.

Since Monte Carlo simulation of the background agrees well ($\sim 5\%$) in the region of $\chi^2_{\text{matching}} < 9.0$, we have a reasonable confidence in our Monte Carlo simulation describing the backgrounds in the region of $\chi^2_{\text{matching}} \leq 9.0$.

Appendix C

Detector simulator (VMONT)

In order to simulate decays and interactions of the particles and simulate the response of the VENUS detector, we have a detector simulator called VMONT[1].

Several reactions simulated by VMONT are as follows,

- Decays of hadrons ($\pi^{\pm}$, $K^{\pm}$, K_L^0 and so on.) and leptons ($\tau^{\pm}$ and $\mu^{\pm}$) are simulated. The position of the decay vertices and the time of flight is also calculated even for particles with short lifetime, such as K_S^0, Λ and D mesons, as well as those with long lifetime.
- Multiple Coulomb scattering, energy loss and nuclear interaction are simulated.
- For calorimeters, electro-magnetic cascade showers in the detectors are simulated by using actual geometry and materials coded in VMONT. Electromagnetic showers in the calorimeters, which originate from electrons and/or photons are simulated by EGS4 [48]. By basing on the obtained information from EGS4, the responses of calorimeters are calculated. The response of calorimeters for hadrons and muons is also calculated on the basis of the beam test data [65].
- For chambers, the responses of chambers are sumulated by taking into account the relation between the drift time and the drift length. The resolutions of each chambers are also taken into account. The simulation of detector responses uses tuned responces of each chamber.

C.1 Nuclear interactions

In our simulation, nuclear interactions are classified into two categories; one is elastic and the other is inelastic. The cross-section of both nuclear interactions depend on each material, species of incident particle and their momentum.

The momentum dependences are based on the experimental data of the cross-section for carbon target [67–69] as shown in Fig. C.1–C.6.

[1]Venus MONTe Calro simulator

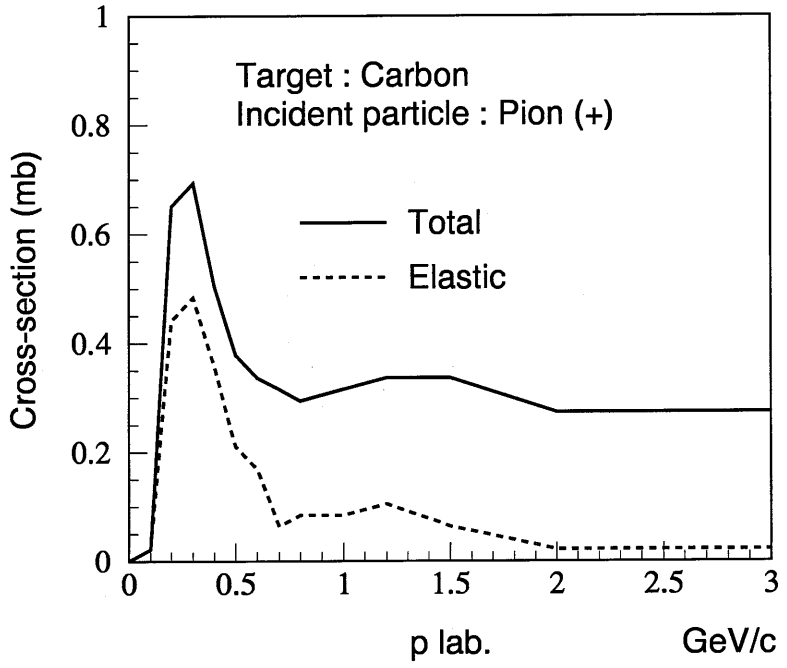

Figure C.1: Cross-section of nuclear interactions for π^+.

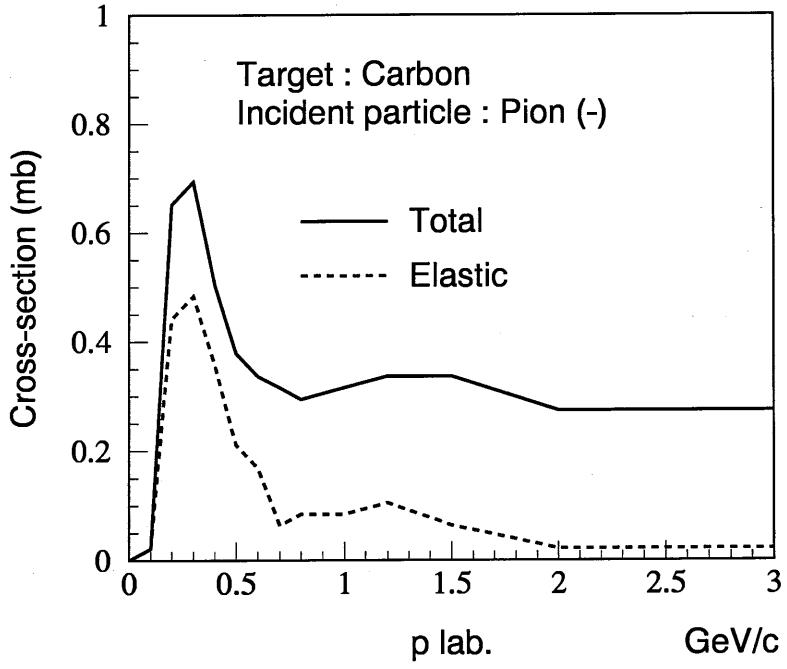

Figure C.2: Cross-section of nuclear interactions for π^-.

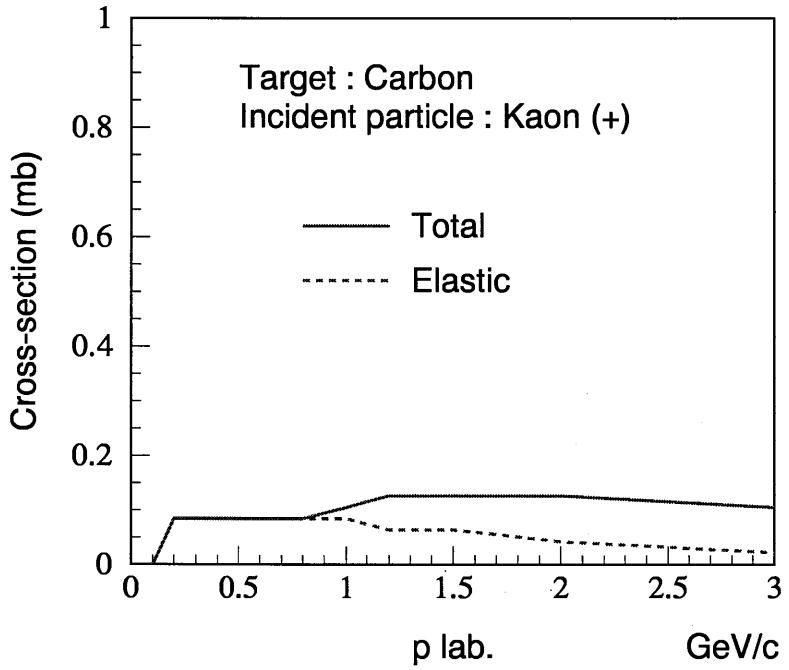

Figure C.3: Cross-section of nuclear interactions for K^+.

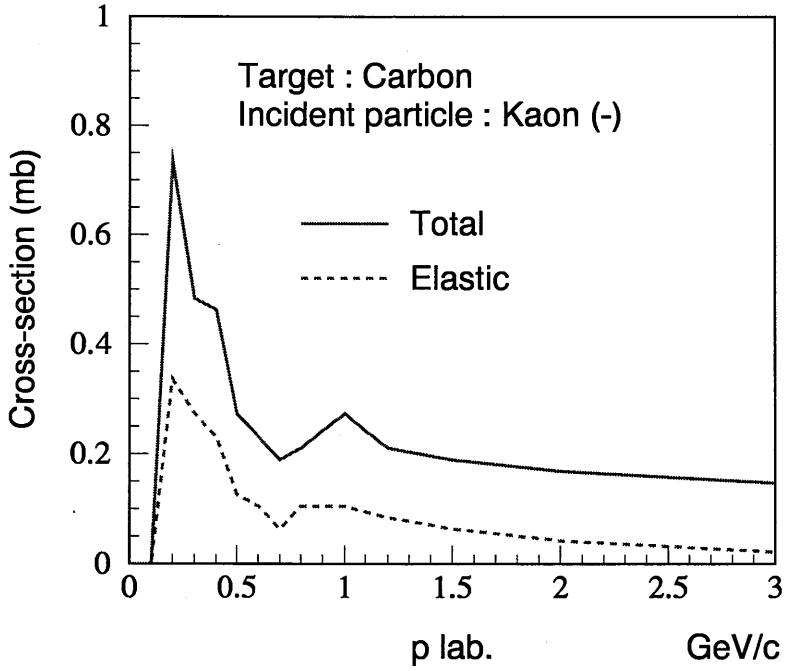

Figure C.4: Cross-section of nuclear interactions for K^-.

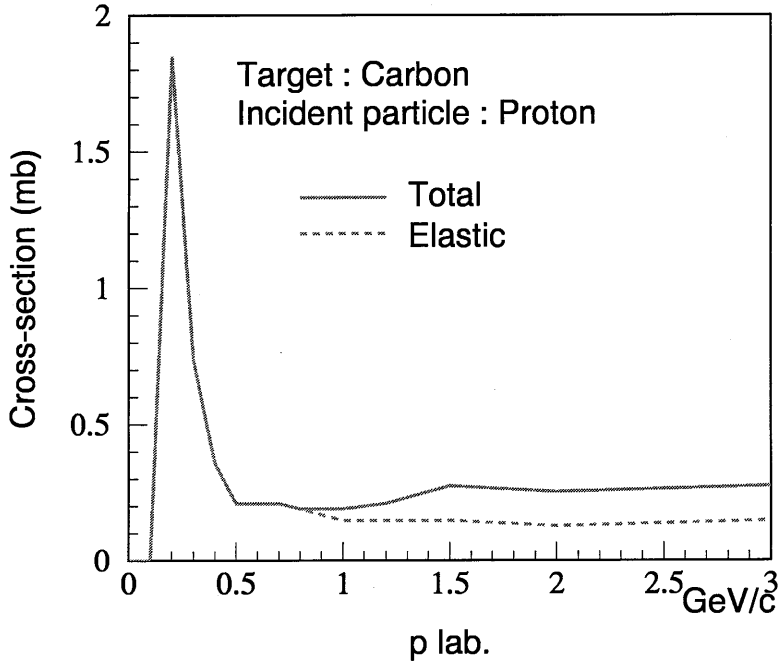

Figure C.5: Cross-section of nuclear interactions for proton.

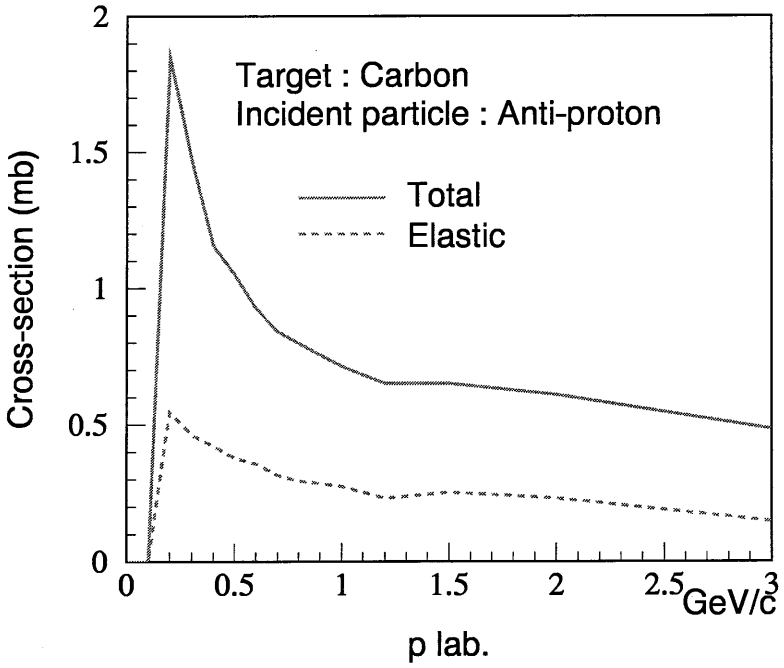

Figure C.6: Cross-section of nuclear interactions for anti-proton.

With the above cross-sections, elastic and inelastic interactions are simulated as follows,

1. Elastic interaction

   When an incident particle interacts with a nucleon in the material, we assume that either proton or neutron is chosen by the ratio of 1:1. The scattering angle θ_{elastic} is formulated with the incident particle momentum p as

$$\theta_{\text{elastic}} = \begin{cases} 13^\circ/p^2 & (p < 1 \text{ GeV}/c) \\ 13^\circ/p & (p \geq 1 \text{ GeV}/c) \end{cases}. \tag{C.1}$$

2. Inelastic interaction

   Inelastic interaction is simulated by the following reactions as listed in Table C.1. The final state is assumed to be uniform in the phase space.

Incident particle	multiplicity in final state	Reaction	branching ratio
$\pi(K)$	2-body	$\pi^+ + N \rightarrow \pi^0 + P$	$1/1 = (100\%)$
	3-body	$\pi^+ + P \rightarrow \pi^+ + \pi^+ + N$	$1/4 = 9/36$
		$\rightarrow \pi^+ + \pi^0 + P$	$1/4 = 9/36$
		$\pi^+ + N \rightarrow \pi^+ + \pi^- + P$	$1/6 = 6/36$
		$\rightarrow \pi^+ + \pi^0 + N$	$2/9 = 8/36$
		$\rightarrow \pi^0 + \pi^0 + P$	$1/9 = 4/36$
P	3-body	$P + P \rightarrow P + \pi^+ + N$	$5/12 = 40/96$
		$\rightarrow P + \pi^0 + P$	$1/12 = 8/96$
		$P + N \rightarrow P + \pi^- + P$	$1/8 = 12/96$
		$\rightarrow P + \pi^0 + N$	$9/32 = 27/96$
		$\rightarrow N + \pi^+ + N$	$3/32 = 9/96$
$N(\Lambda)$	3-body	$N + P \rightarrow N + \pi^+ + N$	$1/8 = 12/96$
		$\rightarrow$ N + π^0 + P	$9/32 = 27/96$
		$\rightarrow$ P + π^- + P	$3/32 = 9/96$
		$N + N \rightarrow N + \pi^- + P$	$5/12 = 40/96$
		$\rightarrow$ N + π^0 + N	$1/12 = 8/96$
$\overline{P}$	4-body	$\overline{P} + P \rightarrow \pi^+ + \pi^- + \pi^+ + \pi^-$	$1/4 = 1/4$
		$\rightarrow \pi^+ + \pi^- + \pi^0 + \pi^0$	$1/4 = 1/4$
		$\overline{P} + N \rightarrow \pi^+ + \pi^- + \pi^- + \pi^0$	$1/2 = 2/4$
$\overline{N}$	4-body	$\overline{N} + N \rightarrow \pi^+ + \pi^- + \pi^+ + \pi^-$	$1/4 = 1/4$
		$\rightarrow \pi^+ + \pi^- + \pi^+ + \pi^0$	$1/4 = 1/4$
		$\overline{N} + P \rightarrow \pi^+ + \pi^- + \pi^+ + \pi^0$	$1/2 = 2/4$

Table C.1: Reactions of inelastic nuclear interaction.

For $\pi^{\pm}$ and $K^{\pm}$, the ratio of two-body to three-body final state depends specially on the incident particle momentum as shown in Fig. C.7.

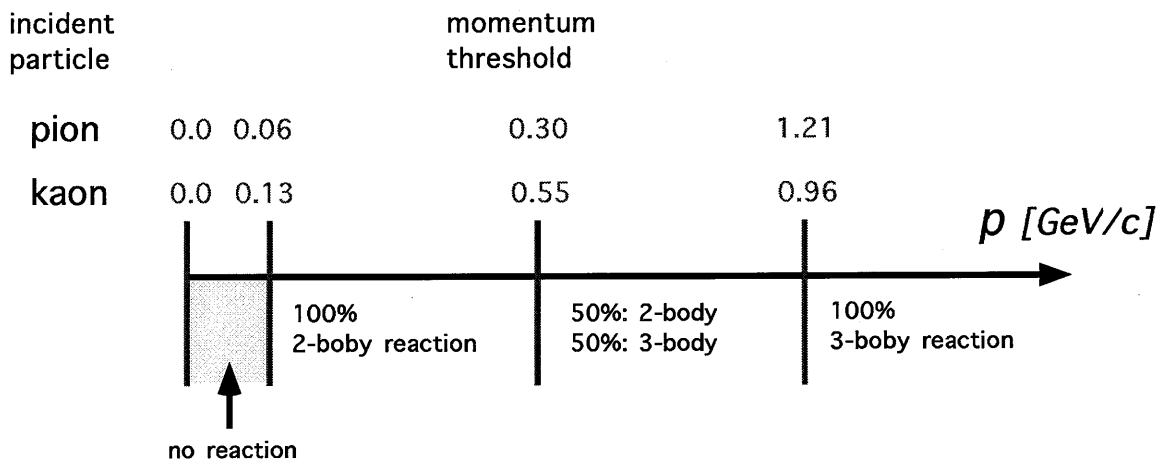

Figure C.7: Momentum threshold of inelastic reactions for pion and kaon.

Appendix D

The fragmentation parameter and the semileptonic decay branching ratio

Here we show that the fixed values of parameters as adopted in Chap. 6 are consistent with our own analysis. As described in Chap. 6.1, p and p_t spectrum of the observed lepton candidates is formulated as follows,

$$\begin{aligned} N_{\rm data}(p,p_t) &= \{\ \sigma_c B_c P_{cp}(\epsilon_c,p,p_t) \\ &+ \sigma_b B_b P_{bp}(\epsilon_b,p,p_t) \\ &+ \sigma_b B_{bc} P_{bs}(\epsilon_b,p,p_t)\cdot(1+\alpha) \\ &+ \sigma_b B_{bu} P_{bu}(\langle x_b\rangle,p,p_t) \\ &+ \sigma_b B_\tau P_{b\tau}(\epsilon_b,p,p_t)\ \}\cdot 2L\cdot\varepsilon(p,p_t) \\ &+ N_{bg} \end{aligned} \tag{D.1}$$

In Chap. 6, we fixed branching rations and fragmentation parameters to obtain σ_c and σ_b. Here we fix the value of σ_c and σ_b and fit the p and p_t spectrum by Eq. D.1 using ϵ_c and ϵ_b as free parameters. The fragmentation parameters ϵ_q correspond to the mean values of the scaled hadron energy $\langle x_q\rangle$. The other parameters are fixed as the following values as shown in Table D.1.

parameter	value
σ_c	39.7 pb
σ_b	14.3 pb
B_c	9.8 $\pm$ 0.5 %
B_b	11.13 $\pm$ 0.29 %
B_{bc}	7.9 $\pm$ 0.8 %
B_{bu}	0.3 $\pm$ 0.2 %
$B_{b\tau} = \mathrm{BR}\ (b \to \tau\nu_\tau X)$ $\cdot\ \mathrm{BR}\ (\tau \to e\nu_e\nu_\tau)$	0.48 %
$\langle x_c \rangle$	0.51 $\pm$ 0.02
$\langle x_b \rangle$	0.70 $\pm$ 0.02

Table D.1: World average values of the parameters.

The semileptonic decay branching ratios and the fragmentation parameter are fixed world average values [58, 60].

Second, we perform the same fit using the semileptonic decay branching ratios of B_c and B_b as free parameters. In this case, the fragmentation parameters are fixed at the values in Table D.1. We obtained the following results from the fits,

	electron sample	muon sample	combined result
$\langle x_c \rangle$	$0.49 \pm 0.04 \pm 0.03$	$0.47 \pm 0.05 \pm 0.03$	$0.50 \pm 0.03 \pm 0.02$
$\langle x_b \rangle$	$0.68 \pm 0.04 \pm 0.01$	$0.77^{+0.06}_{-0.05} \pm 0.01$	$0.71 \pm 0.03 \pm 0.01$
B_c	$10.5 \pm 0.9 \pm 1.1\%$	$7.2 \pm 1.1 \pm 1.8\%$	$10.6 \pm 0.7 \pm 0.9\%$
B_b	$13.1 \pm 1.2 \pm 1.0\%$	$13.3 \pm 1.5 \pm 0.8\%$	$13.7 \pm 1.0 \pm 0.7\%$

Table D.2: Measured values of fragmentation parameter and semileptonic decay branching ratio.

The first error is statistical and the second is systematic. These results are consistent with the values in Table 6.1.

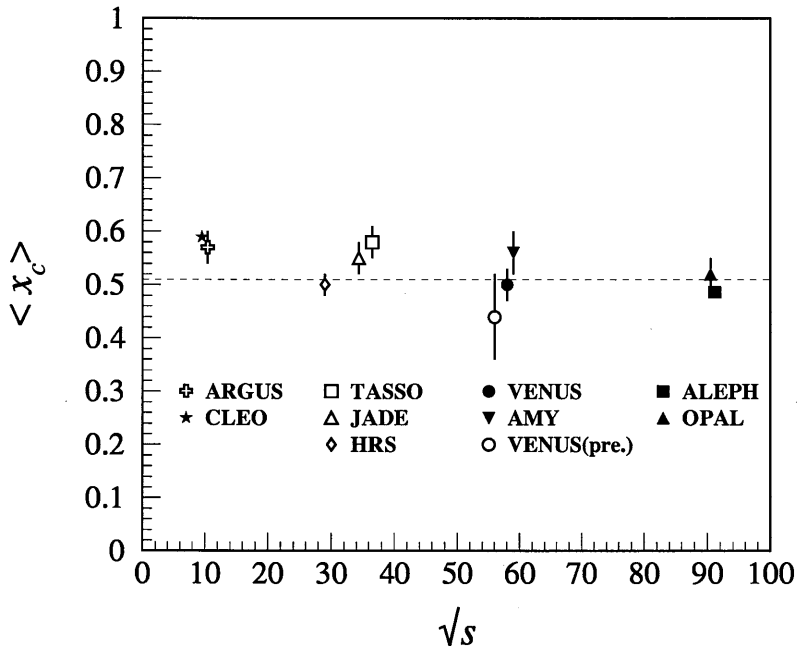

Figure D.1: Mean value of scaled c hadron energy. Dashed line indicate the world average value of 0.51.

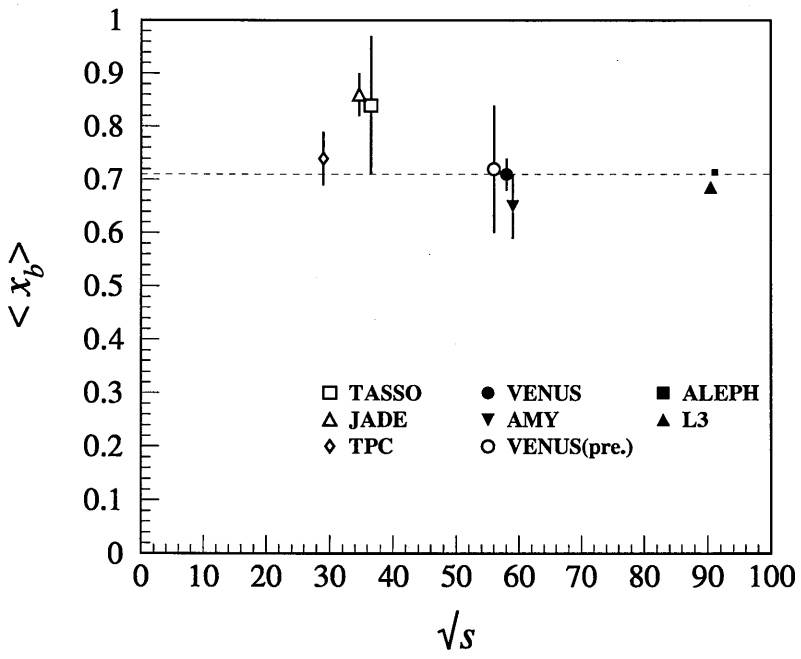

Figure D.2: Mean value of scaled b hadron energy. Dashed line indicate the world average value of 0.70.

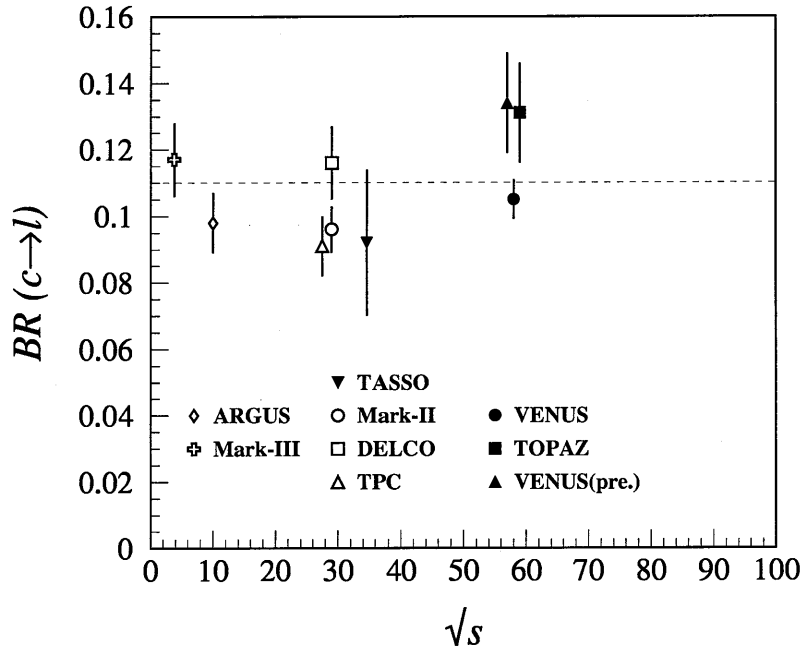

Figure D.3: Semileptonic decay branching ratio of c hadrons. Dashed line indicate the world average value of 9.8%.

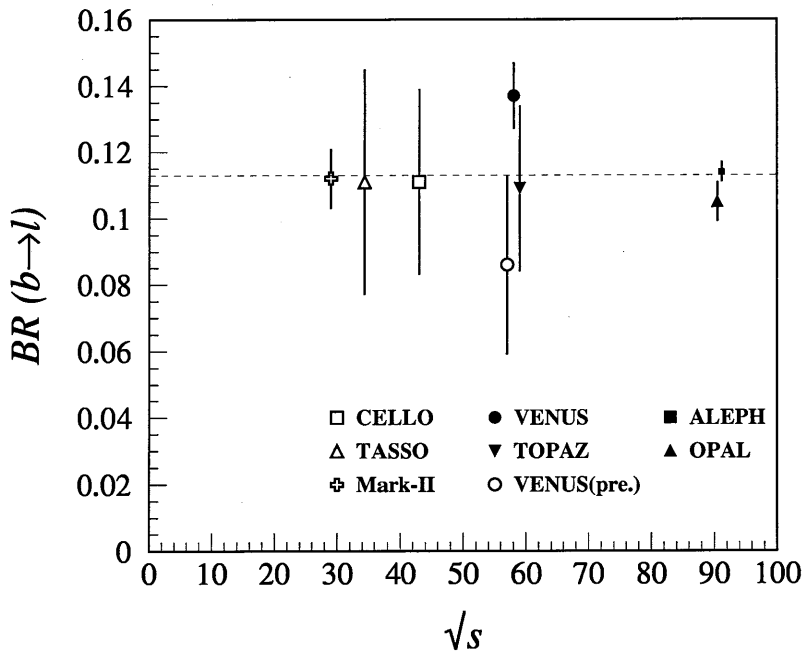

Figure D.4: Semileptonic decay branching ratio of b hadrons. Dashed line indicate the world average value of 11.1%.

Bibliography

[1] S. L. Glashow, Nucl. Phys. 22 (1961) 579;
S. Weinberg, Phys. Rev. Lett. 19 (1967) 1264;
A. Salam and J. C. Ward, Phys. Lett. 13 (1964) 168.

[2] Y. Nambu and G. Jana-Lasinio, Phys. Rev. 122 (1961) 345;
P. W. Higgs, Phys. Lett. 12 (1964) 132, Phys. Rev. 145 (1966) 1156.

[3] UA1 collab., Phys. Lett. 122 B (1983) 103; 122 B (1983) 476; 126 B (1983) 398; 129 B (1983) 130.

[4] VENUS collab., M. Shirakata *et al.*, Phys. Lett. B 278 (1992) 499

[5] VENUS collab., K. Abe *et al.*, Phys. Lett. B 313 (1993) 288

[6] C. Peterson *et al.*, Phys. Rev. D 27 (1983) 105.

[7] JADE collab., W. Bartel *et al.*, Z. Phys. C 33 (1986) 23;
S. Bethke *et al.*, Phys. Lett. B 213 (1988) 235.

[8] E.J. Eichten, K.D. Lane and M.E. Perkin, Phys. ReV. Lett. 50 (1983) 811.

[9] E.J. Eichten *et al.*, ReV. Mod. Phys. 56 (1984) 579.

[10] HRS Collab., M. Derrick et al., Phys. Rev. D 34 (1986) 3286.

[11] MAC Collab., E. Fernandez et al., Phys. Rev. D 35 (1987) 10.

[12] CELLO Collab., H.J. Behrend et al., Z. Phys. C 51 (1991) 149.

[13] JADE Collab., W. Bartel et al., Z. Phys. C 30 (1986) 371.

[14] PLUTO Collab., Ch. Barger et al., Z.Phys. C 27 (1985) 341.

[15] TASSO Collab., W. Braunschweig et al., Z.Phys. C 37 (1988) 171.

[16] VENUS Collab., K. Abe et al., Z.Phys. C 48 (1990) 13.

[17] ALEPH Collab., Buskulic et al., Z.Phys. C 59 (1993) 215:

[18] VENUS Collab., K. Abe et al., Phys.Lett. B 232 (1989) 425.

[19] TOPAZ Collab., I. Adachi et al., Phys.Lett. B 255 (1991) 613.

[20] UA2 Collab., J. Alitti et al., Phys. Lett. B 257 (1991) 232.

[21] UA2 Collab., J.A. Appel et al., Phys. Lett. B 160 (1985) 349.

[22] UA2 Collab., P. Bagnaia et al., Phys. Lett. B 138 (1984) 430.

[23] UA1 Collab., G. Arnison et al., Phys. Lett. B 172 (1986) 461.

[24] UA1 Collab., G. Arnison et al., Phys. Lett. B 177 (1986) 244.

[25] M.J. Shochet, plenary talk at the XXIV Intern. Conf. on High energy physics (Munich, August 1988).

[26] VENUS collab., T. Arima *et al.*, Phys. Rev. D55: 19-39, 1997.

[27] Y. Yamada *et al.*, Nucl. Instr. and Meth. A330 (1994) 64-75.

[28] F.Takasaki *et al.*, Nucl. Instr. and Meth. A322 (1992) 211.

[29] R. Arai *et al.*, Nucl.Instr. and Meth. 217 (1983) 181.

[30] M. Sakuda *et al.*, Nucl. Instr. and Meth. A311 (1992) 57-77.

[31] Y. Hemmi *et al.*, Jpn. J. Appl. Phys. 26 (1987) 982.

[32] R. Arai *et al.*, Nucl. Instr. and Meth. A254 (1987) 317-326.

[33] K. Ogawa *et al.*, Jpn. J.Appl. Phys. 23 (1984) 897-903.

[34] K.Ogawa *et al.*, Nucl. Instr. and Meth. A238 (1985) 328-332.

[35] K. Ogawa *et al.*, Nucl. Instr. and Meth. A243 (1986) 58-66.

[36] T. Sumiyoshi *et al.*, Nucl. Instr. and Meth. A271 (1988) 432-441.

[37] Y. Fukushima *et al.*, IEEE, TRANS. NS. 36 (1989) 670.

[38] Y. Asano *et al.*, Nucl. Instr. and Meth. A259 (1987) 430-437.

[39] Y. Ikegami *et al.*, IEEE, TRANS. NS. 36 (1989) 183.

[40] T. Ohsugi *et al.*, Nucl. Instr. and Meth. A269 (1988) 522-526.

[41] K. Amako *et al.*, Nucl. Instr. and Meth. A272 (1988) 687-694.

[42] Y. Arai and Y. Yasu, IEEE, Trans. NS. 35 (1988) 300.

[43] Y. Arai and S. Uehara, Nucl. Instr. and Meth. A301 (1991) 497-505.

[44] KEK Data Acquisition Development Working Group, KEK-REPORT 85-10

[45] Y. Nakagawa *et al.*, Jpn. J. Appl. Phys. 25 (1986) 1049.

[46] Y. Noguchi and A. Ono, Nucl. Instr. and Meth. A253 (1986) 27-37.

[47] T. Oyama *et al.*, Nucl. Instr. and Meth. A305 (1991) 71-81.

[48] R. L. Fold and W. R. Nelson, SLAC-report-210, UC-32(1978);
W. R. Nelson, H. Hirayama and D. W. O. Rogers, SLAC-report-265, December 1985.

[49] G. A. Akopdjanov *et al.*, Nucl. Instr. and Meth. 140 (1977) 441.

[50] N. Kanda, VENUS-NOTE No.260.

[51] VENUS Collab., K. Abe *et al.*, Phys. Lett. 234B (1990) 382.

[52] T. Sjöstrand *et al.*, Comput. Phys. Commun. 43 (1987) 367;
T. Sjöstrand. CERN-TH-6488-92, May 1992. 284pp.

[53] J. J. Sakurai and D. Schildknecht, Phys. Lett. B40 (1979) 121;
I. F. Ginzburg and V. G. Selbo, Phys. Lett. B109 (1982) 231.

[54] M. Drees, M. Kämer, J. Zunft and P. M. Zerwas, Phys. Lett. B306 (1993) 371;
J. Smith and W. van. Neerven, Nucl. Phys. 274 (1992) 36.

[55] H. Abramowicz, K. Charchula and A. Levy, Phys. Lett. B269 (1991) 458.

[56] S. Odaka, VENUS NOTE 289(1993).

[57] Don Groom, Particle Data Group Note: PDG-95-01.

[58] Particle Data Group, Phys. Rev. D54(1996)1, Review of Particle Physics.

[59] ALEPH collab., D. Buskulic *et al.*, Phys. Lett. B343 (1995) 444.

[60] The LEP experiments: ALEPH, DELPHI, L3 and OPAL, Nucl. Instr. Meth. A378 (1996) 101.

[61] CLEO collab., R. Fulton *et al.*, Phys. Rev. Lett. 64 (1990) 16;
ARGUS collab., H. Albrecht *et al.*, Phys. Lett. B234 (1990) 409.

[62] ALEPH collab., D. Buskulic *et al.*, Phys. Lett. B384 (1996) 414.

[63] D.Bardin *et al.*, CERN-TH. 6443/92: e-Print Archive: hep-ph/9412201

[64] K. Hagihara *et al.*, Phys. Lett. B219 (1989) 369.

[65] K. Ogawa *et al.*, KEK-PREPRINT-94-169;
K. Ogawa *et al.*, Nucl. Instrum. Methods A238 (1985) 328-332.

[66] CLEO Collab., J. Dominick *et al.*, Phys. Rev. D50: 3027-3037, 1994.

[67] A. S. Carroll *et al.*, BNL-21171: KEK Accession No. 75-5-131.

[68] C. J. Battey *et al.*, Nucl. Phys. (1973) 429-503.

[69] E. Schwarz *et al.*, Phys. Rev. Lett (1979) 1578.